Plasmonic Nanoantenna Arrays: Optical Properties and their Applications in Biosensing

A thesis presented

by

Stephanie Lynn Dodson

submitted to

The School of Physical and Mathematical Sciences

at

Nanyang Technological University

in fulfillment of the requirement for the degree of

Doctor of Philosophy

in the subject of

Physics and Applied Physics

2014

ACKNOWLEDGEMENTS

First and foremost, I would like to thank my advisors, Professor Qihua Xiong and Professor Shuzhou Li, for their guidance throughout my doctorate.

I would also like to thank Professor Jerome Plain for hosting me for lab exchange and the Merlion program for providing the opportunity to travel to France to collaborate with UTT. I would like to thank all of my friends and lab mates at UTT, particularly Jonathan Darcos for being the best undergraduate slave anyone could ask for, Mohamed Haggui for spending the last few stressful months of his doctorate teaching me photochemical imaging, and Julien Proust for teaching me so much about French culture, cooking and wine.

I am grateful to all my lab mates at NTU for all of the scientific and cultural experiences we have shared, particularly Xinlong Xu for the many hours in the SEM room sharing stories from Chinese mythology and language, and also Cuong Cao and Hamed Zaribafzadeh for sharing all the biosensing knowledge and experience.

I would like to thank my parents, William and Arlene Dodson, for their support through the past twenty-four years of schooling.

Also, a huge thank you is in order to my friends for their encouragement through good times and bad during my doctorate, particularly Brendan Orner, Ian Oliver, and Alexander Petrovic for their help and advice on my thesis.

ABSTRACT

Plasmonics is a field that has developed around the phenomenon that in a metal dielectric interface electrons act as a gas or cloud. Along a surface, in an external oscillating electromagnetic field, this electron cloud propagates as surface plasmon polaritons. However this thesis focuses on localized surface plasmons, which occur in metallic nanoparticles. In external oscillating electromagnetic field, the electron gas oscillates around the nanoparticle surface leading to areas of localized, intense electromagnetic field, called hotspots. This localized surface plasmon phenomenon has lead to the development of many different applications such as plasmon lasers, super resolution imaging, surface enhanced Raman scattering, and localized surface plasmon resonance spectroscopy. This thesis will focus on the biosensing techniques developed around localized surface plasmon resonances and surface enhanced Raman scattering.

During this thesis work, we developed nanorod arrays for localized surface plasmon resonance based biosensing. We studied the effects of nanorod geometry and array parameters on resonance using both simulation and experimental methods. We fabricated nanorods in a variety of rectangular arrays to achieve very sharp resonances. These arrays had sensitivities of up to 310 nm/RIU with a figure of merit of 3.6. We were able to observe the adsorption of single stranded DNA on the femptomolar scale. The nanorod arrays developed in this work were able to detect single nucleotide polymorphisms in the k-ras oncogene in concentrations as low as 1 nM mutant type out of 1000 nM wild type.

In the field of surface enhanced Raman scattering based biosensing, bowtie nanoantenna had already shown great potential as sensitive biosensors. Previous studies had shown a strong central hotspot in the junction between prisms that was particularly useful for observing enhanced Raman spectra of biomarkers. In this thesis work, we designed bowtie nanoantennae for the optimization of a surface enhanced Raman scattering (SERS) based biosensor. We fabricated bowtie nanoantennae in a variety of geometries, with gaps as small as 3 nm. We characterized the near field and far field computationally and experimentally to observe the effects of gap size, prism size, metal thickness, corner radius of curvature, and array density. The bowtie antennae designed in this work were able to achieve surface enhanced Raman scattering enhancement factors as high as 10^{11}.

In order to experimentally observe the near electric field localization of bowtie antennae we used a photosensitive polymer to perform photochemical near field imaging. Using the established technique of photochemical near field imaging, we were able to image the off resonance modes various bowtie antennae. In order to image the near field localization of the transverse and longitudinal modes, we developed a new technique that made use of the two-photon absorption of the photosensitive polymer in order to allow imaging of modes in a wider spectral range.

The research done in the course of this thesis has many impacts on the field of plasmonics. The nanorod array biosensor for localized surface plasmon resonance based biosensing is extremely sensitive and has been shown to be able to detect very low concentrations of mutant DNA in mixed analyte samples. This biosensor can be easily tuned to the desired resonance through variation of nanorod geometry and array parameters. The photochemical near field imaging technique developed in the course of this thesis has the potential to be used for characterizing many different plasmonic nanostructures. By developing a two-photon absorption based technique and increasing the spectral range of the usable excitation wavelengths a wide variety of nanostructure near field modes can be imaged.

TABLE OF CONTENTS

TABLE OF FIGURES

1 CHAPTER 1: INTRODUCTION

1.1 MOTIVATION

Highly sensitive biosensors allow for the accurate recognition of low concentrations of biomarkers, implying the possibility of earlier disease diagnosis and treatment.[1] With this in mind, it is of great interest to exploit the novel properties exhibited by noble metals in the nanoscale for making sensitive, plasmonics-based biosensing technologies. Biosensors based on surface enhanced Raman scattering (SERS) and localized surface plasmon resonance (LSPR) have great potential as both rapid and sensitive tools.[2-3]

Early detection of diseases is vital for effective treatment. For example, many times cancer is not diagnosed until its later stages when it has spread and metastasized. These later stages of cancer are more difficult to treat, making early diagnosis an integral part of successful treatment. The past 35 years have witnessed an increase in cancer incidence, while the past 18 years have seen a decrease in the mortality rate of cancer in the US.[4] The increasing prevalence of cancer indicates that it is still a critical problem, while the decrease in the mortality rate from cancer implies that, once diagnosed, treatments are becoming more effective. Detection can, therefore, be considered a top priority issue as cancer can only be treated once it has been diagnosed.

Conventional cancer diagnosis techniques do not have the specificity or sensitivity required for true early-stage cancer detection. Currently, common cancer detection methods consist of computer assisted tomography (CAT) scanning, visual and digital examination, x-ray imaging, ultrasound imaging, and proteomics. Many of these methods are macro-scale techniques that require the patient to be in the later stages of cancer for the symptoms to be observable. Proteomics, the study of proteins, has profoundly changed the landscape of detection of diseases enabling a variety of techniques which takes advantage of the properties of proteins that make them excellent biomarkers for diseases, such as cancer, and has great potential for early-stage diagnosis.

The proteomics techniques most commonly used today are mass spectrometry and antibody binding coupled with either gel electrophoresis or fluorescence microscopy.[1] Detection sensitivity is very important in biosensing, particularly proteomics, as higher

sensitivity allows for earlier detection of disease biomarkers. In early stages of cancer, the level of biomarkers is still very low, sometimes too low for current detection methods to distinguish. Higher sensitivity in biosensors means lower concentrations of biomarkers are required for accurate detection, implying the need for less sample from the patient. With this in mind, current research focuses on the development of biosensors for use in highly sensitive and specific biosensing applications. With a high sensitivity biosensor, it will be possible to detect low concentrations of biomarkers allowing for early diagnosis of diseases, such as cancer, which will lead to more effective, earlier treatments and higher survival rates.

Higher sensitivity and specificity can lead to earlier diagnosis, which in turn can lead to higher survival rates. The challenge lies in that the concentration of disease biomarkers at early diagnosis stages is usually very low.[1] This is normally the limiting factor in how early the disease can be detected using proteomic biosensors. Higher detection sensitivity in proteomic biosensors allows for the accurate detection of lower concentrations of biomarkers, implying the possibility of earlier diagnosis.[1] New, nanotechnology-based biosensors make use of the unique optical and electrical properties of nanoscale particles. The novel optical and electronic properties exhibited by noble metals in the nanoscale can be utilized to make various types of plasmonic biosensors. SERS and LSPR are techniques that have shown great promise as plasmonic biosensing platforms.[2-3]

1.2 PLASMONICS

Surface plasmons are waves that propagate along the surface of a conductor caused by collective electron oscillations.[5] The plasmonic response of the colloidal metallic nanoparticles is responsible for the color variation in the Lycurgus Cup and in much ancient stained glass.[6-7] Nanoparticles of different shapes, sizes, and materials will absorb and scatter light at different wavelengths. We can make use of the interesting optical and electrical properties of plasmonic nanoparticles to create molecular biosensors.

In an external, oscillating electromagnetic field the free electrons of noble metal atoms in the nanoparticles become displaced from the nuclei and act as an electron cloud.[8] The Coulomb attraction between the nuclei and their displaced electrons acts as a restoring force and the electron cloud is induced into collective, coherent oscillations,

which are quantized and labeled as surface plasmons.[9] Surface plasmon polaritons, shown in Figure 1a, propagate along metal-dielectric interface.[10-11] Localized surface plasmons, shown in Figure 1b, occur when light interacts with particles much smaller than the incident wavelength and the plasmon oscillates around the nanoparticle with a frequency known as the LSPR.[12-13] This phenomenon leads to areas of intense, localized enhancement of the electric field, called hotspots. Particle shape, size and material, as well as surrounding dielectric, will affect the optical and electronic properties of the particle.[14]

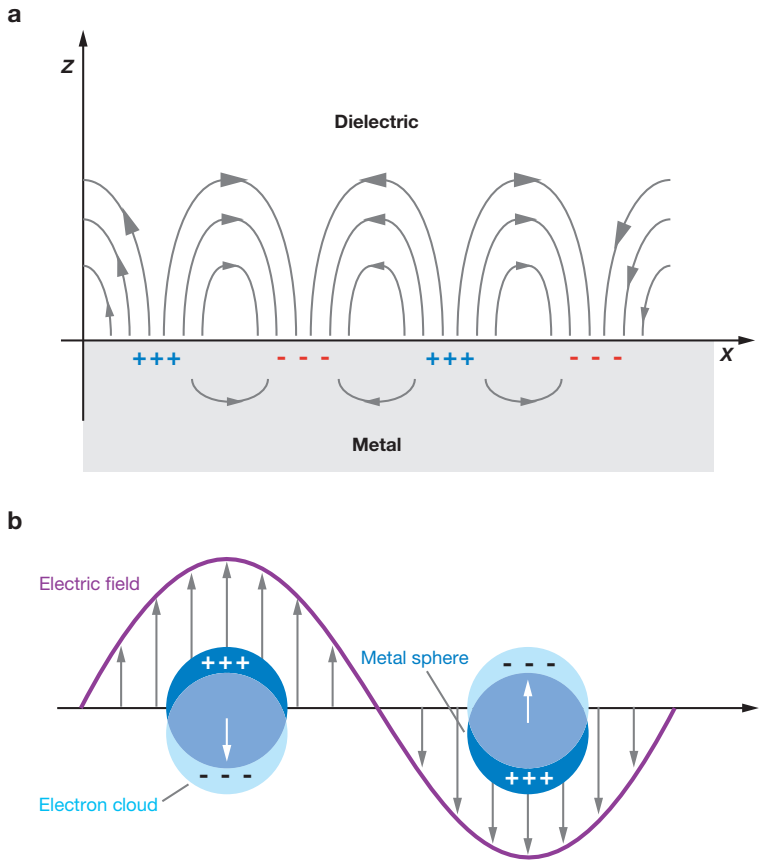

FIGURE 1: ILLUSTRATION OF A SURFACE PLASMON

Schematic diagrams illustrating (a) a surface plasmon polariton and (b) a localized surface plasmon, showing the response of noble metal spheres to an oscillating electric field, demonstrating the oscillation of the free electron cloud relative to the nuclei. Adapted from Willets et al.[15]

Maxwell's equations can be used to describe and understand the optical properties of materials. Maxwell's equations describing the behavior of a wave in a material are:

$$\nabla \cdot \vec{B} = 0 \qquad (1\text{-}1)$$

$$\nabla \cdot \vec{D} = \rho_f \qquad (1\text{-}2)$$

$$\nabla \times \vec{E} = -\frac{\partial}{\partial t}\vec{B} \qquad (1\text{-}3)$$

$$\nabla \times \vec{H} = \vec{J_f} + \frac{\partial}{\partial t}\vec{D} \qquad (1\text{-}4)$$

where $\vec{B}$ is the magnetic induction, $\vec{D}$ is the electric displacement, ρ_f is the charge density, $\vec{E}$ is the electric field, $\vec{H}$ is the magnetic field, $\vec{J_f}$ is the free electric current.

Permittivity, ϵ, is a description of the response of a material to an electric field. Permeability, μ, represents the response of a material to a magnetic field. Permittivity and permeability can be used to relate the electric and magnetic displacements and fields, as follows:

$$\vec{D} = \epsilon_0 \epsilon_r \vec{E} \qquad (1\text{-}5)$$

$$\vec{B} = \mu_0 \mu_r \vec{H} \qquad (1\text{-}6)$$

where ϵ_0 is the permittivity of free space, ϵ_r is the relative permittivity, μ_0 is the permeability of free space, and μ_r is the relative permeability.

To determine the electric field distribution around a spherical particle smaller than the wavelength of incident light a quasi-electrostatic approximation can be used to solve LaPlace's equation:

$$\nabla^2 \varphi = 0 \qquad (1\text{-}7)$$

$$E = -\nabla \varphi \qquad (1\text{-}8)$$

where φ is the electric potential, with the boundary conditions that φ is continuous at the sphere surface and the normal component of D is also continuous. If we only consider one dimension and restrict the angular momentum to $\ell = 1$, the potential becomes:

$$\varphi = A\, r \sin\theta \cos\phi \text{ , for } r < a \qquad (1\text{-}9)$$

$$\varphi = (-E_0 r + B/r^2) \sin\theta \cos\phi \text{ , for } r > a \qquad (1\text{-}10)$$

where A and B are constants. From these solutions we can determine the electric field outside the sphere:

$$E_{out} = E_0\hat{x} - \alpha E_0\left[\frac{\hat{x}}{r^3} - \frac{3x}{r^5}(x\hat{x} + y\hat{y} + z\hat{z})\right] \qquad (1\text{-}11)$$

where α is the polarizability of the sphere. The first term is the applied field and the second term is the induced dipole field for an induced dipole moment, $p = \alpha E_0$. Polarizability is given by:

$$\alpha = \frac{\epsilon_r - \epsilon_0}{\epsilon_r + 2\epsilon_0}a^3 \qquad (1\text{-}12)$$

This leads to an extinction efficiency[16] of:

$$Q_{ext} = \frac{C_{ext}}{\pi a^2} = \frac{8\pi a(\epsilon_0)^{1/2}}{\lambda}\,\mathrm{Im}\left(\frac{\epsilon_r - \epsilon_0}{\epsilon_r + 2\epsilon_0}\right) \qquad (1\text{-}13)$$

Extinction efficiency is the ratio of the extinction cross section over the geometrical cross section of the particle. The extinction cross section denotes the area of incident light that is likely to interact with a particle, through both scattering and absorption:

$$C_{ext} = C_{sca} + C_{abs} \qquad (1\text{-}14)$$

where C_{sca} is the scattering cross section and C_{abs} is the absorption cross section. The extinction efficiency is the inverse of transmission, T, which is the incident light that does not interact with the particle:

$$Q_{ext} = 1 - T \qquad (1\text{-}15)$$

Transmission is easy to measure experimentally, through optical transmission spectroscopy, while extinction efficiency is easy to simulate, and the two values can be easily compared through their inverse relationship. Simulated extinction spectra and experimental transmission spectra can be correlated with geometrical parameters for the identification of plasmonic and photonic modes.

By concentrating light into nanoscale volume, plasmonic elements allow for fundamental studies of light-matter interactions at length scales that were otherwise inaccessible.[17] Nanostructured metals dramatically alter the way light scatters from molecules, which led to the development of surface-enhanced Raman spectroscopy.[18-20]

Plasmonics has been used to create waveguides, metal films with nanoscale holes with unexpectedly high optical transmission, metal thin films that act as optical lenses, ultrafast logic circuits, and metamaterials which engineer optical space to control light.[21-25]

1.3 LOCALIZED SURFACE PLASMON RESONANCE

The localized surface plasmon resonance (LSPR) is the inherent frequency at which the electron cloud of a metallic nanoparticle oscillates in an external electromagnetic field. Resonance condition is achieved when the frequency of the driving force, F_d, from the oscillating external field matches the restoring force of the Coulomb attraction, F_C, of the electron cloud to the nuclei.

$$F_C = -2\pi n e^2 d \tag{1-16}$$

$$\boldsymbol{F}_d = \frac{m\boldsymbol{a}}{2} = \frac{m\ddot{\boldsymbol{d}}}{2} = \frac{-m\omega_p^2 \boldsymbol{d}}{2} \tag{1-17}$$

$$\therefore \omega_p = \sqrt{\frac{4\pi n e^2}{m}} \tag{1-18}$$

where n is the electron density, e is the charge of the electron, m is the mass of the electron, a is the acceleration, d is the displacement, and ω_p is the plasma frequency. The frequency of these resonances is highly dependent on the shape, size, composition, and dielectric environment of the particle.[14, 26-28] The LSPR can be observed through transmission spectroscopy, illustrated in Figure 2. Transmission spectroscopy measures the extinction spectrum of the sample by measuring the light that passes through the sample at different wavelengths.[15]

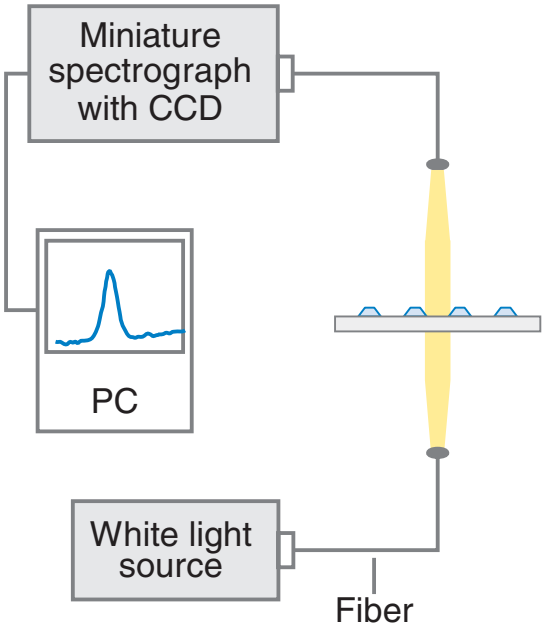

FIGURE 2: ILLUSTRATION OFTRANSMISSION SPECTROSCOPY EXPERIMENTAL SETUP

Typical transmission spectroscopy geometry for measuring extinction spectra of nanoparticle arrays. Adapted from Willets et al.[15, 29]

LSPR biosensing makes use of the response of plasmonic devices to their dielectric environment to detect binding events between biomolecules.[30] In these types of experiments, coatings of biomolecules act as a dielectric medium to which the LSPR reacts. Higher numbers of molecule binding and larger molecules both lead to increased local refractive index. The response of the biosensor dictates the limit of detection of disease biomarkers. The design specifications of the nanoparticles and the array parameters have a strong influence on the resonance position and shape. Designing and tuning nanoparticle arrays can achieve sharp resonances in the spectral region of interest for the chosen spectroscopic technique. It is easier to distinguish shifts in resonance when the resonance is sharp, leading to a high sensitivity to dielectric environment.

Sensitivity, figure of merit (FOM), and quality factor are quantitative ways of measuring the response of a sensor to its dielectric environment.[31] Sensitivity is defined as:

$$S = \frac{\Delta\lambda}{\Delta n} \qquad (1\text{-}19)$$

where $\Delta\lambda$ is the change in wavelength and Δn is the change in refractive index. The FOM is then given by:

$$\text{FOM} = \frac{S}{\text{FWHM}} \qquad (1\text{-}20)$$

where FWHM is the full width of the LSPR transmission plot curve at half of the peak value. Quality factor for LSPR sensors is defined as:

$$Q = \frac{\lambda_{max}}{FWHM} \qquad (1\text{-}21)$$

where is the wavelength of the resonance peak. LSPR sensors have been reported with sensitivities between 25 and 868 nm /RIU.[32-33] Typical quality factors are between 3 and 8 in the visible and near infrared region.[27] A high sensitivity and a narrow resonance profile make for high-quality sensors.

Nanoparticle LSPR can be very sensitive to local changes in the dielectric environment of the particle.[2, 34-37] Since biomolecules generally have a higher refractive index than their buffer solutions, the binding of biomolecules to the surface of nanoparticles changes the local dielectric environment and can be detected by the LSPR shifts. Binding events can be observed using simple transmission spectroscopy. Highly sensitive LSPR biosensing has already been done using various plasmonic substrates.[34, 38-41] LSPR-based sensing of DNA hybridization reached the attomolar scale, antibody-antigen binding has been detected at 2 pg/mL, and thrombin has been detected at concentrations of 1 ng/mL.[32-33, 42-44]

Metallic nanorod arrays have interesting plasmonic and photonic LSPR features, very sharp resonances that can be exploited to make high sensitivity sensors.[25,83-88] In this thesis, gold nanorod arrays were designed, fabricated, and tested for chemical and biological sensing capabilities.

1.4 Near-Field Imaging

Visualizing the electric near-field of nanoparticles is important for understanding the plasmonic behavior of the particles. Maxwell's equations predict different electric

field characteristics resulting from the charge distributions and changing electric fields, labeled as far- and near-fields, respectively.[45-46] Figure 3 shows an illustration of the difference in far- and near-fields. By imaging the electric near-fields resulting from different excitation wavelengths, we can observe the plasmonic modes of metallic nanoparticles and compare the features to simulated predictions.

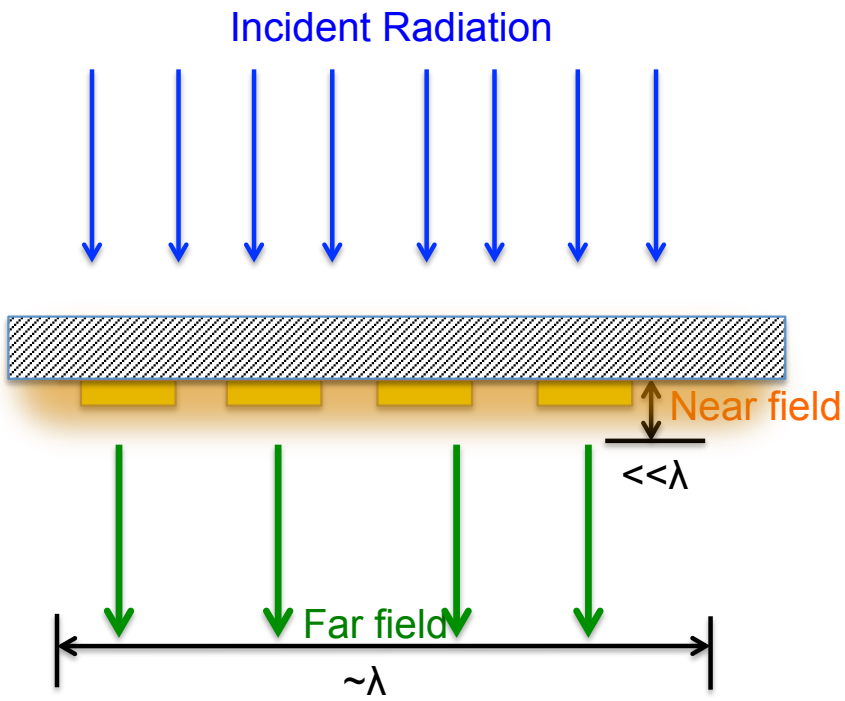

FIGURE 3: ILLUSTRATION OF NEAR AND FAR FIELD OPTICS

An illuminated surface of nanoparticles generates a near electromagnetic field in the sub wavelength length scale and a far electromagnetic field on the order of the wavelength of incident radiation.

Near-field scanning optical microscopy (NSOM), illustrated in Figure 4, is a near-field imaging technique whose resolution is limited by the detector aperture used rather than the far-field diffraction limit. By placing the detector less than one wavelength of light away from the particle, the information from the evanescent field can be used to construct images of the electric near-field. NSOM techniques can be limited by long collection times, tip heating, tip quality, surface quality, difficulty with image contrast, and the requirement for very sensitive detectors.[47-48] Other near-field imaging techniques include photochemical imaging, total internal reflectance microscopy, near-field infrared spectrometry, near-field dielectric microscopy, and scanning tunneling microscopy. [46]

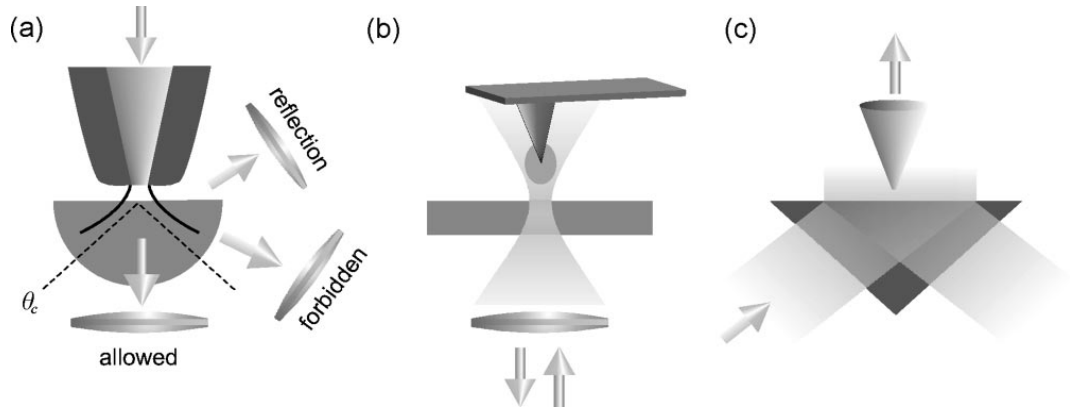

FIGURE 4: ILLUSTRATION OF DIFFERENT TYPES OF NEAR-FIELD OPTICAL MICROSCOPIES

a) Aperture SNOM with angular resolved detection, b) apertureless configuration, and c) scanning tunneling optical microscope. Adapted from Hecht et al.[49]

Photochemical near-field imaging is a technique that makes use of the conformational change of the azobenzene molecule to induce topographical changes in polymer films. The azobenzene molecules are grafted to a polymer chain to create a photosensitive, dynamic polymer. When a thin film of this polymer is coated over a nanoparticle and excited by an external electric field, the excited near-field of the nanoparticle will cause molecular motion of the polymer. This motion occurs most in areas of high electric field gradient, so that the topography of the polymer surface becomes a map of the near-field of the particle. These topographical changes are imaged and quantified by atomic force microscopy, which has an extremely high sensitivity in the vertical direction.

While NSOM requires very complex setup and expertise, photochemical imaging is based on the more basic and ubiquitous AFM. The static nature of the topographical image of the polymer surface allows for the separation of the near-field excitation and the imaging of the near-field.[50-51] Studies of the electric near-field at varying heights above the surface of the particle have been demonstrated using different polymer thicknesses.[52] Photochemical imaging has demonstrated the nanometer-scale resolution of AFM and theoretically could be sensitive to the motion of an individual molecule.[53-55] Photochemical imaging also has the potential to image the near-field modes of any excitation wavelength, based on the light sources available rather than the imaging technique.

In this thesis work, the modes of gold bowtie antenna arrays in the visible spectrum were imaged using photochemical near field imaging. Furthermore, a recipe was developed to use two-photon absorption based molecular motion to image modes in the near infrared spectral range, which is usually not accessible by single photon absorption.

1.5 SURFACE ENHANCED RAMAN SCATTERING

Raman scattering spectroscopy can be used to observe the vibrational modes of molecules. Surface enhanced Raman scattering (SERS) makes use of the localized electric near-field of nanoparticles to increase the Raman scattering of molecules, since both the incoming and the scattered electromagnetic fields are dramatically enhanced. Metallic nanostructures including both chemically synthesized nanoparticles and nanostructures by top-down fabrication have been demonstrated as effective SERS substrates, which can be used towards highly sensitive and specific biosensing.[56]

In SERS experiments, illustrated in Figure 5, the sample is excited by a laser and the Raman scattered light passes through a spectrometer and is measured by a detector.

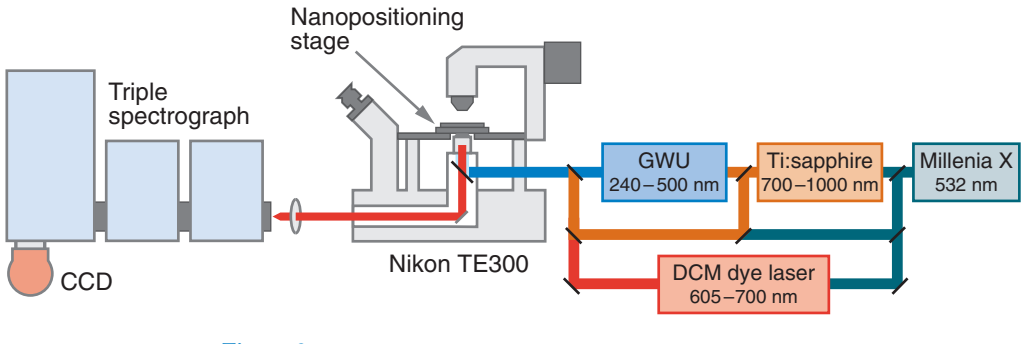

FIGURE 5: ILLUSTRATION OF SURFACE ENHANCED RAMAN SCATTERING SPECTROSCOPY EXPERIMENTAL SETUP

Experimental setup for measuring surface-enhanced Raman scattering in an epi-illumination geometry using a wavelength-scanned laser-excitation system and a triple spectrograph coupled with a charge-coupled device (CCD) camera. Adapted from Willets et al.[15, 29]

When light interacts with matter, there is a certain probability that the light will be scattered, elastically or inelastically.[57] The Raman effect, illustrated in Figure 6, occurs

because of the inelastic scattering of incident light, which shifts the frequency by the energy of the molecule's characteristic vibrations. Data analysis techniques have made it possible to analyze the Raman spectra in order to draw conclusions about the chemical structure and composition of Raman markers.[58] The small Raman scattering cross sections of most molecules implies the need for large numbers of molecules to achieve adequate conversion from excitation photons to Raman photons.[19, 59-60]

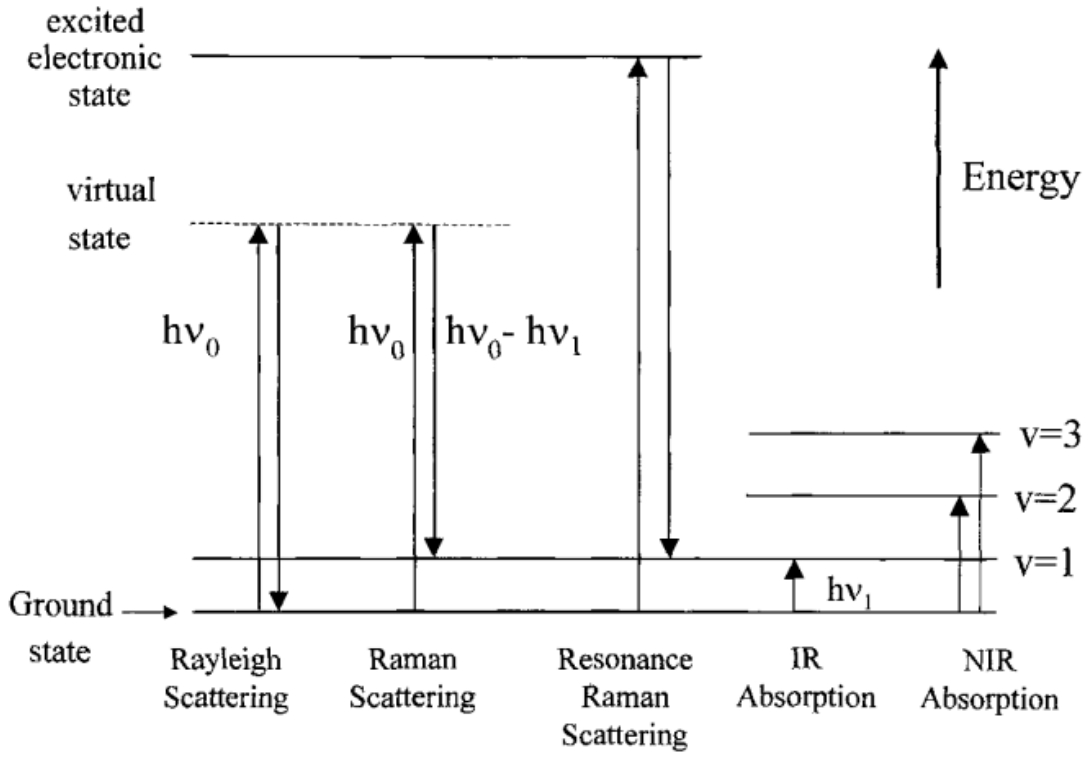

FIGURE 6: ILLUSTRATION OF VIBRATIONAL SPECTROSCOPIC TRANSITIONS

Electronic transitions of the interaction of light with matter through scattering and absorption. These interactions for the basis for several types of spectroscopic techniques. Adapted from McCreery.[57]

SERS biosensing makes use of the enhanced local electric fields of plasmonic devices to increase the Raman signal of biomolecules and biomarkers. SERS involves the adsorption of a molecule in the hotspot of a nanoparticle, where the increased electromagnetic field causes an increase in Raman cross-section and hence an increase in Raman signal, as illustrated in Figure 7. This means that lower concentrations of biomarkers produce readable signatures and allow for detection of lower sample volume or very low concentration samples.

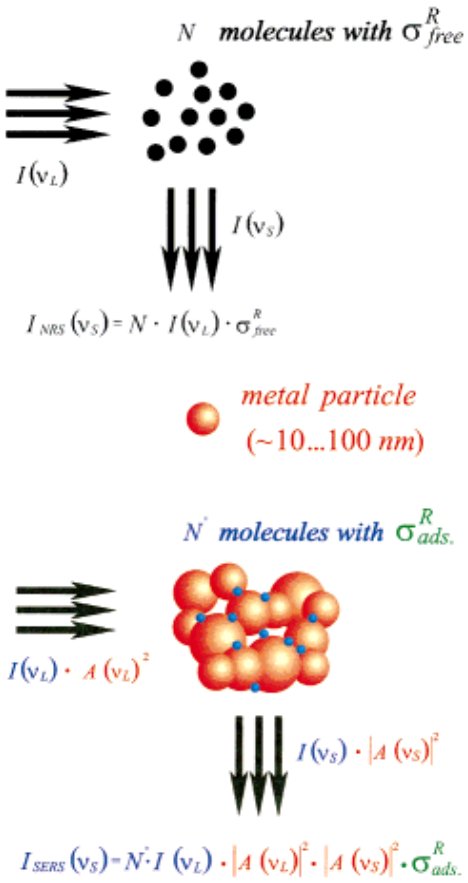

FIGURE 7: ILLUSTRATION OF SURFACE ENHANCED RAMAN EFFECT

Comparison of "normal" (top) and surface-enhanced (bottom) Raman scattering. The conversion of laser light I_L into Stokes scattered light I_{NRS} is proportional to the Raman cross section σ_{Rfree}, the excitation laser intensity I_L, and the number of target molecules N in the probed volume. Figure 1b displays a schematic of a SERS experiment. σ_{Rads} describes the increased Raman cross section of the adsorbed molecule ("chemical" enhancement); $A(\nu_L)$ and $A(\nu_S)$ are the field enhancement factors at the laser and Stokes frequency, respectively; N′ is the number of molecules involved in the SERS process. Adapted from Kneipp et al.[58]

The Raman enhancement factor is a quantitative measure of the increase in Raman signal due to the enhanced electric field in SERS substrates. The enhancement factor, EF, is given by:

$$EF = \left(\frac{N_{bulk}}{N_{SERS}}\right)\left(\frac{I_{SERS}}{I_{bulk}}\right) \qquad (1\text{-}22)$$

where N_{bulk} is the number of molecules in the bulk sample, N_{SERS} is the number of molecules on the SERS sample, I_{bulk} is the intensity of the Raman signal for the bulk sample, and I_{SERS} is the intensity of the Raman signal for the SERS sample.

In this thesis work, gold bowtie antenna arrays were designed, fabricated, and tested for the effects of various geometrical parameters on the SERS EF of naphthalene thiol.

1.6 ORGANIZATION OF THIS THESIS

The introduction chapter has given a brief overview of plasmonics and its applications in biosensing. This included a conceptual overview of the theory and techniques involved in localized surface plasmon resonance and surface enhanced Raman scattering spectroscopies, as well as near-field imaging.

The second chapter will describe the discrete dipole approximation and the development of a simulation recipe within the DDSCAT program. The effects of grid spacing and substrates, including effective mediums, on computational time and simulation accuracy were studied.

The third chapter will describe the development of nanofabrication techniques optimized to achieve very fine features and very small gaps between features. Various parameters involved in the electron beam lithography process, such as electron beam dosage, deposition rate, and liftoff method, were tested in order to push the limit of current fabrication of very small features. Using the developed recipe, features as small as 15 nm line widths and 3 nm gaps between features were achieved.

The fourth chapter will describe the development of nanorod arrays for LSPR-based biosensing. Nanorods were fabricated in a variety of rectangular arrays to achieve very sharp resonances. Geometrical particle and array parameters were used to tune and sharpen the resonance. Refractive index sensitivity of 360 nm/RIU was achieved. DNA was detected in concentrations as low as 0.1 aM.

The fifth chapter will describe the experimental technique of photochemical near-field imaging of nanoparticles. The photosensitive polymer, DR1MA, was used to image the electric near field of various geometries of bowtie nanoantennae. A recipe was developed to use the two-photon absorption of DR1 to induce molecular motion for near field imaging.

The sixth chapter will describe the experimental and simulated characterization of bowtie nanoantennae for the optimization of a SERS-based biosensor. Bowtie nanoantennae were fabricated in a variety of geometries, including gaps as small as 3 nm. The near field and far field were characterized computationally and experimentally. SERS enhancement factors as high as 10^{11} were achieved.

The final chapter will give a broad overview of the conclusions of this thesis work. The applications of the plasmonic structures studied in this thesis work in the field of biosensing will be discussed.

2 CHAPTER 2: SIMULATION

2.1 COMPUTATIONAL ANALYSIS OF NANOPARTICLE SCATTERING

By simulating different geometrical and material parameters we can gain insight into, and start to understand, complex systems. Simulation of nanoparticles and nanoparticle arrays can be used to tune the LSPR and achieve the highest electric field enhancement that is theoretically possible. By isolating and varying simulation parameters we can identify modes of excitations, and correlate the near field and far field features.

2.1.1 DISCRETE DIPOLE APPROXIMATION

The discrete dipole approximation (DDA) is a calculation method to compute the scattering of electromagnetic radiation by any arbitrary objects. The basic idea was first proposed by H. Devoe, developed and improved by E.M. Purcell and C.R. Pennypacker, and further developed by B.T. Draine, and P.J. Flatau.[61-63] DDA was inspired by the work by Lorentz showing the correlation of the dielectric properties of a substance to the polarizabilities of its constituent atoms through the Clausius-Mossotti relation[64-68]:

$$\frac{\epsilon - \epsilon_0}{\epsilon + 2\epsilon_0} \cdot \frac{M}{d} = \frac{4\pi N_A \alpha}{3}$$

where ϵ is the dielectric constant of the substance, ϵ_0 is the permittivity of a vacuum, M is the molar mass of the substance, d is the density of the substance, N_A is Avogadro's number, and α is the molecular polarizability.

By representing an object of arbitrary shape by numerous individual point dipoles, as shown in Figure 8, the scattering can be solved exactly using Maxwell's Equations. By describing the location and polarizability of each dipole, any material can be described and its interaction with plane-wave monochromatic light can be computed.

Discrete Dipole Scattering (DDSCAT) is one of the most popular applications of DDA, developed by B. T. Draine and P. J. Flatau in 1988, that calculates the absorption and scattering properties of objects with arbitrary geometries and dielectric properties.[63, 69-74] Though originally developed for astronomic simulation, the program has since been adapted for noble metal nanostructures.

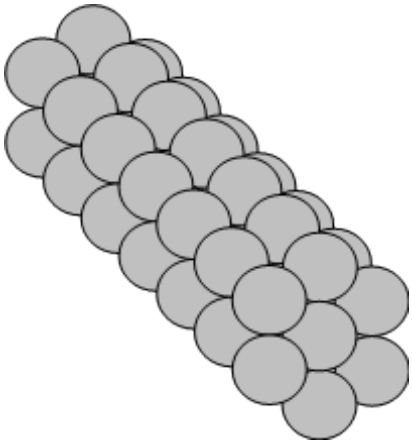

Figure 8: Illustration of the discrete dipole approximation (DDA) of a nanowire

Section of a nanowire represented by discretized spherical dipoles, as used in the DDA method

In DDSCAT, an array of dipoles, for $j = 1, \ldots, N$, each with polarizabilities α_j, are each located at $\boldsymbol{r}_j$. The polarization, $\boldsymbol{P}_j$, of each dipole is:

$$\boldsymbol{P}_j = \alpha_j \boldsymbol{E}_j \qquad (2-1)$$

where $\boldsymbol{E}_j$ is the electric field at r_j. The electric field at r_j is given by:

$$\boldsymbol{E}_j = \boldsymbol{E}_{inc,j} - \sum_{k \neq j} \boldsymbol{A}_{jk} \boldsymbol{P}_k \qquad (2-2)$$

Which consists of the incident wave:

$$\boldsymbol{E}_{inc,j} = \boldsymbol{E}_0 e^{(i\boldsymbol{k}\cdot\boldsymbol{r}_j - i\omega t)} \qquad (2-3)$$

and the contribution from all other dipoles:

$$-\sum_{k \neq j} \boldsymbol{A}_{jk} \boldsymbol{P}_k \qquad (2-4)$$

where:

$$\boldsymbol{A}_{jk} = \frac{e^{ikr_{jk}}}{r_{jk}} \times \left[k^2 \left(\hat{r}_{jk} \hat{r}_{jk} - \mathbf{1}_3 \right) + \frac{ikr_{jk} - 1}{r_{jk}^2} \left(3\hat{r}_{jk} \hat{r}_{jk} - \mathbf{1}_3 \right) \right], j \neq k \qquad (2-5)$$

where $k \equiv \omega/c$, $r_{jk} \equiv \left| r_j - r_k \right|$, $\hat{r}_{jk} \equiv \left(\boldsymbol{r}_j - \boldsymbol{r}_k \right)/r_{jk}$, and $\mathbf{1}_3 \equiv 3\times3$ identity matrix.[69]

The boundary conditions of the system can either be infinite, for simulating a finite particle, or periodic, for simulating an array of particles. With infinite boundary conditions, the interaction of the defined particle is calculated for an expanding area of surrounding dielectric medium. When the calculation converges and no further area expansion causes any significant change to the results, the boundary conditions are considered infinite and the calculation stops. A similar procedure occurs for periodic boundary conditions. The initial particle is replicated at the user-defined one, two, or three-dimensional interval, and the interaction between particles is calculated. Then this replication and calculation step is repeated with expanding boundaries until the data converges, at which point the calculation stops and infinite periodic boundary conditions are considered achieved.

The electric field is calculated for each dipole. The information can be used to calculate the electric field intensity and thus the average and maximum intensities over the nanoparticle surface. The information can also be used to make a contour plot of the intensity on and around the nanoparticle in order to visualize the locations of hotspots.

The extinction cross section denotes the area of incident light that is likely to interact with a particle, and is a combination of the absorbance and scattering cross sections. The extinction efficiency is the ratio of extinction cross section to the geometrical cross section of the nanoparticle. The extinction efficiency is simulated in DDSCAT for multiple wavelengths to create a spectrum used to determine the theoretical resonance position of the particle.

2.1.2 Effective Medium Theory

When taking into account the effects of substrates on nanoparticle systems, one can add a DDA dipole representation of a dielectric or use the effective medium theory to approximate the effects.[75-76] The effective medium theory approximates the properties, usually dielectric constant and conductivity, of composite materials based on the relative fractions of its components, as given by:

$$\varepsilon_{eff} = \varepsilon_m \frac{\varepsilon_i(1 + 2\delta_i) + 2\varepsilon_m(1 - \delta_i)}{\varepsilon_m(2 + \delta_i) + \varepsilon_i(1 - \delta_i)}$$

where ε_m is dielectric constant of the original material, ε_i is the dielectric constant of the inclusion material, δ_i is the fraction of inclusion material. The refractive index of a dielectric material is related to the dielectric constant as:

$$\tilde{\varepsilon} = \varepsilon_1 + i\varepsilon_2 = (n + ik)^2$$

where $\tilde{\varepsilon}$ is the complex dielectric constant, ε_1 is the real part of the dielectric constant, ε_2 is the imaginary part of the dielectric constant, n is the real part of the refractive index, and k is the imaginary part of the refractive index.[77]

In this chapter, simulations were run to determine how simulation parameters affect the results and computation time. This provides a general guideline to design and tune the parameters for nanofabrication. Finding a compromise between accuracy and feasibility is important in developing a simulation recipe. The correlation between grid spacing, accuracy, and computation time was tested. The addition of a substrate was studied for its effects on the system. In addition, the effects of a substrate were approximated using the effective medium theory.

2.2 Simulation Parameter Testing

Simulation of the particle scattering was carried out using the DDA in the DDSCAT program.[69, 74] DDSCAT version 7.0 was used for all simulations. The dielectric constants of Au and silica are taken from Johnson and Christy.[78] The particle scattering electric field intensity over the nanoparticle surface was calculated for isolate targets. The information was used to make contour plots of the intensity on and around the nanoparticle to visualize the location of the hotspots. The extinction efficiency was simulated for multiple wavelengths to produce spectra used to determine the resonance position of the particle.

2.2.1 Effect of Grid Spacing

Grid testing is important for determining the maximum grid spacing that is accurate for the system. As the grid spacing is decreased the number of dipoles increases, which increases the computation time. Therefore the largest grid spacing, meaning the least number of dipoles, that is accurate for the system should be determined. The grid spacing is controlled by adjusting the shape parameters and effective radius. When optimizing the grid spacing of a system, the largest grid spacing of the planned series is run first. Then the grid spacing is adjusted smaller incrementally until the data has converged. When the data converges the largest accurate grid spacing can be determined.

The grid spacing used for DDA calculations determines both the accuracy of the simulation and the computational time required. Generally speaking, calculation using a

smaller grid spacing is more accurate than using a larger grid spacing. As the size of the grid decreases, more dipoles are required to make up the specified geometry of the particle to be simulated, thus requiring more complex calculations.

Different grid spacings were tested for computational time and accuracy. A single gold triangular prism of side length 150 nm and thickness 45 nm was used for all tests. The resulting plots of optical properties and computational time variation with grid spacing are shown in Figure 9. The simulation starts to become increasingly computationally intense for grid spacings less than 4 nm. The resonance peak position and shape starts to change for grid spacings less than 4 nm. From these observations, 4 nm was determined to be the maximum grid size that should be used for this system. The difference in computation time between 1 nm and 1.5 nm is significantly more than the difference between 2 nm and 1.5 nm.

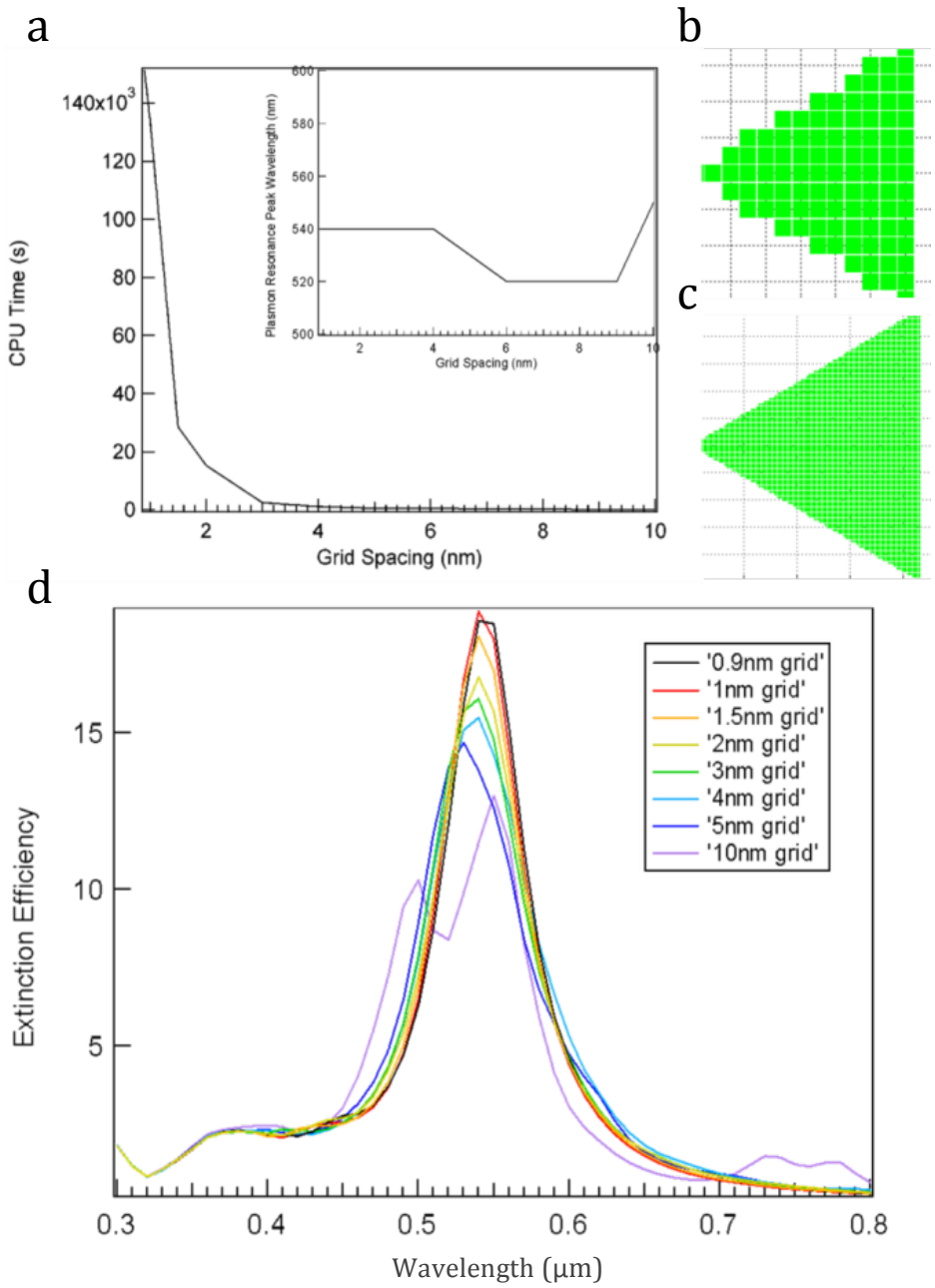

Figure 9: Grid Spacing Test

a) Plot of computation time for varying grid spacings. Inset: plot of resonance wavelength for different grid spacings. b) 10 nm grid spacing. c) 1.5 nm grid spacing. d) Plot of extinction efficiency spectra for different grid spacings.

A grid of 4 nm was determined to be the maximum accurate spacing for this system that did not drastically increase the computation time. Larger or more complex systems may have different grid spacing requirements. This method of testing grid spacing should be carried out each time a new particle geometry is developed. For each system simulated, depending on accuracy requirements, geometry details, and

computational time limitations, there will be an ideal grid spacing. Smaller features and particle size require a smaller grid size to better approximate the features.

2.2.2 SUBSTRATE EFFECT TEST

The substrate, or dielectric environment, of a particle can have an effect on the optical properties and electric field of the particle. As a substrate is added and increases in size relative to the particle, the effects on optical and electric field properties should reach a plateau. The addition of a substrate to a system can affect the extinction spectra by red shifting and peak broadening. As the substrate increases in size the number of dipoles increases, which increases the computation time. Therefore, the smallest substrate size that is accurate for the system should be discovered and used. The substrate size is controlled by the DDSCAT shape parameters and effective radius. When testing a series of substrate sizes, the smallest substrate in the series is run first followed by increasingly larger substrates until the data converges. When the data converges the smallest accurate substrate size can be determined.

Different substrate sizes were tested for a gold triangular prism with 150 nm side length and 45 nm thickness (H). A grid spacing of 4 nm was used for the system. A series of tests were run holding the thickness or radius of a cylindrical substrate constant while varying the other, as shown in Figure 10e and f. A prism with no substrate had a resonance wavelength of 620 nm. In Figure 10a, the radius was kept constant at 263 nm (3R) while the thickness was varied from 45 nm (H) to 182 nm (4H). In Figure 10c, the radius was kept constant at 351 nm (4R) while the thickness was varied from 45 nm (H) to 137 nm (3H). In Figure 10d, the thickness was kept constant at 91 nm, twice the thickness of the gold prism (2H), while the radius was varied from 88 nm (R) to 439 nm (5R). For increasing substrate size, the resonance red shifted dramatically when the substrate size was similar to the prism size, followed by a blue shift and convergence when the dielectric was acting as a substrate.

A cylindrical substrate with radius 263 nm and thickness 91 nm was found to be the minimum size of substrate that gave accurate substrate effect results. A substrate smaller than this was found to produce coupling effects due to the substrate being on the same order of magnitude of size as the particle. For each particle system simulated it would be necessary to find the minimum substrate size that causes convergence in the resonance shift.

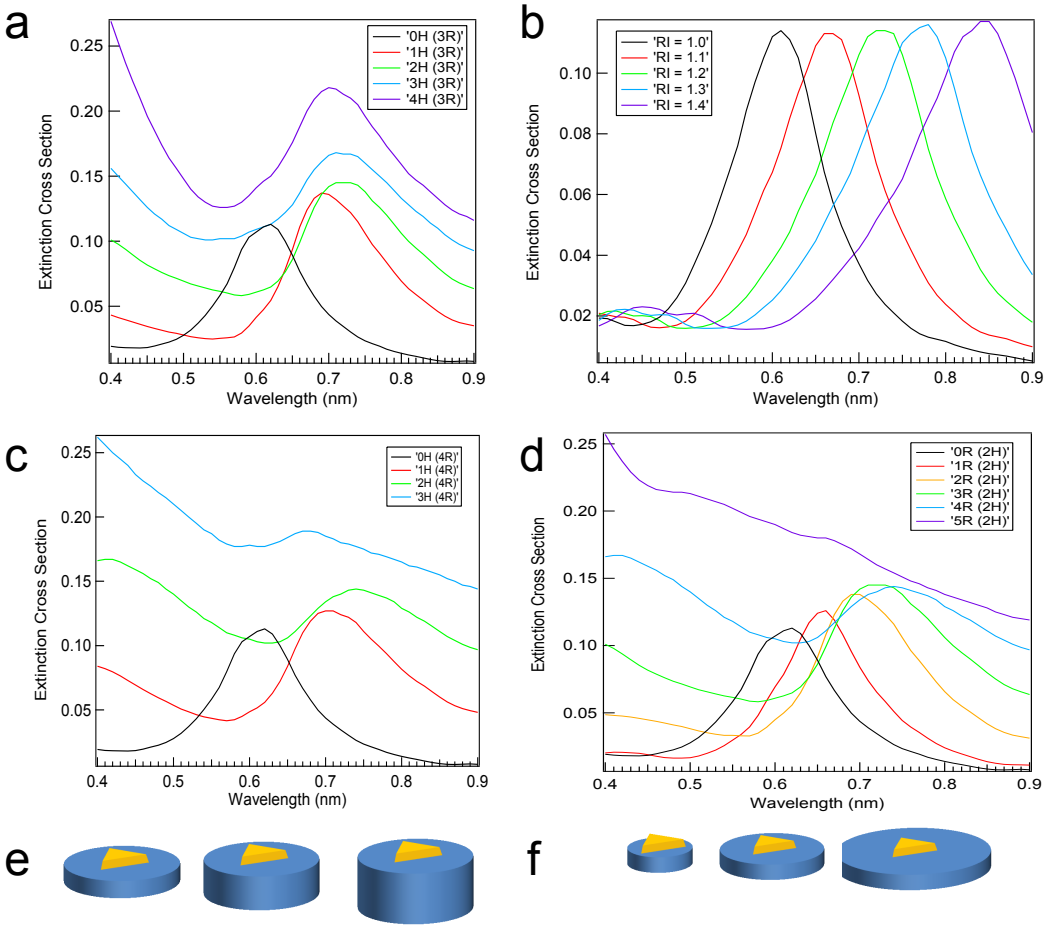

FIGURE 10: SUBSTRATE TEST

a) Plot of extinction cross-section for different substrate height with a constant substrate radius 3R. b) Plot of extinction cross-section for different effective medium values. c) Plot of extinction cross-section of different substrate height with a constant radius of 4R. d) Plot of extinction cross-section for different substrate radii with a constant substrate height 2H. e) Illustration of increasing substrate height with a constant substrate radius. f) Illustration of increasing substrate radius with a constant substrate height.

2.2.3 Effective Medium Test

The effective medium theory can be used to approximate the effects of a substrate. The refractive index of the surrounding medium of the system can be adjusted to approximate the resonance peak of different substrate sizes. By adjusting the effective medium of the system the effects of a substrate can be approximated with much less computation time than simulating a real substrate. The effective medium theory suggests

that the red shifting effects of a substrate can be approximated by increasing the refractive index of a homogenous surrounding medium.

Different effective medium calculations were tested for a gold triangular prism with side length 150 nm and thickness 45 nm. A grid spacing of 4 nm was used for the system. First, an effective medium was calculated using a weighted average, taking into account the actual amount of surface in contact with air and with silica. The total area in contact with air was 29,993 nm^2. The total area in contact with silica was 9,743 nm^2. The effective refractive index was calculated to be 1.105. The resonance wavelength for a prism in a medium with refractive index 1.105 is 670 nm.

Next, an effective medium was calculated using a weighted average assuming the amount of area in contact with air was the same as the amount of area in contact with silica. The area used for both was the area of the triangular face of the prism, 9,743 nm^2. The calculated effective refractive index was 1.215. The resonance wavelength for a prism in a medium with refractive index 1.215 is 730 nm.

Tests were also run for media with refractive indices 1.0, 1.3, and 1.43. A prism in air, refractive index 1.0, had a resonance wavelength 610 nm. A prism in a medium with a refractive index 1.3 had a resonance wavelength 780 nm. A prism in silica, with a refractive index of 1.43, had a resonance wavelength of 850 nm.

An effective medium with refractive index of 1.215 was found to approximate a 263 nm radius and 91 nm thick cylindrical substrate of silica for a 150 nm side length and 45 nm thick Au prism. When simulating a new system, substrate and effective medium tests should be run to optimize the parameters for accuracy and minimal computational time. For a new simulation system, where the effects of a substrate are known, the effective medium theory can be used to approximate that effect by simulating a dielectric environment with an increased refractive index.

2.3 CONCLUSIONS

For each system of nanoparticle simulation, there is a set of parameters that must be determined for efficient balance of accuracy and computation time. From testing various simulation parameters, the ideal grid spacing and effective medium can be

determined. In this chapter, an example of a triangular prism was tested for grid spacing and substrate effects.

When testing the grid spacing of a particle, it is important to determine a balance between accuracy and computational time. Testing different grid spacings for a triangular prism showed an exponential increase in computational time with decreasing grid spacing. Subjectively evaluating the computation cost for accuracy, one can determine the smallest feasible grid spacing for each system.

The substrate effects on a nanoparticle system are important to include for comparison with experimental conditions. The inclusion of a dielectric substrate with a nanoparticle red shifts the resonance while the substrate size is on the order of the particle size. As the substrate becomes comparatively large, the resonance blue shifts slightly and eventually converges. The smallest piece of dielectric that acts as a true substrate is preferable in order to minimize the computational time.

Substrate effects can be approximated by the effective medium theory. The effective medium theory states that the red shift induced by the addition of a dielectric substrate can be approximated by increasing the refractive index of the homogeneous dielectric medium. Each system of nanoparticles simulated can be tested to find the refractive index that gives the best match to substrate effects. Alternatively the refractive index can be tested in order to match it to experimental conditions.

3 CHAPTER 3: FABRICATION

3.1 NANOFABRICATION

The goal of this fabrication work was to develop a recipe to obtain the smallest features possible using electron beam lithography. The objective was to push the limits of current fabrication abilities to achieve feature sizes in the range of 15 nm line widths and 5 nm gaps between features. A fabrication recipe for electron beam lithography was developed for nanoparticle arrays, shown in Figure 13, and the results were characterized using a variety of techniques including scanning electron and atomic force microscopy.

High quality fabrication is important for plasmonic devices. Small gaps between features and sharp corners have been shown to exhibit much higher localized electric field hotspots.[13, 79] Therefore, the optimization of a fabrication recipe, leading to precise control of small features, is key to manipulating plasmonic properties of nanoparticles.

The geometries of nanoparticles designed in simulation can be fabricated for experimental characterization and the results compared between simulation and experiment. High quality, repeatable fabrication can increase the comparability of experiment to simulation and attempt to recreate the conditions of theoretical computation.

There are many types of nanofabrication that yield high quality, complex structures: the chemical synthesis and assembly of structures;[2, 80-83] using a physical mask for patterning metal deposition or etching, such as in nanosphere lithography;[2, 84-85] exposing resist in patterns using patterned light, as with laser interference, or by using masks, as in optical lithography.[86]

Wet chemical synthesis, an illustration of which is shown in Figure 11, is capable of producing large quantities of high-quality nanoparticles in a variety of shapes and sizes.[87] The bottom up approach to nanoparticle fabrication involves solution synthesis and filtering of nanoparticles that leads to high quality and uniformity. The particles can be used in solution for colorimetric analyte detection or deposited on a substrate for use with other spectroscopic techniques. Deposition of synthesis particles can result in either random dispersion or orderly monolayers, which limits the periodicities available for array-based photonic properties.[2, 80-83]

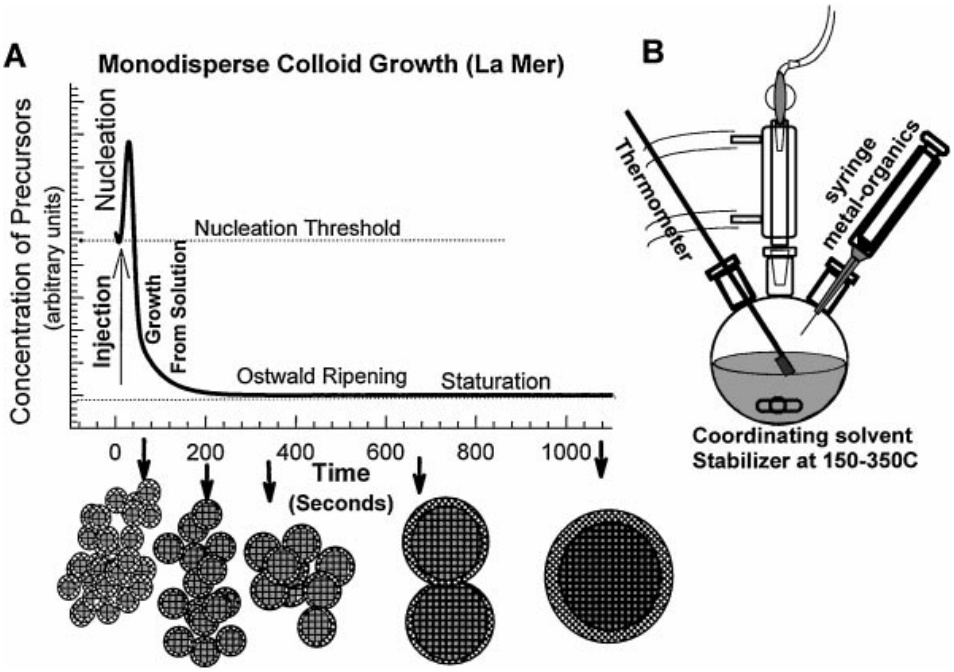

FIGURE 11: ILLUSTRATION OF WET CHEMICAL SYNTHESIS OF COLLOIDAL NANOPARTICLES

A) Cartoon depicting the stages of nucleation and growth for the preparation of monodisperse nanoparticles in the framework of the La Mer model. As nanoparticles grow with time, a size series of nanoparticles may be isolated by periodically removing aliquots from the reaction vessel. (B) Representation of the simple synthetic apparatus employed in the preparation of monodisperse nanoparticle samples. Adapted from Murray et al.[88]

Nanosphere lithography (NSL), illustrations of which are shown in Figure 12, uses a physical mask of polystyrene spheres for metal deposition that results in hexagonal arrays of triangular prisms.[89-90] Being inexpensive, rapid and parallel as well as having flexible particle shape and spacing make NSL an attractive plasmonic biosensing platform. NSL is capable of particle sizes on the order of 100 nm, but is limited in array and particle geometries.[91-92]

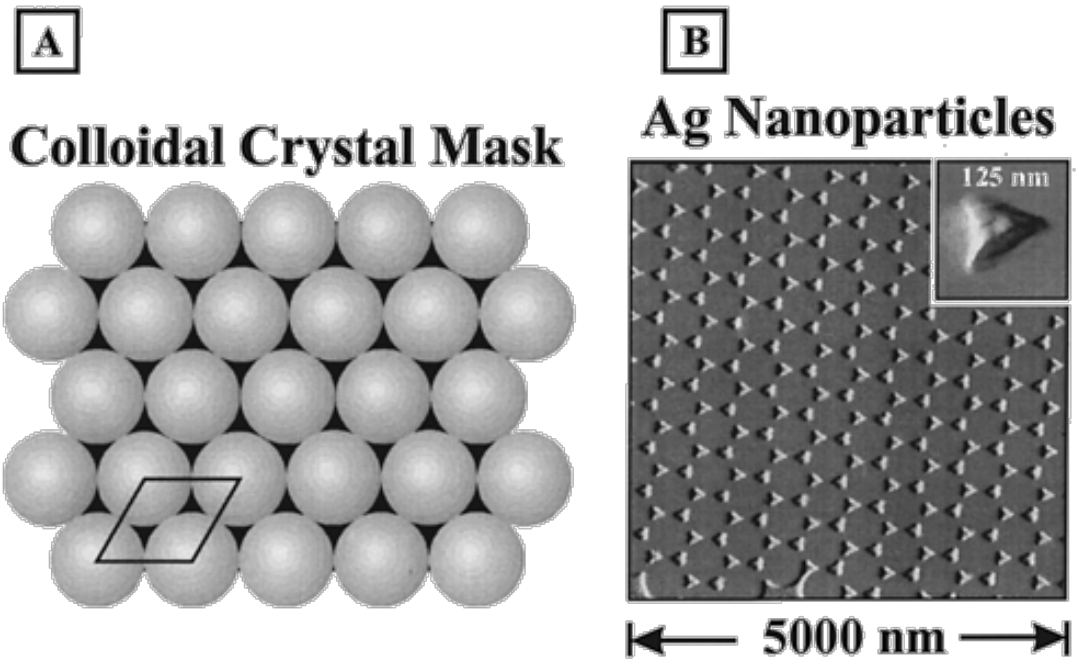

FIGURE 12: ILLUSTRATION OF NANOSPHERE LITHOGRAPHY

a) Schematic illustration and b) representative AFM image of typical nanosphere lithography fabrication setup and results. Adapted from Haynes et al.[92]

Lithographic techniques, both optical and electron beam, can be used to fully control the particle positions and shape. First, a thin layer of polymer resist spin-coated onto the substrate and a radiation source is then used to expose a pattern in the resist. The exposed regions are rendered more soluble for positive resist, while negative resists are cross-linked and polymerized, making them less soluble. The chip and the polymer are then rinsed in a developer solution to wash away the inside or outside of the pattern for positive and negative resists, respectively. In this work, a positive polymer resist was used. After being rinsed in a developer solution metal is deposited onto the top of the polymer and the exposed areas of the substrate. The remaining polymer and its accompanying metal is lifted off using a resist solvent, such as acetone, leaving just the metal on the substrate, in the desired pattern, examples of which are shown in Figure 13. An illustration of the procedure for electron beam lithography is shown in Figure 14.

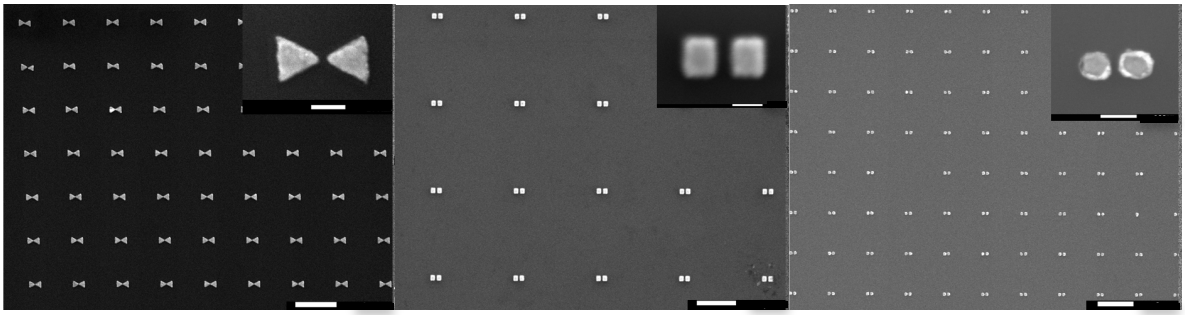

FIGURE 13: EXAMPLES OF EBL FABRICATION RESULTS USING AREA DOSAGE

Triangular (left), square (middle), and circular (right) nanoparticle dimer arrays. Scale bars are 1 μm. Insets show high magnification images of individual dimers. Scale bars are 100 nm.

Optical lithography has a diffraction-limited resolution of ~λ/2, which leads to feature sizes around 1 μm. However, the use of various techniques, such as ultraviolet lasers and high numerical aperture optics, allows for photolithography capable of feature sizes on the range of 300 nm.[93-95]

Electron beam lithography (EBL) is capable of making finely controlled patterns with very small feature size, on the nanometer scale.[40, 94, 96-97] Using various modifications to the fabrication procedure, EBL has been used to fabricate structures with linewidths as small as 10 nm and gaps between features as small as 8 nm.[96-97]

Many factors in the fabrication process can influence the quality of the resulting patterns. Metal adhesion layers are sometimes required during fabrication if there is poor adhesion between the substrate and desired pattern metal. Evaporation angles can result in mismatches in overlapping metal layers, similar to inadvertent shadow evaporation, that can distort fine features. The electron beam dosage must be carefully tuned according to the hardness of the resist, the beam current, and the feature proximity. Over-exposure leads to enlarged, distorted features and small gaps are filled in. Under-exposure leads to weak feature definition or no feature.

Poor quality patterns can cause discrepancies that affect the comparability of experimental and simulated results. Surface roughness resulting from the various metal deposition methods can cause the existence of unexpected hotspots in the resulting crevices, which are very hard to account for in simulations. The corners and edges created in most simulation software are perfectly straight, however, during fabrication these features can be rounded or curved to varying degrees.

Characterization techniques can be used to confirm successful fabrication and to compare with simulation. Scanning electron microscopy (SEM) confirms that the fabrication was successful through high magnification imaging of the structures produced with EBL. SEM imaging allows for the careful examination of the surface quality, shape, and scale of features. Optical microscopy can only image features larger than a wavelength of light, and so does not have the resolution necessary to image features on the nanoscale, such as the nanoparticle arrays fabricated for this project. Using atomic force microscopy (AFM) confirms the height of features and the surface quality of particles.

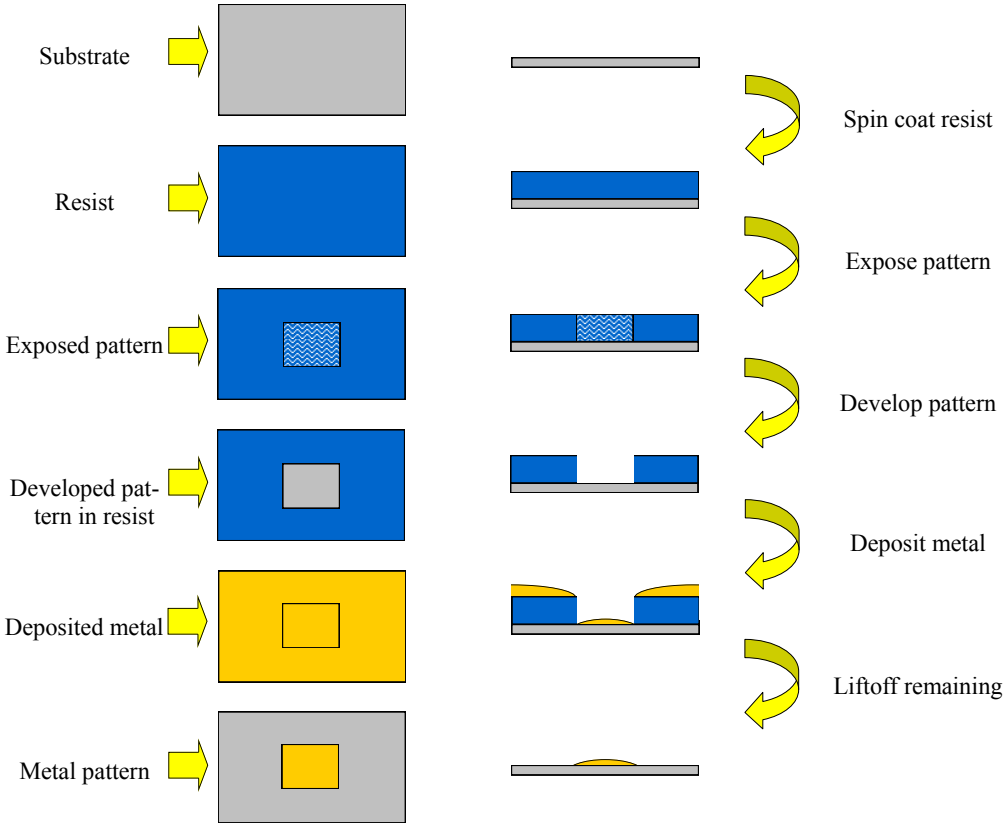

Figure 14: Illustration of Electron Beam Lithography Process

(top to bottom) Bare substrate is spin coated with a polymer resist. Polymer resist is exposed in desired pattern (in this example pattern is a rectangle) by an electron beam. Exposed pattern in resist is washed away using a developer solution. Metal is deposited over resist and bare pattern. Polymer resist is washed away removing metal on top, leaving only metal deposited in bare pattern area.

3.2 Electron Beam Lithography Process

3.2.1 ELECTRON BEAM LITHOGRAPHY

When testing different bake times a VWR 635HF hot plate was used to bake the chips at 180 °C. An accurate and stable temperature was ensured using an Omega Engineering Model CL23A Calibrator-Thermometer K-type thermocouple. A gradient in hotplate surface temperature was observed so all baking was done on the exact center of the hotplate. A silicon substrate was used for all bake time tests. The same polymer layer, 950 PMMA A4, was used for all chips. The PMMA was spin coated onto the chips using a Specialty Coating Model P6700 spin coater. The PMMA was spun at 4,000 rpm for 40 seconds.

Dosage testing was done on a JOEL JSM-7001F field emission scanning electron microscopy (FESEM) with DEBEN PCD Beam Blanker EBL configuration. Testing was done using a line spacing of 19 nm. All chips used were silicon substrate with a layer of PMMA baked for 15 minutes at 180 °C. All tests were developed for 75 seconds.

Development times were tested on silicon substrate chips with a PMMA layer baked at 15 min. A solution ratio of 1:3 methyl isobutyl ketone (MIBK)/isopropyl alcohol (IPA) was used as a develop solution. All tests were done at room temperature. After development the chips were rinsed for 20 seconds in IPA and blown dry using nitrogen gas or compressed air.

Metal evaporation was done in an Elite Engineering Thermal Evaporator. A chamber pressure of at least $7x10^{-7}$ Torr was used for evaporation.

Metal liftoff was done in room temperature acetone for at least 2 hours followed by sonication for 1 to 2 minutes at power level 2 in a Crest Ultrasonics Powersonic P1100D sonicator.

3.2.2 SCANNING ELECTRON MICROSCOPY IMAGING

Imaging was performed using a JOEL JSM-7001F FESEM. The astigmatism and wobble were carefully adjusted utilizing a standard sample of gold nanoparticles approximately 100 nm in diameter. The focus was carefully adjusted for each image location. The magnification was adjusted to maximize the spatial resolution of the image. The smallest beam current possible, typically around 34 pA, was used for all imaging. An acceleration voltage of 15 kV was used for all imaging. The scan speed was adjusted to ensure an accurate scan of the sample for a high resolution image. The weakest beam

current and acceleration voltage feasible were used and the focus and magnification were adjusted as quickly as possible in order to minimize charging effects.

3.2.3 Atomic Force Microscopy Imaging

AFM imaging was done a Digital Instruments Veeco Nanoscope V. The height scale and amplitude error were adjusted so as to be as small as possible but still include all features inside the plot, typically less than 100 nm and 100 mV, to give maximum feature contrast. The cleanliness of the sample was ensured by blowing with nitrogen gas or compressed air in order to avoid obscuring the image of the sample with dirt particles. A slow scan speed of 1 Hz was used to ensure an accurate reading of the height. The pixels per scan were adjusted to 512 to maximize the resolution of the image.

3.3 Electron Beam Lithography Parameter Testing

In order to optimize the fabrication recipe to achieve the smallest features possible, a variety of parameters needed to be isolated, and tested. A key factor in EBL is the dosage of the electron beam used to expose the pattern in the resist. Different line dosages were tested in the range of 1.5 μC/cm to 4.0 μC/cm. A line dosage of 1.5 μC/cm was able to achieve a line width of 15 nm, as shown in the inset of Figure 15. Increasing the line dosage up to 4.0 μC/cm caused the line width to increase to 27 nm. The proximity of features was found to greatly affect the results of dosage testing.

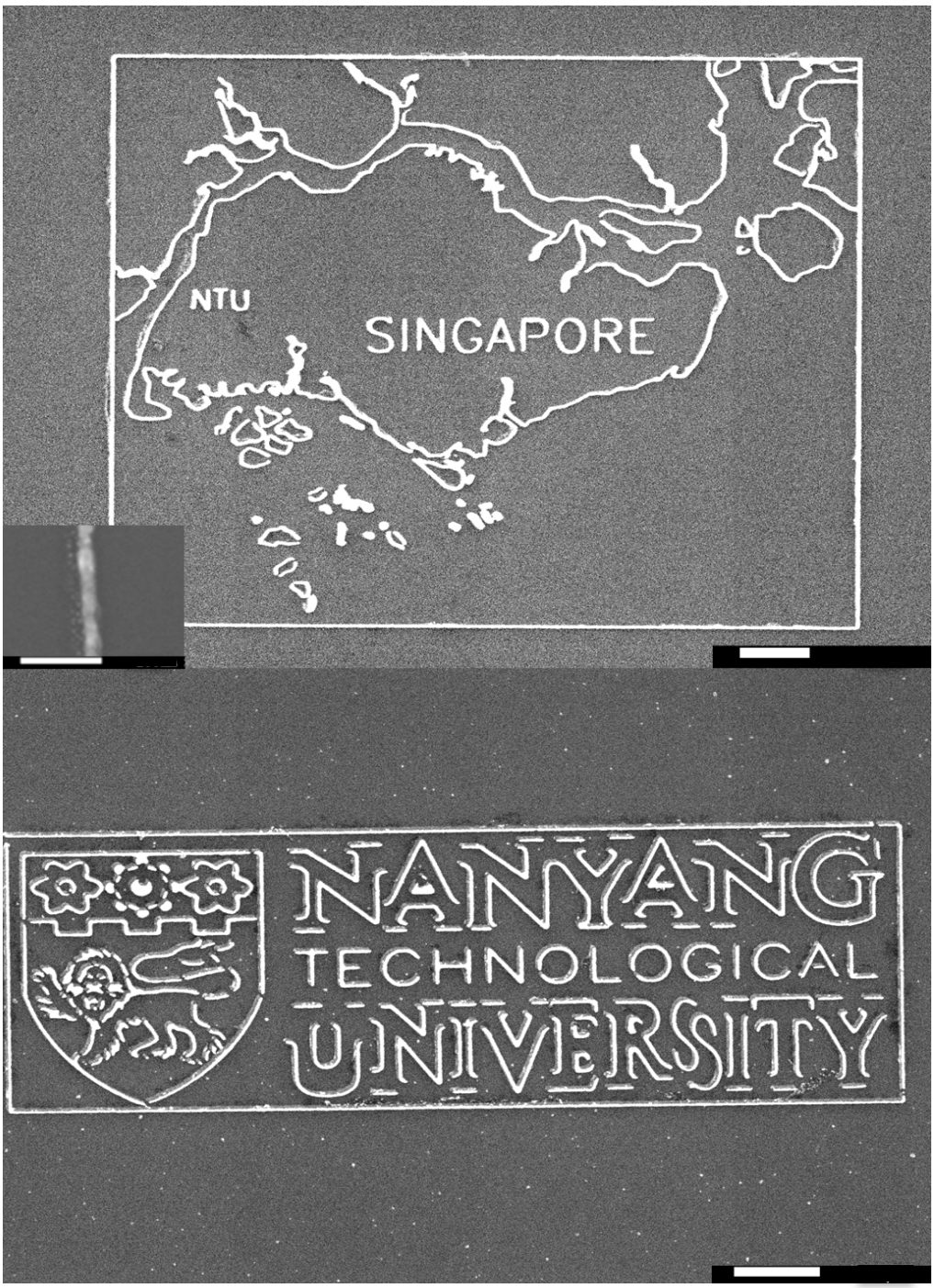

Figure 15: Examples of EBL Fabrication Results Using Line Dosage

Map of Singapore (top). Scale bar is 1 μm. Inset shows smallest linewidth achieved, 15 nm. Scale bar is 100 nm. NTU logo (bottom). Scale bar is 1 μm.

Area dosages were tested from 300 to 900 μC/cm^2. Results varied greatly depending on particle geometry and SEM beam current, demonstrated in Figure 16. It should be noted that for each new nanoparticle system to be fabricated, a dosage testing

should be performed in order to determine the optimal dosage for this particular geometry. In addition, the SEM beam current is constantly changing, which also requires constant dosage tuning.

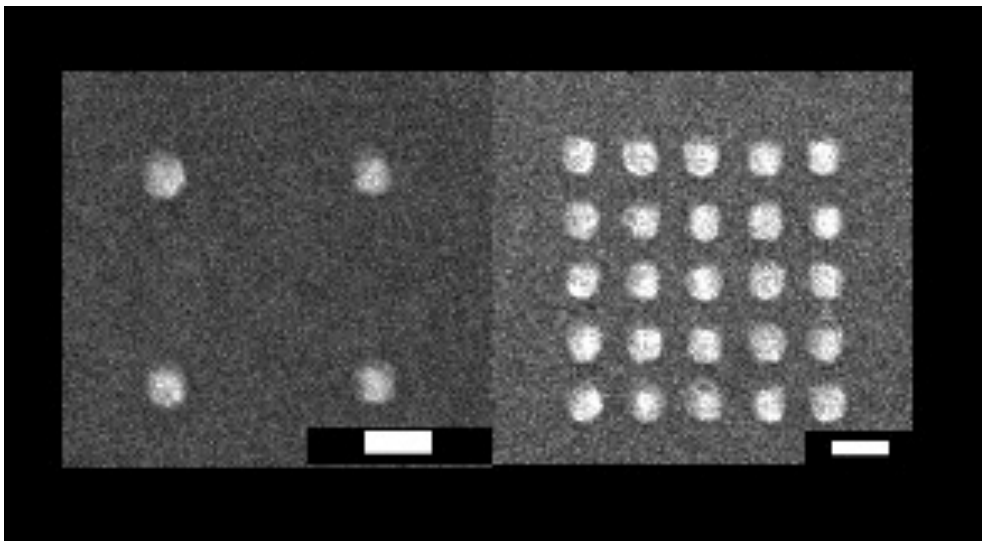

FIGURE 16: DEMONSTATION OF PROXIMITY EFFECTS IN EBL FABRICATION

The effects of pattern proximity on the results of EBL fabrication. For the same dosage the widely spaced (left) and closely packed (right) patterns result in smaller and larger pattern features, respectively. Scale bars are 100 nm.

Bake times of 8, 10, and 15 minutes were tested. A bake time of 15 minutes was found to allow for very small feature patterning. Lower bake times led to softer, more soluble resist that allowed larger features to develop. Higher bake times, such as 15 minutes, led to harder resists that were found to require higher electron beam dosages to fully expose the pattern accurately and smaller features were possible.

Development times from 45 to 90 seconds were tested. A development time of 75 seconds was found to not under- or over-develop patterns. Development times lower than 60 seconds were found to under-develop the patterns and led to features smaller than intended. Development times higher than 75 seconds were found to over-develop the patterns and led to features larger than intended.

Different evaporation rates were tested from 0.3 to 1.3 A/s. An evaporation rate of around 0.8A/s was found to give good surface quality. The thickness monitor was

found to be ineffective for evaporation rates lower than 0.5 A/s. Evaporation rates higher than 0.9 A/s were found to lead to greater surface roughness.

Different liftoff techniques were tested. Liftoff in an acetone bath was tested at room temperature and at 60 °C. Sonication power levels and times were tested. A liftoff involving 3 hours in a room temperature acetone bath followed by 30 seconds of sonication at power level 2 was found to give good liftoff results. Higher sonication powers were found to dislodge the nanoparticles.

3.4 Electron Beam Lithography Recipe

Each parameter was tested in series in order to determine the ideal values for developing a fabrication recipe. Many times the best results meant the smallest or sharpest features.

Bake time of the resist affects how hard the polymer layer becomes and thus how soluble it is to the developer. When the resist is harder the developer works more slowly and one can get smaller, more detailed features to develop. After testing several bake times 15 minutes was found to give the smallest features of all bake times in the test.

The dosage of the electron beam during EBL controls how much charge is allowed to interact with the resist. If an insufficient amount of charge is allowed to contact the resist then the polymer near the bottom will not be exposed. If there is too much exposure then the exposed area will overflow outside of the designed pattern and larger or distorted features will result. The dosage can be tested to determine the most accurate shape and smallest features possible to be written. Many dosages were tested and an area dosage of 450 $\mu C/cm^2$ and a line dosage of 1.5 $\mu C/cm$ were found to give the smallest features, including a linewidth of 15 nm.

Proximity effects can affect the size of features because the electrons will penetrate the area around the pattern feature slightly. If features are close enough the mild Gaussian shaped penetration of the resist overlap to fully expose the resist in areas outside of the pattern. Dosage testing can be done for the periodicity or nearness of the features desired. A 3 nm gap was the smallest gap achieved between triangular prisms.

Development time controls how long the developer solution has in contact with the exposed and unexposed regions of the resist. The developer first dissolves the exposed and more soluble resist areas. The developer also slowly dissolves the unexposed and less soluble areas. An ideal development time would dissolve the exposed areas fully and would minimize the amount of unexposed area dissolved. After testing 4 development times, 75 seconds was found to give the best results.

Evaporation rate can affect the quality of the metal layer deposited. The surface roughness or smoothness is important on such a small scale as the nanoantenna were. A slower evaporation rate leads to a smoother surface. After testing several evaporation rates, 0.5-0.8 A/s was found to give a good quality surface even on nanoscale features.

Proper liftoff technique ensures that the deposited metal is removed fully and cleanly. If not enough liftoff time is allowed then residual polymer resist will remain under the metal and the metal will remain on or near the pattern. Some small pieces of metal may remain on the smaller feature unless a mild sonication is used. Too hard a sonication can result in removal of the small features. Several liftoff techniques were tested and a 2 hour acetone bath at room temperature followed by a 2 min sonication at power level 2 was found to liftoff effectively.

4 CHAPTER 4: NANOROD ARRAYS

1.1 LOCALIZED SURFACE PLASMON RESONANCE SENSING

The dielectric sensitivity of plasmon resonances has been shown to be a robust technique for the detection of analyte binding events *in vitro*.[98-99] Nanoparticle arrays have been shown to have very narrow plasmon resonance peaks, which have great potential for highly sensitive biosensing.[100] With this in mind, the plasmonic and photonic modes of gold nanorod arrays were studied through rigorous experiments and discrete dipole approximations. These sharp resonances were utilized to create very sensitive LSPR-based chemical and biological sensors. Colon cancer markers were successfully and sensitively detected via shifts in the localized surface plasmon resonance (LSPR) of nanorod arrays.

One- and two-dimensional arrays of nanoparticles have been previously studied for their plasmonic resonances and longer wavelength photonic resonances.[30, 101-106] Arrays of gold nanorods showed very sharp resonances that shifted significantly with variations in array parameters. Classical mechanics have been found to be sufficient to describe a system of nanoscale particles in arrays on the order of a wavelength of visible light and DDA is a numerical approximation that has been used to study the classical electrodynamics of such a system.[107-109] Previously, DDA simulations of rectangular nanorod arrays showed the appearance of sharp photonic resonances in the near infrared.[106] These photonic resonances are of great interest to reproduce experimentally for high sensitivity dielectric sensing due to their very narrow resonances.

The periodicity, particle geometry, polarization, and dielectric environment greatly affect the LSPR. Of particular interest, the nanoparticle LSPR has been known to be very sensitive to changes in the dielectric environment of the particle.[2, 34-37] Increases in the refractive index of surrounding dielectric medium are known to red shift the LSPR of nanoparticles. The LSPR shift per refractive index unit is a quantitative way to measure the sensitivity (S) of a plasmonic substrate to its dielectric environment. Another quantification of sensor quality is the figure of merit (FOM), which is the ratio of the sensitivity to the full width at half maximum (FWHM) of a resonance peak.[31] Sharp resonance peaks have narrow FWHMs, which lead to high FOMs. A high FOM is a key factor when designing a highly sensitive chemical and biological sensor. Through computational and experimental studies, nanorod arrays were optimized to have notably

sharp resonances. The high FOM of these substrates is indicative of their great potential in further sensing applications.

Since biomolecules generally have a higher refractive index than their buffer solutions, the binding of biomolecules to the surface of nanoparticles changes the local dielectric environment and can be detected by LSPR shifts. Binding events can be observed using simple transmission spectroscopy. Highly sensitive LSPR biosensing has been done using various plasmonic substrates, including nanorod arrays.[34, 38-41] Nanorod arrays have been used to perform label-free immunoassays observing antibody-antigen and biotin-streptavidin binding through LSPR shift.[99, 110] A sensitivity of 170 nm/RIU with a figure of merit of 1.3 were demonstrated. Several studies have observed the LSPR shift of other binding events, such as Concanavalin-monosaccharide binding, demonstrating the flexibility of LSPR sensors.[111-114]

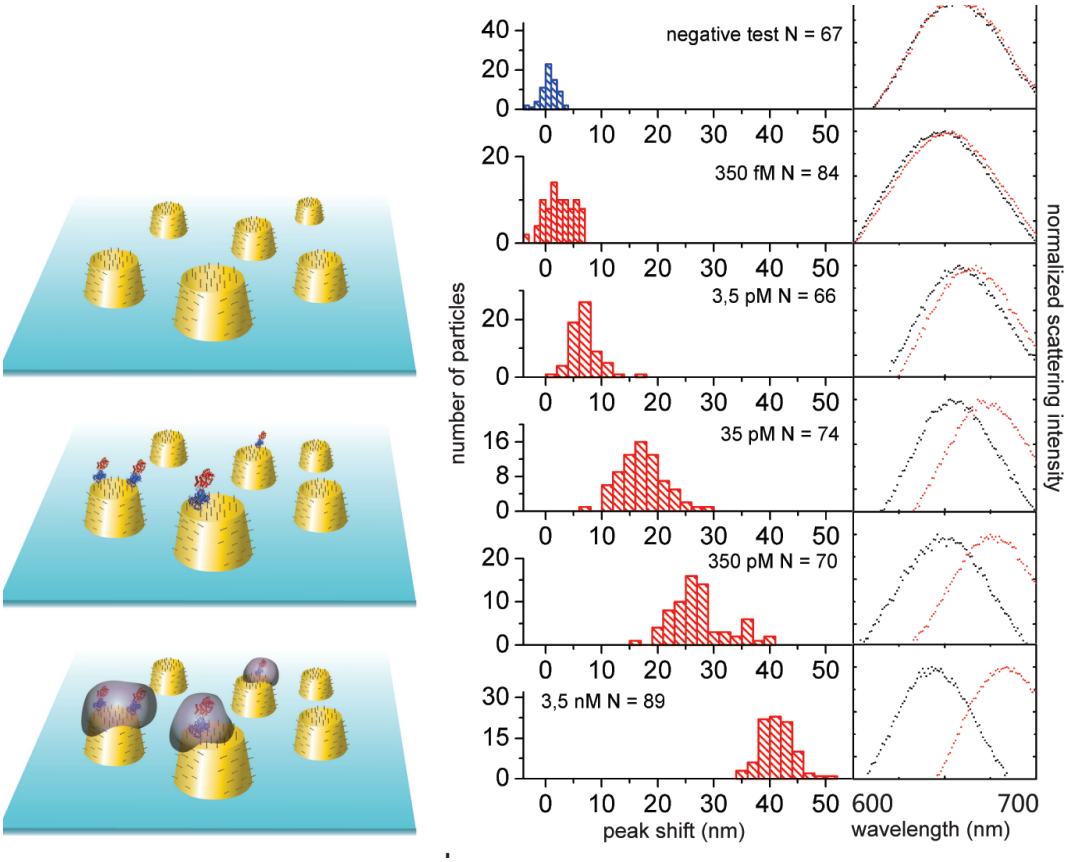

FIGURE 17: LSPR SHIFTS INDUCED BY MOLECULAR BINDING EVENTS

(left) Illustration of molecular binding to gold nanoparticle arrays. (right) Peak shifts $\Delta\lambda_{product}$ induced by HRP induced precipitation on single particles for different concentrations of SA-HRP ranging from 3.5 nm down to 350 fM. The column to the right shows typical single particle raw spectra obtained before (black) and after (red) the enzymatic precipitation reaction. Adapted from Chen et al.[38]

Single nucleotide polymorphisms (SNPs) are mutations in deoxyribonucleic acid (DNA) that usually involve one or more nucleotides being incorrect or out of sequence. SNPs can be found in the wild, and are usually a sign of cancer. One such cancer that is of great concern in the medical community is colon cancer.[115] The SNPs associated with colon cancer, such as the K-*ras* mutation, are well-documented biomarkers for colon cancer, and have great potential to serve in diagnostics.[116-122]

In this chapter, we present a proposal to detect SNPs using LSPR sensing. First, the DNA sample is hybridized to an ideal complimentary strand already covalently bound to the biosensor surface. When a nuclease molecule is introduced to the system and if any SNPs are present, the nuclease cleaves the DNA at that position.[123-124] Surveyor nuclease in particular cleaves both strands at the location of the SNP.[125-126] In theory, the complete removal of a section of DNA bound to the surface of a nanoparticle would lower the local refractive index of the nanoparticle, which would lead to a blue shift in LSPR. We propose that by observing any shift in resonance before and after the nuclease is introduced to the system SNPs could be detected.

Nanorod arrays were studied for their plasmonic and photonic resonances and their potential as LSPR biosensing substrates. One- and two-dimensional arrays were simulated using DDA to observe their extinction efficiency spectra and electric near field. Rigorous periodicity studies were carried out to fully understand the behavior of photonic resonances resulting from the array structure. Two-dimensional arrays of nanorods were fabricated and characterized using transmission spectroscopy. Arrays with very sharp longitudinal resonances were found to act as very sensitive LSPR-based chemical and biological sensors. Chemical sensing capability was tested by measuring the LSPR shift for varying refractive index media. Biosensing capability was tested by observing LSPR shift for biotin-streptavidin binding of varying concentrations of biotinylated DNA. Biosensing was performed via LSPR detection of SNP colon cancer markers.

4.1 Nanorod Array Design, Fabrication, and Testing Parameters

Simulation of the extinction efficiency and electric field was carried out using the DDA method in the DDSCAT program, version 7.0.[69, 74] A grid spacing of 1 nm was used for all simulations. The dielectric constants of Au are taken from Johnson and Christy.[78] We have tested that 1 nm grid spacing is adequate to make the calculation converge. The electric field intensity over the nanoparticle surface was calculated for isolate targets in an

effective medium of refractive index of 1.331. The electric field information was used to make contour plots of the local field intensity on and around the nanoparticle to visualize the features of different modes of excitation. The extinction efficiency was simulated for multiple wavelengths to produce spectra used to determine the resonance position of the particles or arrays.

Electron beam lithography (EBL) was used to fabricate the nanorod arrays. The same polymer layer was used for all chips, 950 poly (methyl methacrylate) (PMMA) A4. The PMMA was spin coated onto the chips using at 4000 rpm for 40 s (Specialty Coating Model P6700) and then baked at 180°C for 15 min. EBL was performed using a JEOL JSM-7001F field emission scanning electron microscope (FESEM) equipped with a Deben Beam Blanker and a nanometer pattern generation system (NPGS). After e-beam writing, the chips were developed for 75s in a solution of 1:3 methyl isobutyl ketone (MIBK):isopropyl alcohol (IPA) at room temperature. After development the chips were rinsed for 20s in IPA and blown dry using nitrogen gas. Evaporation of 2 nm Cr and 30 nm Au was sequentially done in a thermal evaporator (Elite Engineering, Singapore). A chamber pressure of $2x10^{-7}$ Torr and evaporation rate of approximately 0.6 Å/s were used for evaporation. Liftoff was done at room temperature in acetone for 2 hours followed by a 2 minute sonication (Crest Ultrasonics Powersonic P1100D) at low power (level 2). More details about the fabrication process and recipe development can be found in Appendix B. Nanorod geometry was observed and measured by SEM. Figure 1 shows an example of SEM image, with an inset showing the variable usage used throughout the work.

Transmission spectroscopy was performed on a 20/20 PV™ UV-Visible-NIR microphotospectrometer (CRAIC Technologies™, USA) with non-polarized light in air, unless otherwise noted, with an angle of incidence of 90 degrees and an aperture size of 15 μm. Spectra were taken for at least three locations per sample.

For the dielectric sensitivity testing Au nanorods chip was first cleaned by sonication in IPA for one minute, washed in deionized water and dried by nitrogen gas. Then, glycerol solutions (Alfa Aesar, UK) of 1%, 10%, 20%, 28%, 36%, 44%, 52%, 64%, 72%, 84%, 92%, and 100% in DI water, corresponding to different refractive indices (RI) of 1.3342, 1.3448, 1.3572, 1.3676, 1.33897, 1.4011, 1.4189, 1.4310, 1.4492, 1.4613, and 1.4735 respectively, were deposited and covered by a cover slip.[127] After each measurement, the chip and cover slip were rinsed by DI water and blown dry using

nitrogen gas. LSPR λ_{max} shifts were plotted against their respective RI unit, and sensitivity of Au nanorods was calculated by linear regression.

For DNA sensing experiments, the chip was washed by IPA, rinsed by DI water, and then cleaned by ultraviolet-ozone process (UV-1, SAMCO, Japan) for 15 min. Immediately after cleaning, the chip was incubated in 1 mM solution of 1:9 (v/v) mixture of biotin-PEG3-thiol (spacer arm length 27-28 Å, nanoScience Instruments, USA) and methyl-PEG4-thiol (spacer arm length 15.8 Å, Pierce, USA) in DMSO for 2 hr. The chip was washed in DI water for 5 min and blown dry using nitrogen gas. The chip was incubated in a streptavidin (Pierce, USA) solution of 250 nM for 1 hr, washed in PBS (pH 7.4) for 5 min, rinsed in DI water, and dried using N2. To apply as minimum as possible amount of DNA solution, the nanorod array was bound by a hydrophobic tape. The nanorod array was then incubated in 100 µL of biotinylated DNA (MW 9440 Da, 1st BASE, Singapore) of 10^{11}, 10^{8}, 10^{5}, 10^{2}, and 10^{-1} aM concentrations in PBS for 1 hr. Then the chip was washed in PBS for 5 min, rinsed with DI water, and dried by N2.

For the SNP experiments 100 µM thiolated DNA probe (Integrated DNA Technologies, Singapore) was first mixed with 150 mM dithiothreitol (Sigma-Aldrich, Singapore) at room temperature for 2 hr to deprotect the terminal thiol group. After the deprotection, the thiolated DNA probe was desalted and purified using a NAP-5 column (GE Healthcare, Singapore). An open chamber was made by punching a hole (d ~ 8 mm) on an adhesive tape using a paper puncher and sticking it onto the ITO glass substrate where the AuNRs are aligned in the center of the hole. Then, 20 µL of 20 µM deprotected DNA probe diluted in PBS buffer (100 mM, pH 7) was dropped into the open chamber and incubated at room temperature overnight. A glass coverslip (thickness no. 1) was placed on the top of the chamber to avoid evaporation. After the incubation, wash the chip with PBS buffer and air-dry.

WT and MT DNA at various concentrations and ratios were hybridized with the DNA probes immobilized on the AuNRs' surface. Briefly, 10 µL of each DNA sample was mixed with 10 µL PerfectHyb™ Plus Hybridization Buffer (Sigma-Aldrich, Singapore). After that, the mixture was added onto the DNA-functionalized AuNRs. Then, the reaction was first incubated at 90 °C for 5 min, and then at 42 °C. During the incubation, a high humidity condition should be kept to avoid evaporation. After the incubation, the AuNRs was washed by DNA-free H_2O.

TABLE 1: DNA SEQUENCES FOR SNP DETECTION EXPERIMENT

Name	Sequences (5'-3')	Tm (°C)
Thiolated DNA probe	Dithiol-TTT TTT TTT TAG CTC GTG GCG TAG GC	58.5
Mutant type (MT)	GCC TAC GCC ACC AGC TAA AAA AAA AA	58.7
Wild type (WT)	GCC TAC GCC ACG AGC TAA AAA AAA AA	58.5

After hybridizing with the immobilized DNA probe, the samples were treated with Surveyor Nuclease (Transgenomic Inc., UK) according to the manufacturer's protocol. After that the chip was washed by DNA-free H_2O and measured using transmission spectrophotometer.

4.2 RESULTS

Two dimensional nanorod arrays were fabricated by EBL in a variety of array geometries. Figure 18 shows an SEM image of nanorods with 200 × 50 nm geometry in a square array with a 500 × 500 nm center-to-center periodicity. Other square and rectangular arrays were fabricated with varying periodicities from 100 nm to 1 μm.

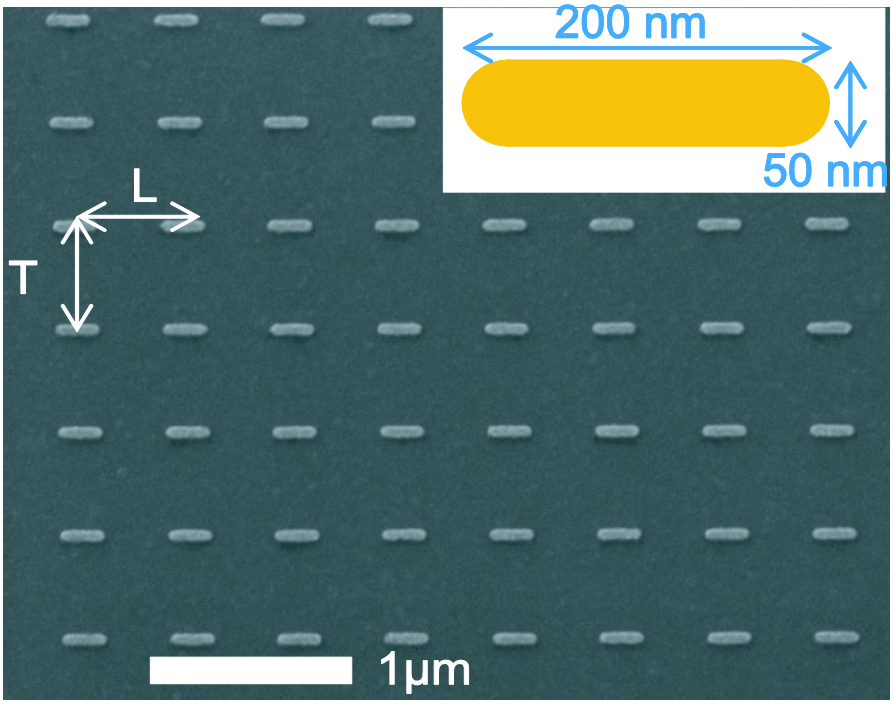

FIGURE 18: SEM IMAGE OF NANOROD ARRAY

Scanning electron microscopy image of nanorod array. "L" denotes the longitudinal array parameter. "T" denotes the transverse array parameter. Inset shows the nanorod geometry. Nanorods are nominally 200 nm long and 50 nm wide.

4.2.1 Simulated Effect of Geometry on Single Nanorods

In order to understand the effects of changes in nanorod size and aspect ratio, the DDA was used to simulate the extinction efficiency spectra of varying nanorod geometries. This is an important factor to consider, as small variations in the fabrication procedure can drastically affect the experimental particle shape. It is essential to understand the effect of nanorod geometry on LSPR. Figure 19a shows the variation in resonance of a single nanorod with constant length and varying width. Spectra for both polarizations are shown, longitudinal (parallel to the nanorod axis) and transverse (perpendicular to the nanorod axis), as illustrated in Figure 18. Figure 19b shows the extinction spectra of a single nanorod with a constant width and varying length. There is very little variation in transverse resonance position for either variation in aspect ratio, though there is a slight red shift for an increase in nanorod thickness. The variation of aspect ratio, the length over the width of the particle, has a huge effect on the longitudinal resonance mode. Aspect ratios 2.7 to 8 vary the resonance from 900 to 1400 nm. As the

aspect ratio of the rod decreases, it becomes more sphere-like, in geometry and resonance. It is useful to understand this phenomenon when considering the experimental results from fabricated nanorods. When slight variations in nanorod geometry cause significant changes in resonance position, the specific shape of each batch of rods must be measured and considered when analyzing the trends of other parameters. In the case of trends with unexpected result, the geometry of the nanorods can be analyzed and the LSPR can be normalized for particle geometry.

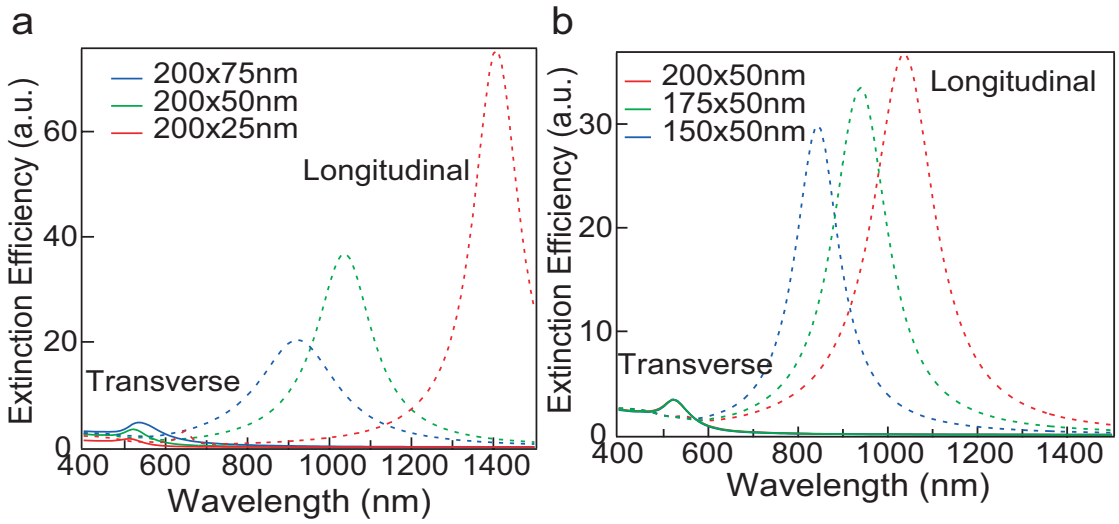

FIGURE 19: SIMULATED EXTINCTION SPECTRA OF SINGLE NANORODS

Simulated extinction efficiency of single nanorods with varying a) widths and b) lengths. Longitudinal (dashed lines) and transverse (solid lines) polarizations shown.

To better understand the two modes, the electric near-field was visualized through simulation. Figure 20a and b show the electric near-field contour plots of a single nanorod with longitudinal and transverse polarizations, respectively. The longitudinal mode has hotspots located at the ends of the nanorod. The transverse mode has a more uniform electric near-field with cold spots at both ends of the nanorod. The weak electric field excited in the transverse mode will have weak interactions when particles are arranged in arrays. Changes in transverse periodicity may not make much impact on LSPR. The strong, localized electric field excited in the longitudinal mode, however, will interact strongly and changes in longitudinal periodicity will greatly affect the LSPR.

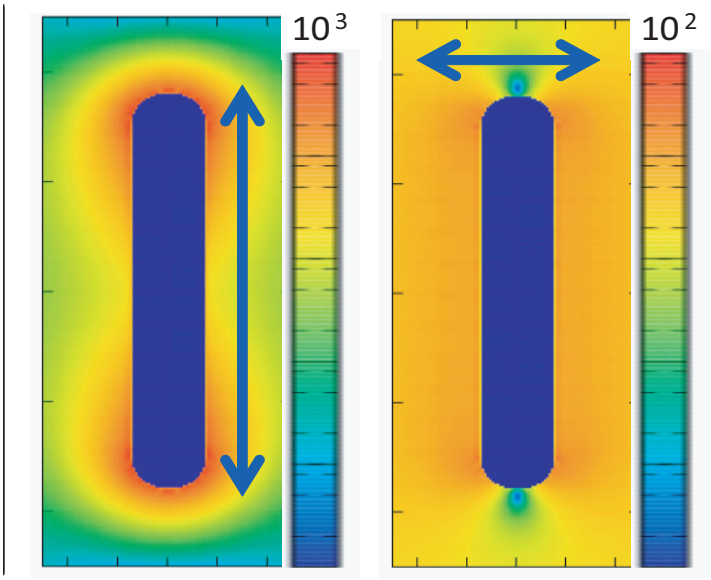

FIGURE 20: SIMULATED ELECTRIC FIELD OF SINGLE NANORODS

Simulated electric near-field, $|E|^4$, for single nanorods with longitudinal (left) and transverse (right) polarization.

4.2.2 Simulated Effect of Periodicity on One-Dimensional Arrays

In order to understand how periodicity affects the LSPR, it is necessary to first understand the effects of the two basic types of one-dimensional arrays. Figure 21 shows the simulated extinction efficiency spectra for a single nanorod and one-dimensional arrays, for transverse and longitudinal polarizations. Very large period arrays have similar LSPR to a single nanorod, since the particles are far enough apart that coupling is negligible. However, as the period is decreased, and the near field of the particles can interact, the resonance shifts and new features appear. The transverse mode was not greatly affected by changes in transverse periodicity, as shown in Figure 21a. The longitudinal mode of transverse periodicity arrays, shown in Figure 21b, was greatly affected by the variation of the periodicity. The resonance shifts, but with no clear trend, and new features appear for some periods, both of which warranted further studies, shown in Figure 22. The transverse mode of nanorods does not interact in longitudinal arrays, therefore variation of periodicity in longitudinal arrays did not affect the transverse mode LSPR, as shown in Figure 21c. The longitudinal mode of nanorods interacts strongly in longitudinal arrays and the longitudinal LSPR was greatly affected by changes in longitudinal periodicity, as shown in Figure 21d, blue shifting as the particles draw closer.

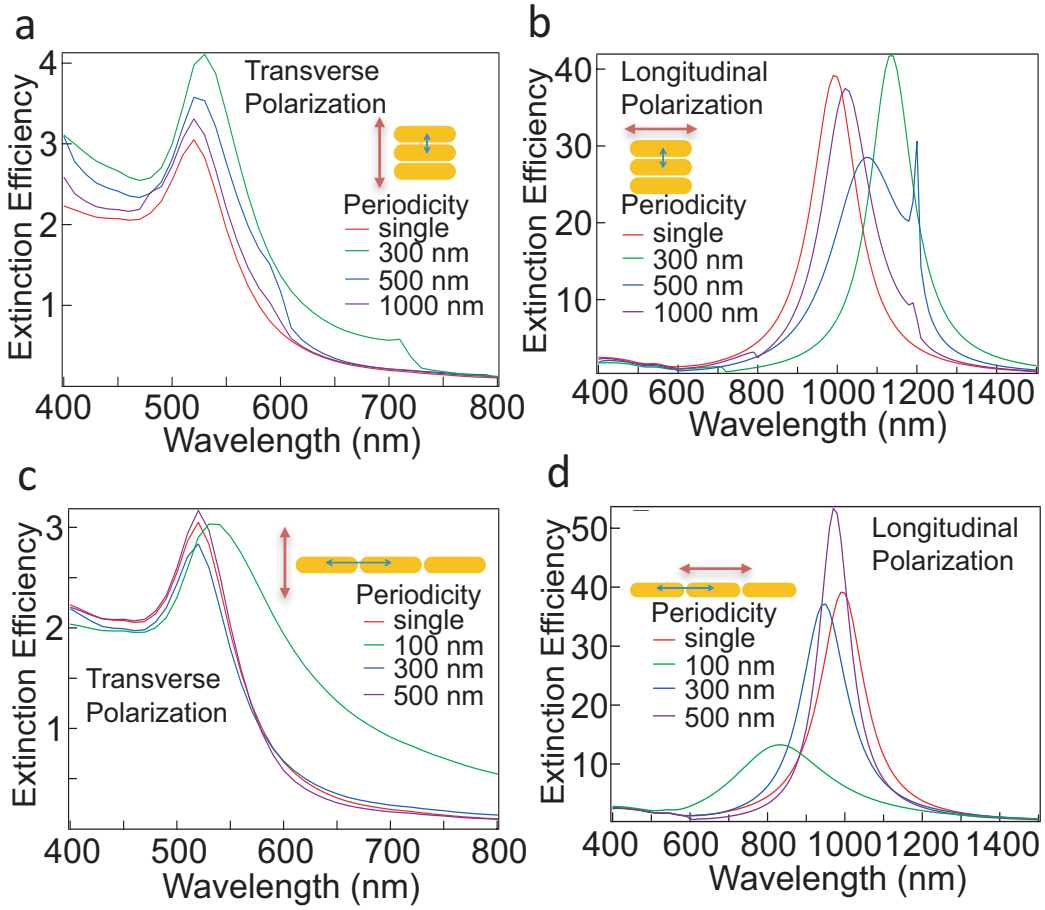

FIGURE 21: SIMULATED EXTINCTION EFFICIENCY OF ONE-DIMENSIONAL ARRAYS OF NANORODS

Simulated extinction efficiency spectra for one dimensional arrays of nanorods with: a) transverse array with a transverse polarization; b) transverse array with a longitudinal polarization; c) longitudinal array with a transverse polarization; d) longitudinal array with a longitudinal polarization.

The appearance of a new peak around 1200 nm in the longitudinal polarization warranted further studies, and Figure 22 shows the extinction efficiency of a thorough study of the effect of periodicity in one-dimensional transverse arrays with longitudinal polarization. The appearance and subsequent red shift of two peaks is observed. These peaks appear very narrow and red shift and broaden until at their maximum extinction at approximately 830 and 415 nm periods. These values correspond roughly to the LSPR wavelength divided by the refractive index of the surrounding medium, 1.331 (divided by two for the 415 nm period).

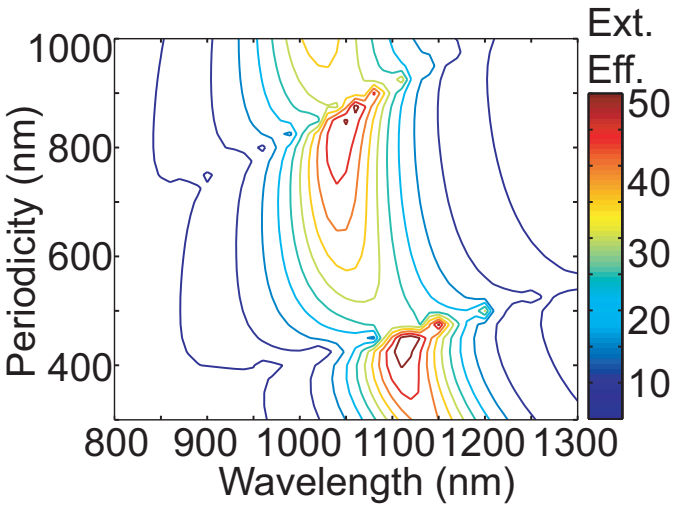

FIGURE 22: SIMULATED EXTINCTION EFFICIENCY OF ONE-DIMENSIONAL ARRAYS OF NANORODS WITH TRANSVERSE PERIODICITY AND LONGITUDINAL POLARIZATION

Further calculations of the transverse array with longitudinal polarization to follow the development of the peak formation.

In order to predict the SERS performance of nanorod arrays, the electric field can be simulated and studied for trends and patterns. The electric field intensity was shown to be much higher for longitudinal polarization in Figure 20, which makes it of interest for potential future SERS experiments (which would be conducted at 785 nm excitation due to availability of lasers). Therefore the electric field intensities of various one-dimensional arrays of nanorods were simulated under longitudinal polarization at 785 nm excitation. The blue shift of the longitudinal mode in Figure 21d is concurrent with the theory that the electric near field of the longitudinal mode would be affected by changes in longitudinal periodicity. The electric field is increasing in energy as the particles draw closer and the near field features have more interaction. Also, the red shift in Figure 21b implies that the electric field intensity of the longitudinal mode will decrease with decreasing transverse periodicity. Figure 23 shows the simulated maximum electric field intensity for a single nanorod and a variety of one-dimensional arrays with longitudinal polarization. Large period arrays of both types more closely resemble the single nanorod, as expected from the similar trends with the resonances. As the longitudinal period is decreased, the electric field increases. As the transverse periodicity is decreased, the electric field intensity decreases. This result agrees with the patterns observed in the resonance shifts of both types of arrays, since the excitation wavelength is 785 nm.

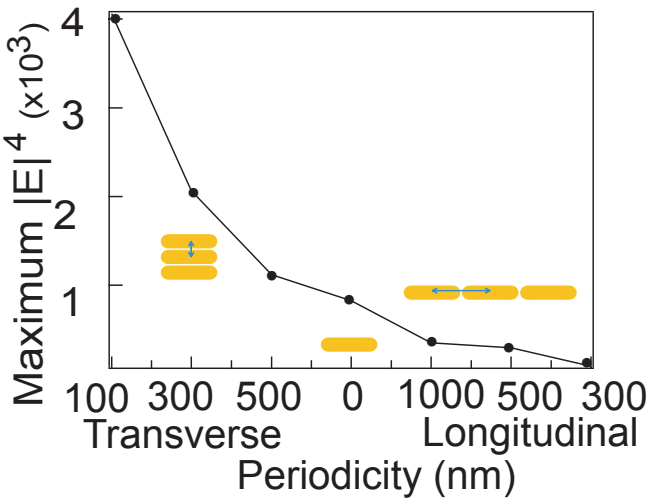

FIGURE 23: SIMULATED ELECTRIC FIELD OF ONE-DIMENSIONAL NANOROD ARRAYS

Maximum electric field intensity for varying transverse and longitudinal one dimensional arrays as compared to a single nanorod, all with longitudinal polarization and 785 nm excitation.

4.2.3 Simulated Effect of Periodicity on Two-Dimensional Arrays

After understanding the trends developed when nanorods are introduced into one-dimensional arrays, it is necessary to expand the system to two-dimensional arrays. The trends observed in one-dimensional array simulations can be used to understand phenomena and trends observed in two-dimensional simulations. Simulated spectra of two-dimensional arrays are of interest to compare with, and better understand and optimize, potential experimental conditions. The sharp resonance occurring under the longitudinal polarization will be the mode of interest for use in experimental biosensing. Figure 24 shows the simulated extinction efficiency spectra of a variety of two-dimensional arrays with longitudinal polarization. Figure 24a shows the extinction spectra of arrays with varying transverse periodicity and constant longitudinal periodicity. The plasmonic mode, around 1000 nm, remains stationary with increasing transverse periodicity. There is a second peak, around 1250 nm, which also remains stationary but undergoes sharpening with increased transverse periodicity. This peak is well correlated to the photonic resonance found in the one-dimensional array simulations. Figure 24b shows the extinction spectra of arrays with varying longitudinal periodicity and constant transverse periodicity. The increase in longitudinal array periodicity causes a blue shift in the plasmonic mode. The appearance and sharpening of the photonic resonance is more dramatic in the variation of the longitudinal periodicity.

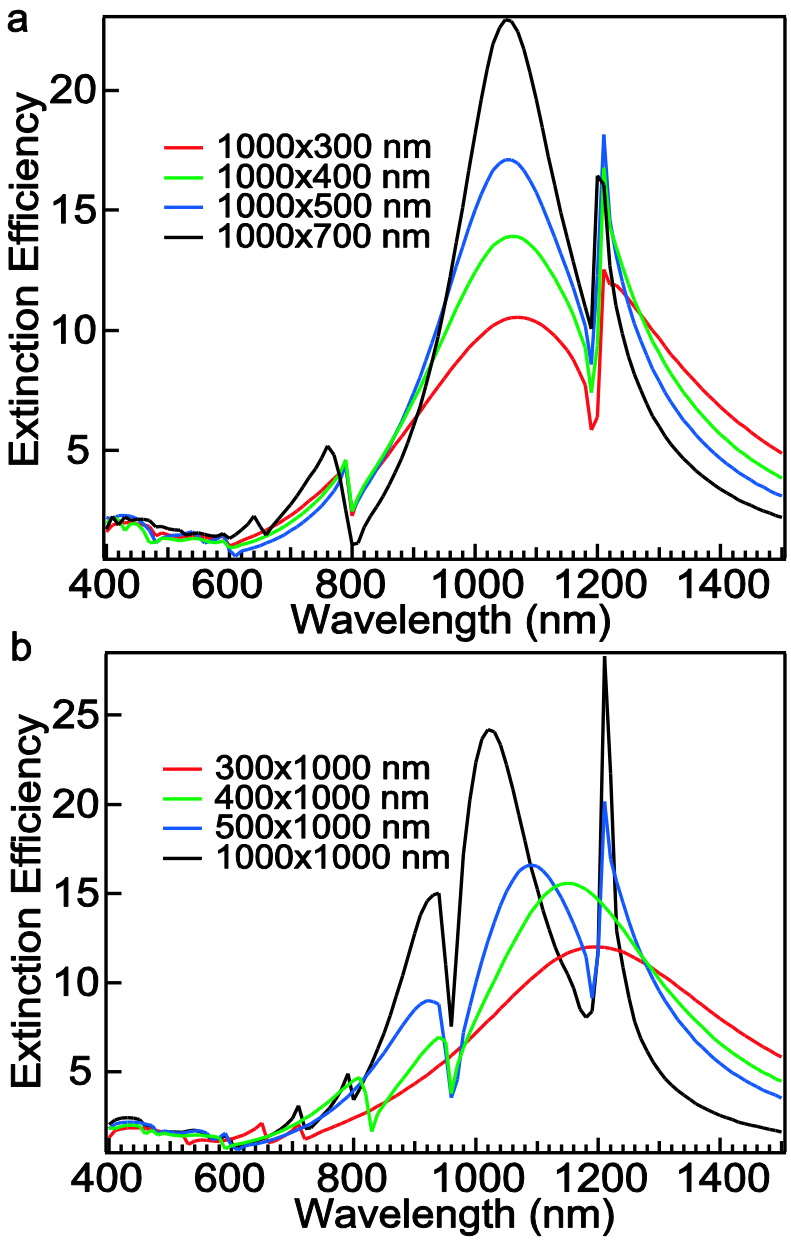

FIGURE 24: SIMULATED EXTINCTION SPECTRA OF NANOROD ARRAYS

Simulated extinction efficiency spectra of two dimensional nanorod arrays with longitudinal polarization. a)Arrays with constant longitudinal periodicity and varying transverse periodicity. b) Arrays with constant transverse periodicity and varying longitudinal periodicity.

4.2.4 EXPERIMENTAL EFFECTS OF PERIODICITY ON TWO-DIMENSIONAL ARRAYS

The sharp photonic resonances seen in simulation have great potential for biosensing, due to the narrow FWHM and high FOM, and so it was of great interest to recreate such resonances experimentally. This requires very high quality fabrication, in order to minimize the surface roughness effects and maintain consistent nanorod shape. Nanorods with 200 nm length and 50 nm width were fabricated in rectangular arrays with periodicities varying from 100 nm to 1μm. Figure 25 shows the experimental transmission spectra of two-dimensional arrays with varying transverse and longitudinal periodicity. Simulation predicted that increasing the transverse periodicity would not shift the longitudinal resonance of a two-dimensional array. In the experimental transmission spectra the longitudinal mode of the 1000 × 100 nm array is red shifted from the resonance position of the other two arrays, and the transverse mode is blue shifted. According to the study on nanorod geometry, shown in Figure 19, this implies that the nanorods in the 1000 × 100 nm array are slightly wider than the nanorods in the other two arrays. Increasing the longitudinal periodicity blue shifts the longitudinal mode of the transmission spectra, as predicted by simulation. Increasing the transverse periodicity also blue shifts the longitudinal mode of the transmission spectra, as predicted from the simulations.

The appearance of the sharp photonic resonance in the near-infrared region of the spectrum did not occur as expected from simulated results. This is assumed to be due to the dielectric mismatch of the experimental system. The simulated environment is a constant dielectric medium with refractive index 1.331, whereas the experimental system consists of an indium-tin oxide (ITO) coated glass substrate and air. A dielectric medium with refractive index 1.331 was determined to be the closest approximation to the experimental system, as the resonances match at these conditions.

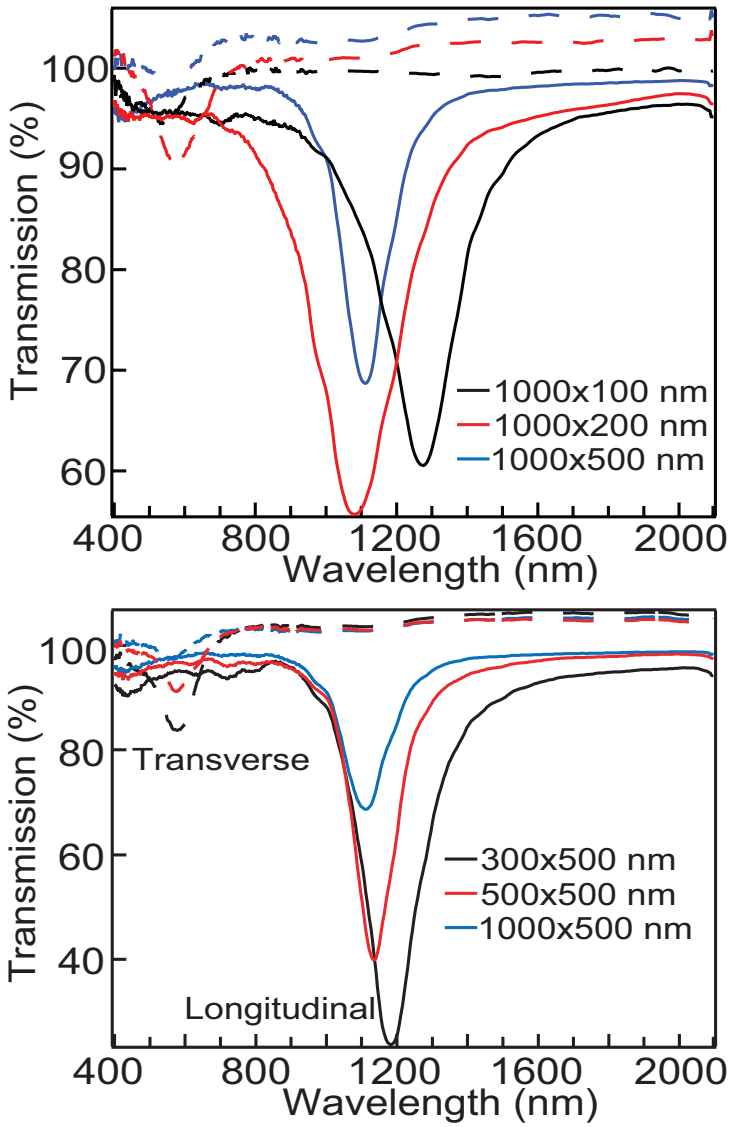

FIGURE 25: EXPERIMENTAL TRANSMISSION SPECTRA OF NANOROD ARRAYS

Experimental transmission spectra for two dimensional nanorod arrays with varying transverse (top) and longitudinal (bottom) periodicity.

4.2.5 CHEMICAL SENSING BASED ON LSPR OF NANOROD ARRAYS

The existence of such a sharp plasmonic resonance as appears in the 300 × 500 nm and 500x500 nm arrays is instantly recognizable as a potential LSPR biosensor as its narrow FWHM, approximately 100 nm, would result in a high FOM, meaning that very small shifts in the resonance easily distinguishable. To determine the sensitivity and FOM of this nanorod array, mediums of different refractive indices were applied and the

resonance red shifts were measured. Figure 26 shows, in black, the experimental sensitivity, 309.6 nm/RIU, of the longitudinal mode of a 300 × 500 nm array in a variety of concentrations of glycerol. The FOM was calculated to be 3.60. Figure 26 also shows, in blue, the simulated sensitivity, 679.3 nm/RIU, of an isolated nanorod to changes in a homogenous dielectric environment. Both calculations of the response of the system to changes in refractive index show a very good linear fit with a coefficient of determination very close to one. The discrepancy in sensitivity is due to the difference in nanoparticle surface area exposed to changes in dielectric material resulting from simulating a homogenous dielectric environment and the experimental conditions of a nanoparticle on an ITO/glass substrate coated with dielectric material. When considering that, using the effective medium theory, an ITO/glass substrate can be approximated in DDSCAT by a RI of 1.331, one could recalculate the simulated sensitivity, with adjusted RIs to take the substrate into account. The simulated environment of a nanoparticle in a homogenous dielectric medium of refractive index 1.331 is equivalent to a particle on an ITO substrate in air. The simulated environment of a nanoparticle in a homogenous dielectric medium of refractive index 1.5 is equivalent to a particle on an ITO substrate in a medium of RI 1.34. Using these equivalencies, a 126.6 nm shift for a change of medium RI of 0.34 RIU, the simulated sensitivity is 372.4.This value is much more akin to the experimental value. Even without this consideration, the experimental sensitivity and FOM are very high and indicate that this nanorod array will prove to be an effective and sensitive biosensor.

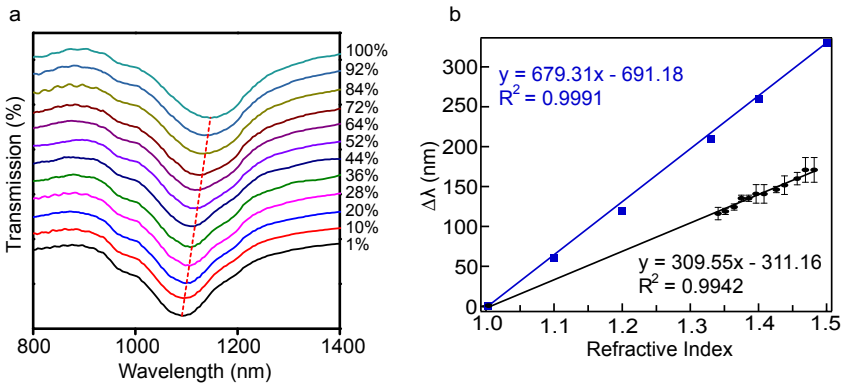

FIGURE 26: LSPR- BASED CHEMICAL SENSING

a) Transmission spectra of varying concentrations of glycerol on a nanorod array on ITO/glass substrate with 300 nm longitudinal periodicity and 500 nm transverse periodicity. b) Dielectric sensitivity. Black data and equation denote the experimental study of nanorod array coated with dielectric medium. Blue data and equation denotes the DDA simulation of a single nanorod in

homogenous dielectric.

4.2.6 BIOSENSING BASED ON LSPR OF NANOROD ARRAYS

In order to evaluate the sensitivity of the nanorod arrays as a potential biosensing platform, the shift caused by molecular binding events must be evaluated. The nanorod array with the highest FOM was chosen, 300 × 500 nm period, as it has the most potential as a biosensor. Nanorod arrays were incubated sequentially with thiolated biotin, streptavidin, and biotinylated DNA and the LSPR shift was measured for each binding event. Figure 27 shows the spectra and λ_{max} shifts for different concentrations of biotinylated DNA, down to 0.1 aM. This concentration of DNA corresponds to approximately 3 molecules in 50 µL of buffer solution. This is a very low limit of detection through streptavidin-biotin binding, and proves the potential of this plasmonic substrate as a biosensing platform.

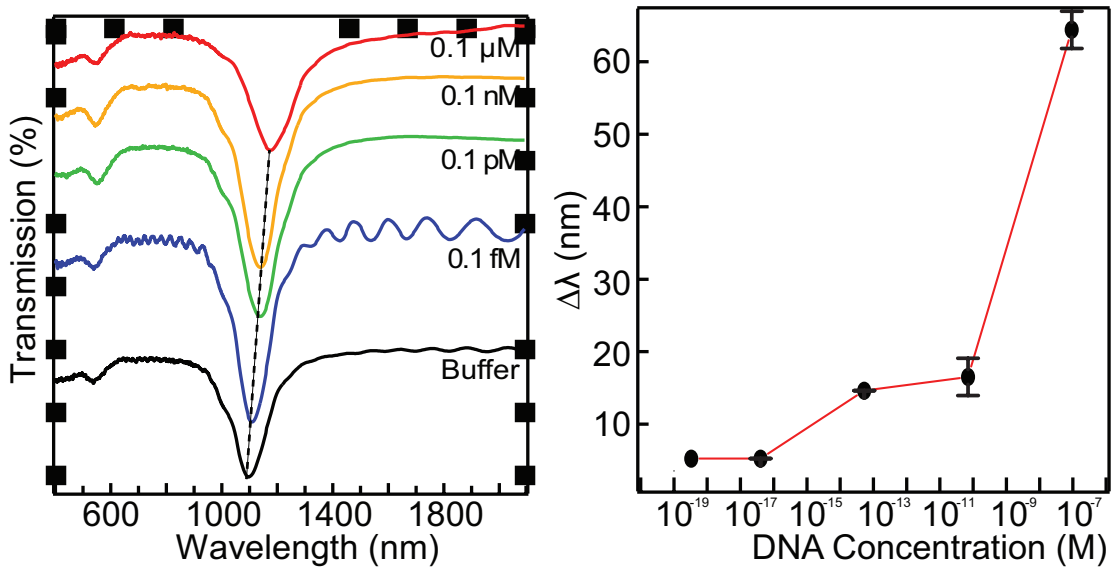

FIGURE 27: SENSITIVITY OF LSPR- BASED BIOSENSING OF SSDNA

Spectra (left) and LSPR λ_{max} shifts (right) of a 300 × 500 nm nanorod array with varying concentrations of DNA. LSPR λ_{max} shifts are plotted in log scale.

The detection of colon cancer was done using the enzymatic cleavage of SNPs. SNPs occur in cancerous cells and in vitro testing can be done to detect SNPs and diagnose colon cancer. The Surveyor nuclease enzyme cleaves both strands of hybridized

DNA at the location of an SNP. When hybridized DNA with SNPs is cleaved the local refractive index of the nanorods is reduced and results in a blue shift of the LSPR of the nanorods. By observing the LSPR shift before and after enzymatic cleavage, the amount on SNPs present in the DNA sample can be deduced. The process of attaching probe DNA, hybridization with sample DNA, and nuclease cleavage is illustrated in Figure 28.

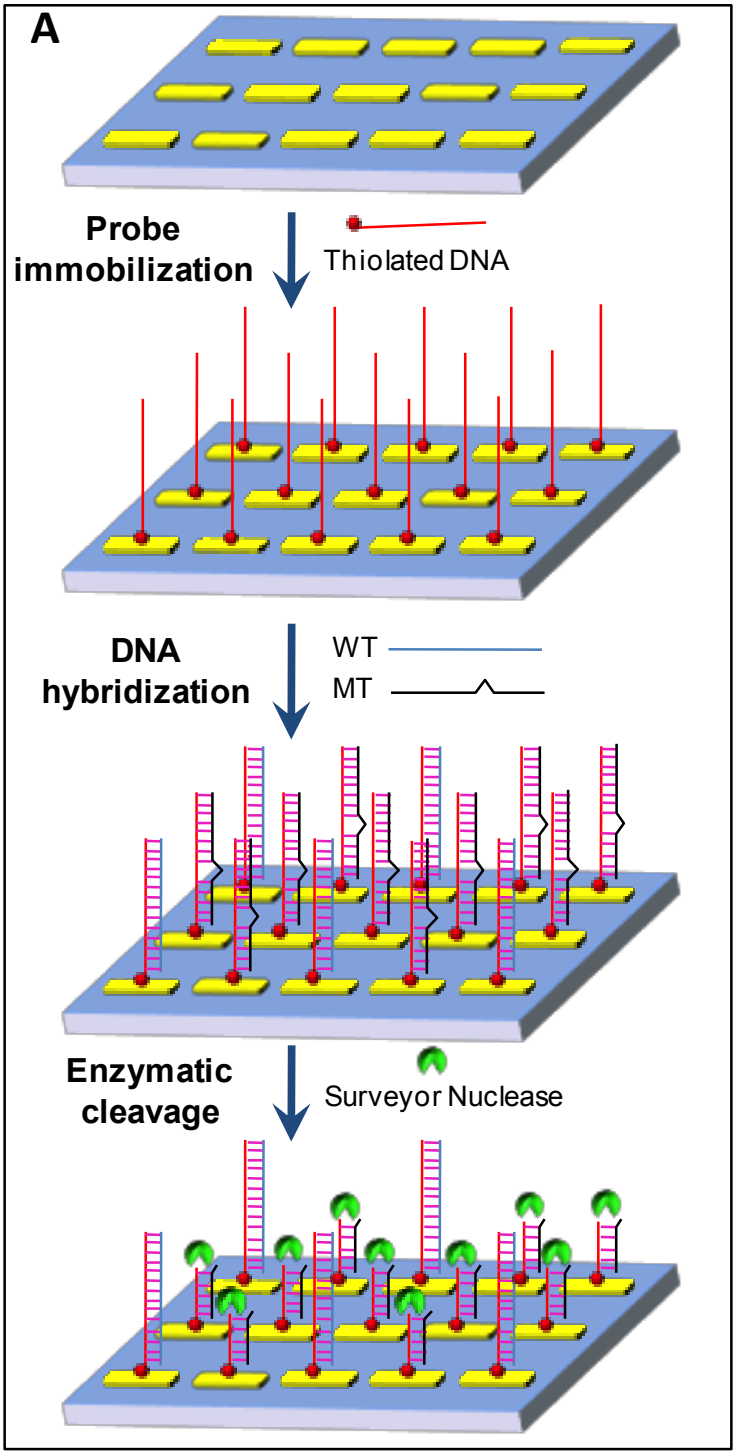

Figure 28: Schematic of Single Nucleotide Polymorphism Cleavage

Schematic illustrating bare gold nanorods, the addition of probe DNA, the hybridization with DNA with SNPs, and cleavage at the SNP site using Surveyor nuclease.

The addition of probe DNA to the nanorod surface increases the local refractive index of the nanorods resulting in a redshift of the LSPR. The hybridization with perfectly matched, wild type (WT) DNA also increases the local refractive index. The LSPR shifts related to the addition of probe DNA and varying concentrations of WT DNA hybridization are shown in Figure 29.

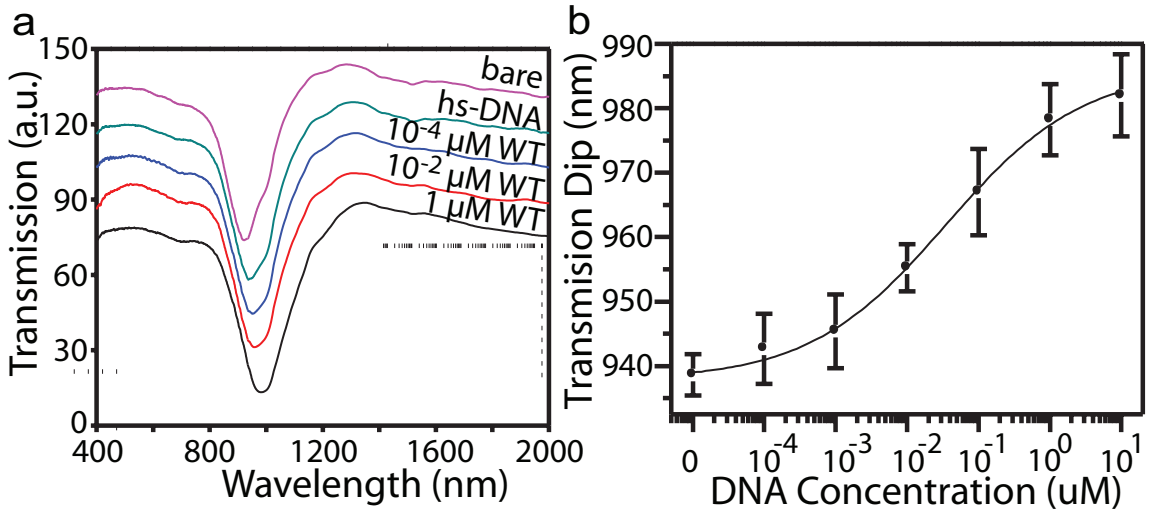

Figure 29: Sensitivity of LSPR-Based Biosensing of DNA Hybridization

a) Transmission of bare gold nanorods, thiolated DNA, 10^{-4} uM perfectly matched DNA (Wild Type (WT)), 10^{-2} uM WT, 1 uM WT. b) Transmission dip of hybridization with WT.

When the hybridized DNA has a SNP present, there is a mismatched nucleotide pair and the mutant type (MT) DNA will not hybridize to the probe DNA at the location of the SNP. When Surveyor nuclease is introduced to the system, it will cleave both strands of DNA at the location of the SNP, as shown in Figure 30a. This cleavage reduces the local refractive index of the nanorods, resulting in a blue shift of the LSPR. If there are no SNPs present in the sample DNA, then there should be no enzymatic cleavage and no blue shift in LSPR. The proof of concept of SNP detection is shown in Figure 30.

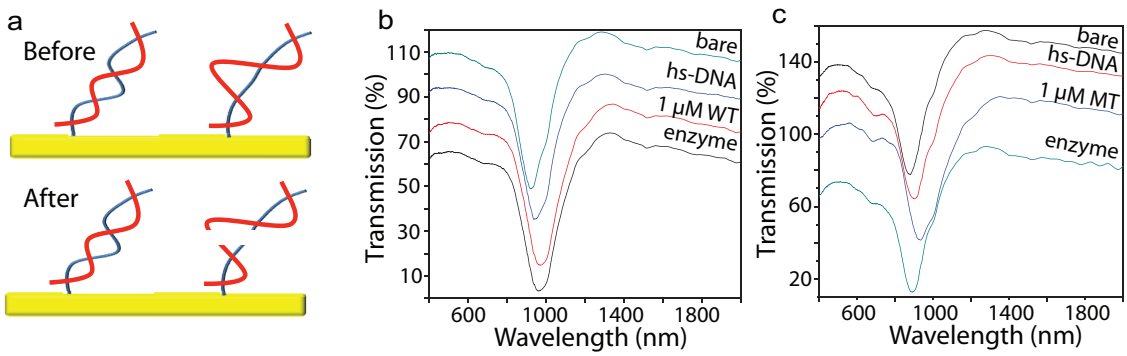

Figure 30: Proof of Concept for SNP Detection

a) Illustration of Surveyor nuclease enzyme cleavage for detection of perfectly matched DNA (Wild Type (WT)) and single mismatched DNA (Mutant Type (MT)) Transmission shifts for bare gold nanorods, thiolated DNA, hybridized with 1 μM WT (b) or MT (c), enzyme cleavage.

In order to perform early, sensitive cancer diagnostics a biosensor must be able to detect very low concentrations of biomarker. In the early stages of cancer there will only be a small number of mutant DNA present within mostly normal healthy samples. In order to better show the potential of these nanorod arrays as a useful biosensor, varying ratios of mutant and healthy DNA were hybridized to the probe and exposed to Surveyor nuclease. In this way, varying percentages of the total DNA adsorbed onto the gold nanorods will be cleaved and the LSPR shift should reflect this percentage. Figure 31 shows the LSPR shift after nuclease cleavage for varying ratios of MT to WT DNA. The nanorod biosensor was able to detect 1 nM MT per 1000 nM WT DNA.

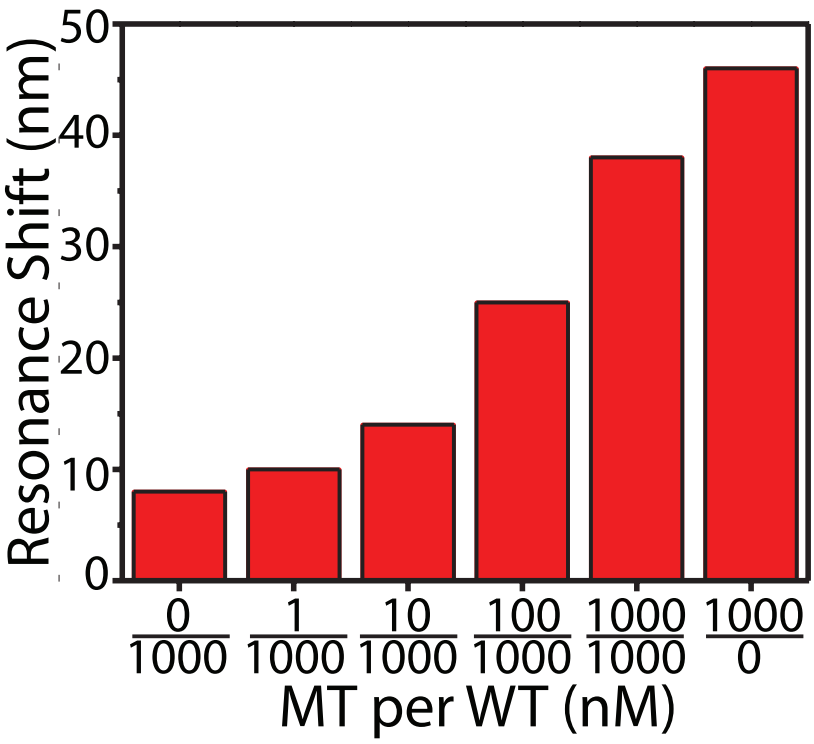

Figure 31: Limit of Detection of SNP

Surveyor nuclease enzyme cleavage for detection of single mismatched DNA (Mutant Type (MT)).

4.3 CONCLUSIONS

In order to design an LSPR-based biosensing substrate, it was necessary to characterize the effects of nanorod geometry and array parameters. Increasing the aspect ratio of nanorods leads to red shifting and sharpening of resonances. Simulations of two-dimensional arrays, confirmed experimentally, have shown that increasing the longitudinal or transverse period blue shifts the longitudinal plasmonic resonance. No experimental evidence was found for the appearance of the sharp photonic resonance shown in simulations.

Lithographically fabricated nanorod arrays with very sharp plasmonic resonances, with quality factors of around 12, have proven to be highly sensitive chemical and biological sensors. When measuring the response to the refractive index of dielectric media, a figure of merit of 3.6 and a sensitivity of 309.55 nm/RIU were achieved. DNA molecules were detected down to 0.1 aM (~3 molecules in 50 μL). Colon cancer SNPs were detected down to 0.1% mutant type.

4.4 PERSPECTIVES

The nanorod arrays developed in this work promise huge capabilities in molecular binding studies and single molecule detection. The sensitive detection capabilities of these nanorod arrays have many applications in disease diagnosis, including SNP detection and antibody-antigen binding.

By observing the LSPR shift of nanorods arrays, it was demonstrated that it is possible to detect the single nucleotide polymorphisms (SNP) of DNA. By comparing the spectra of an array of nanorods coated in a monolayer of probe DNA hybridized to healthy DNA to that of SNP mutated DNA that has been cleaved through nuclease interaction we observe a blue shift in the LSPR of the mutated DNA. Theoretically, any type of cancer that exhibits SNP mutation in DNA should be detectable using this LSPR method.

The binding of antigens to antibodies holds great promise for LSPR-based biosensing. For very small amounts of antigen present, there should be a measurable LSPR shift for a sensitive substrate, like the nanorod arrays developed in this work.

5 CHAPTER 5: PHOTOCHEMICAL NEAR-FIELD IMAGING

5.1 NEAR FIELD IMAGING

The visualization of the near-field of nanoparticles is of interest to identify the modes of excitation and to aid in the intelligent design of plasmonic structures for applications, such as biosensing.[128] By observing the effect of varying nanoparticle geometries and exposure parameters on the location and intensity of hotspots, plasmonic substrates can be designed for optimal electric field enhancement. Using a photosensitive polymer film deposited over the surface of nanostructures, the near-field excited in the particle induces molecular motion and imprints the features topographically into the surface of the polymer.

The azobenzene molecule has a double nitrogen bond that undergoes a conformational change when a photon is absorbed. Dispersed Red 1 (DR1) is an azobenzene-based dye that can be grafted to a polymer chain, such as PMMA, to make a photosensitive polymer. When a film of this polymer is exposed to an electric field gradient the DR1 undergoes cycles of isomerization and subsequent displacements, which then pushes large amounts of the bulky polymer. The molecular motion continues until it is outside of the areas of high electric field intensity, inducing topographical changes. The displacement of the matter is vectorial and therefore it is possible to image the different components of the near-field.

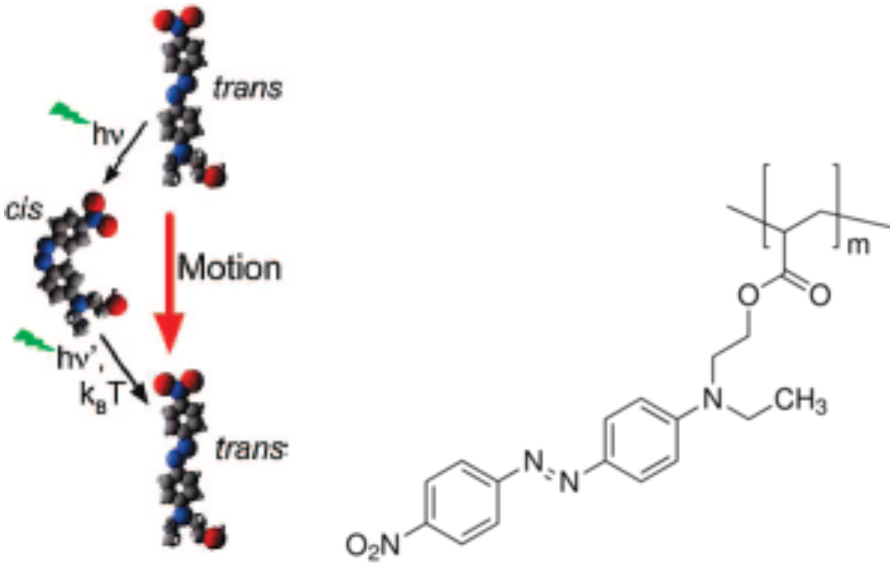

Figure 32: Chemical Structure of PMMA-DR1MA

The irradiation of DR1 causes a conformational change (left) that induces the molecule into translational motion. When grafted to a polymer chain (right), the motion of the DR1 pushes the polymer.

The topographical changes induced by molecular motion within electric field gradients can be imaged using atomic force microscopy (AFM). When the images of a nanoparticle coated with a photosensitive polymer are compared before and after irradiation, ridges and valleys in the polymer surface can be observed. These topographical changes indicate the locations of the hotspots of the plasmonic structures. In the hotspots, there is a locally confined electric field that causes molecular motion of the photosensitive polymer.

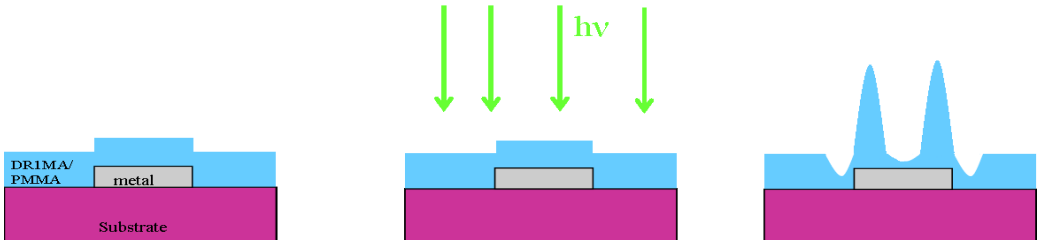

Figure 33: Photochemical Near-Field Imaging Process

DR1MA/PMMA is spin coated over substrate. Then the substrate is irradiated causing high electric field gradients in the hotspots of the nanoparticles. The DR1 undergoes conformational changes in the areas of high electric field intensity, and molecular motion ensues until the DR1 has moved to areas of low electric field intensity.

DR1 has been used by Hubert et al for directly observing the near-field plasmonic modes of metal nanostructures. [50-51, 129-133] Near-field studies making use of photosensitive polymers have been conducted previously on bowtie nanoantennae, which showed experimental electric near-field features were well correlated with simulations.[55, 132] These studies were conducted on large bowties with resonances well outside the range of the absorption band of DR1, therefore only off-resonance modes were able to be experimentally imaged. The mode of greatest interest with bowtie nanoantennae is the longitudinal mode, which produces a strong, highly localized hotspot in the junction

between the prisms. The absorption band of DR1 is approximately 400 to 600 nm, as shown in Figure 34. Using single-photon absorption of DR1, the near-field of metallic nanostructures excited by wavelengths in this range can be imaged. The modes excited in many nanostructures within this wavelength range may be of limited interest if they are far from the LSPR of the structures. Using high quality fabrication it would be possible to study smaller bowties and other structures with resonances within the absorption band of DR1.

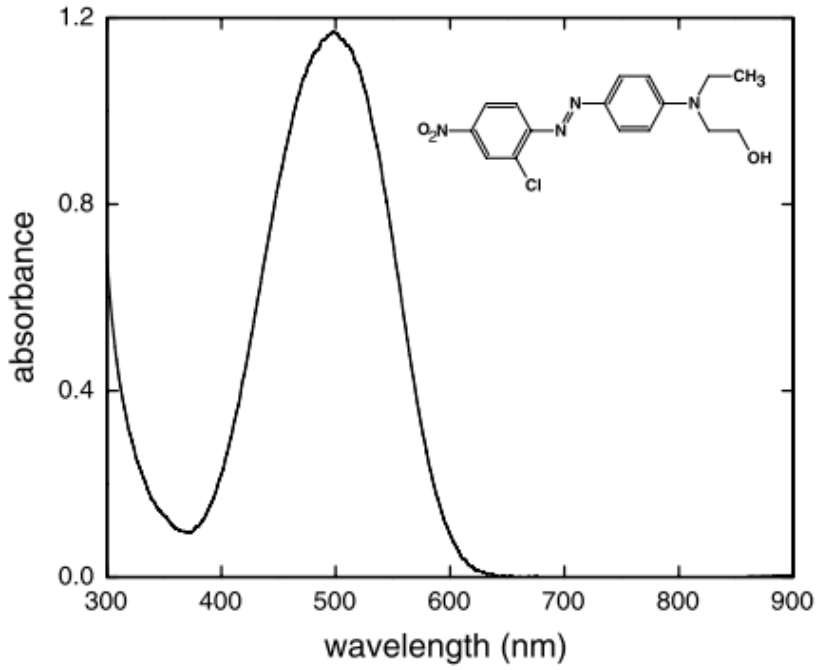

Figure 34: Absorbance Spectrum of DR1

For single photon absorption of DR1 the usable wavelengths range from around 400 nm to 600 nm.

In this work, the limiting factor on the prism size in bowtie nanoantennae was the fabrication quality. The smallest prisms with highly defined features that we were able to fabricate were 140 nm, and the smallest gaps were 4 nm. The modes of most interest for these geometries of bowtie antenna are generally in the red and infrared regime, which is well outside of the absorption band of DR1. Chapter 4 includes a rigorous study of the LSPR of varying geometries of bowtie nanoantennae. An example of the simulated LSPR of a bowtie with 150 nm prism sides and 10 nm gap is shown in Figure 35. The transverse mode is resonant at 800 nm and the longitudinal mode is resonant at 1000 nm.

Theoretically, two-photon absorption of DR1 could be used to image plasmonic modes in the 700-1200 nm regime.

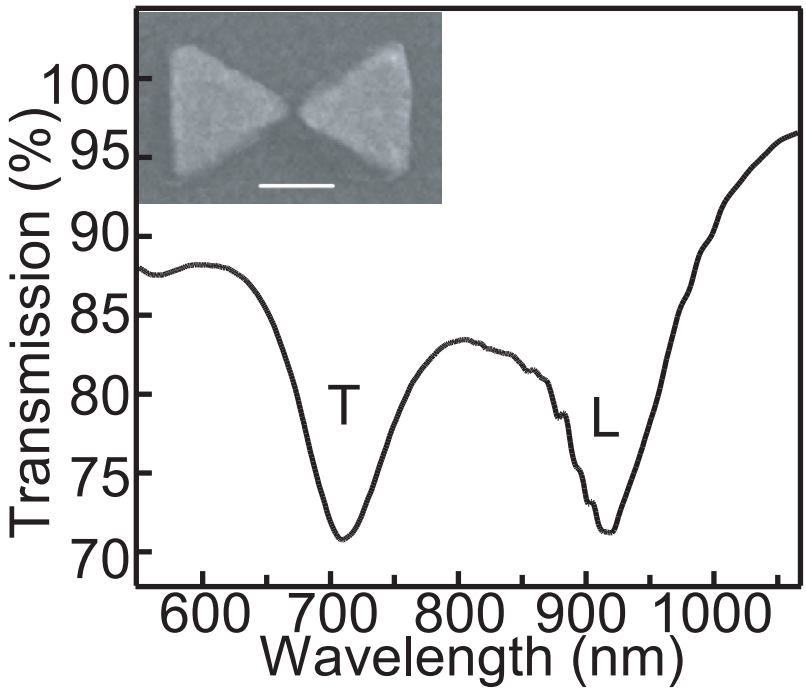

Figure 35: Transmission Spectrum of a Bowtie Nanoantenna

The longitudinal (L) and transverse (T) excitation modes of an array of gold bowtie nanoantennae with 150 nm side lengths and a 5 nm gap between prisms. Inset shows SEM image of typical bowtie. Scale bar is 100 nm.

In this chapter both single-photon and two-photon absorption of DR1MA is used to induce molecular motion in electric field gradients due to focused laser spots and in the hotspots of plasmonic nanoparticles. The longitudinal, transverse, and off-resonance modes of bowtie nanoantennae are imaged using a thin film coating of DR1MA over the nanostructures. The effect of bowtie gap on the near field features is also observed using photochemical imaging.

5.2 METHODS

Simulation of the electric field contour plots was carried out using the DDA in the DDSCAT program.[69, 74] DDSCAT version 7.0 and a 1 nm grid were used for all simulations. The dielectric constants of Au are from Johnson and Christy.[78] The electric field intensity and thus the average and maximum intensity over the nanoparticle surface were calculated for isolate targets in an effective medium of refractive index 1.331. The

information was used to make contour plots of the intensity on and around the nanoparticle to visualize the location of the hotspots.

Photochemical near-field imaging was done using an approach similar to those reported by Haggui and coworkers.[134] DR1MA was mixed in ambient conditions with 1-1-2-trichloroethane in concentrations ranging from 5 to 30 g/L. A thin film of DR1/PMMA was spin coated onto the substrate at speeds ranging from 2500 to 4000 rpm. By varying the concentration and spin speed, the thickness of the film was controllable. The thinnest film achieved was 15 nm, from a 5 g/L solution spun at 4000 rpm. The thickest film produced was 100 nm, resulting from a 30 g/L solution spun at 2500 rpm.

AFM images were taken of polymer-coated nanoparticles on a Bruker BioScope AFM. The AFM tips used were approximately 5 nm in diameter, resulting in a feature size error of about 5 nm. The height scale and amplitude error were adjusted so as to be as small as possible to give maximum feature contrast. A slow scan speed of 0.5 Hz was used to ensure an accurate reading of the height. The resolution was adjusted to 1024 pixels to maximize the resolution of the image.

For single-photon absorption based photochemical imaging experiments, the sample was exposed at 568 nm using an Ar-Kr continuous, plane wave source, with a power of 200 mW/cm^2, for 40 minutes. For two-photon absorption based photochemical imaging experiments the sample was exposed using a tunable, pulsed Ti: Sapphire focalized laser. The wavelengths ranged from 700 to 1000 nm and the power ranged from 30 mW to 1 W. The exposure time ranged from 1 second to 40 minutes. AFM images were taken after excitation of the nanoparticles. Differential images were obtained through post processing image subtraction.

5.3 Results

5.3.1 Simulated Near Field Imaging

Contour plots of the electric field of bowtie nanoantennae were calculated in order to predict the features and intensities of the local electric field. By precisely controlling the parameters of wavelength, geometry, and polarization, the theoretical features of various modes can be forecasted.

Simulated electric field contour plots were calculated using DDA for 568 nm excitation, as shown in Figure 36a-d, in order to predict the electric field induced by

single photon absorption based photochemical imaging. Figure 36a and b show the simulated total electric near-field, $|E|^4$, contour plots for a 6 nm and 10 nm gap respectively. The notable hotspot features are along the edges of the prisms, not on any of the prism corners. Due to the molecular motion response of DR1MA to plasmonic hotspots, the out of plane component of electric field has been shown to have a greater impact than in plane components on topographical changes during photochemical imaging.[134] For this reason, the vector components of the electric field were also simulated, where the total field intensity is given by

$$|E|^4 = \left(|E_x|^2 + |E_y|^2 + |E_z|^2\right)^2 \qquad (5\text{-}1)$$

where $|E_x|^2$ and $|E_y|^2$ are in plane components, and $|E_z|^2$ is the out of plane component of the electric field. Figure 36c and d show the out of plane component of electric field, $|E_z|^2$, contour plots for a 6 nm and 10 nm gap, respectively. The out of plane component shows a cold spot in the center of each prism.

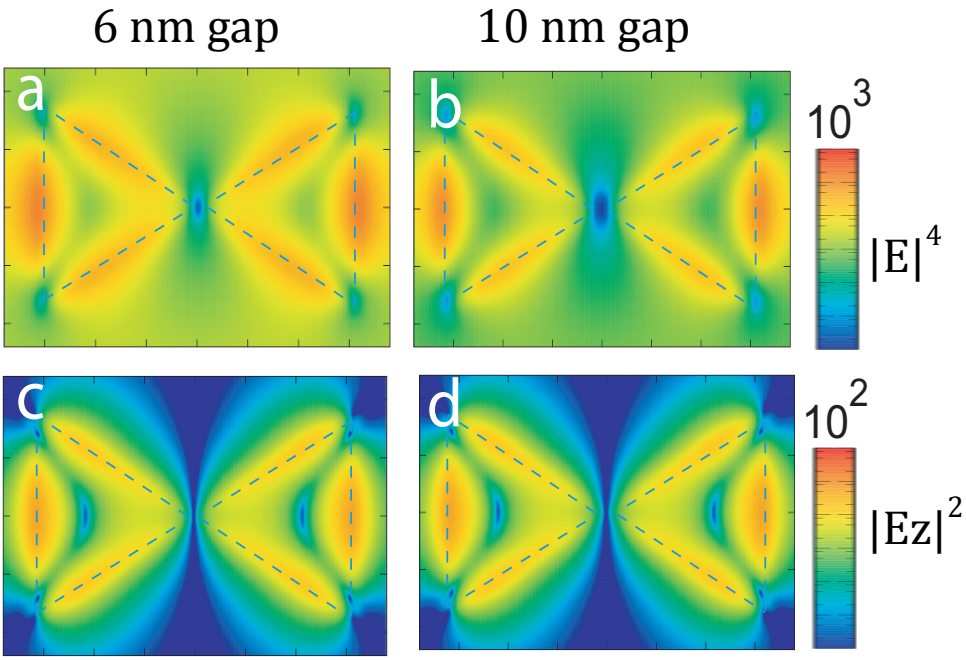

Figure 36: Simulated Electric near-field at 568 nm

a-d) Simulated electric near-field of bowtie nanoantennae with a and c) 6 nm gap and b and d) 10 nm gap between prisms. a and b) Simulated total electric near-field, $|E|^4$, contour plot. c and d) Simulated out of plane component of electric field, $|E_z|^2$, contour plots.

The longitudinal and transverse modes of the bowtie nanoantennae studied in this work are in the red and infrared region of the spectrum, an example of which is shown in Figure 35. Simulating the electric field contour plots of bowties excited at 890 nm shows the expected near field features for modes, as shown in Figure 37. The longitudinal mode displays a central hotspot in the junction between the prisms. The transverse mode does not exhibit this central hotspot, instead it shows hotspots on the four outer corners of the bowtie.

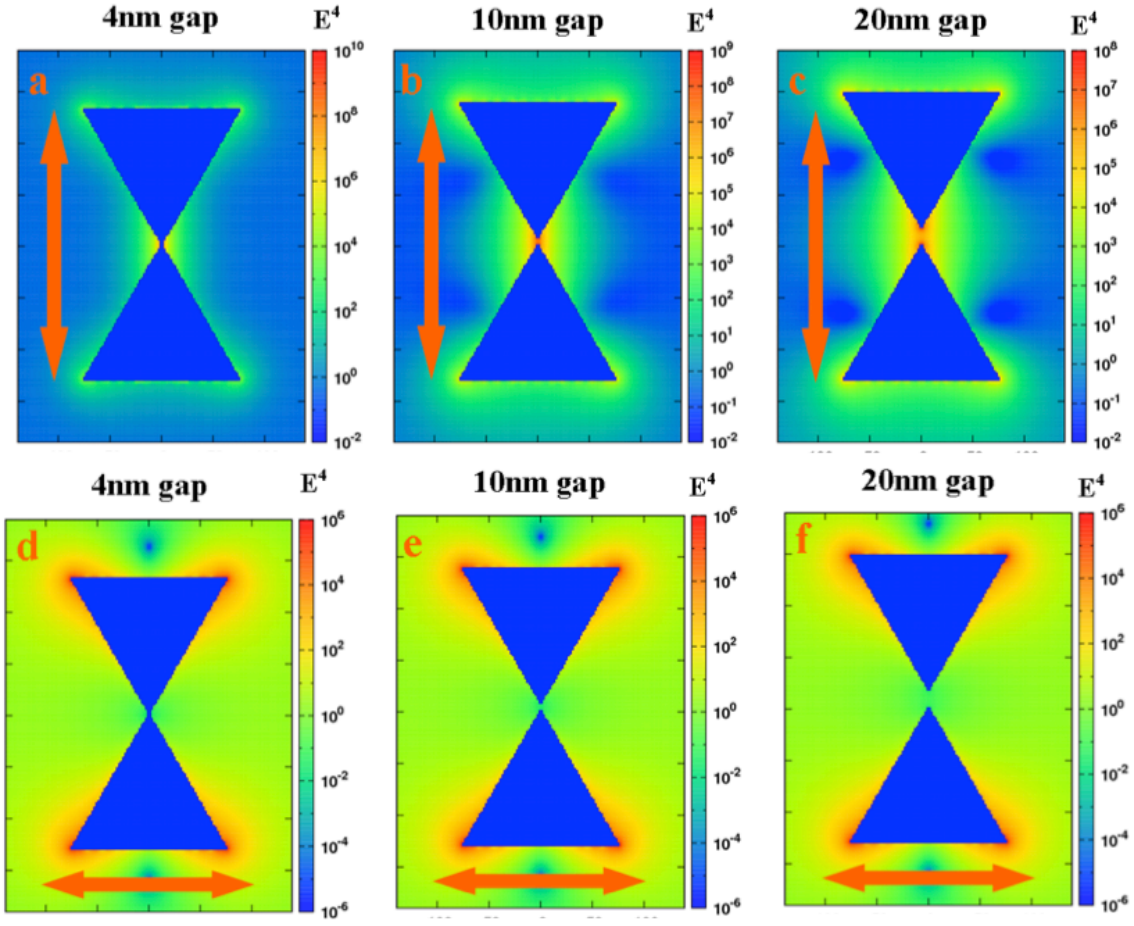

Figure 37: Simulated Electric Near-Field at 785 nm

Simulate electric near-field contour plots of bowtie nanoantennae. Top row shows longitudinal polarization for a variety of gap sizes: a) 4 nm, b) 10 nm, c) 20 nm. Bottom row shows transverse polarization for a variety of gap sizes: d) 4 nm, e) 10 nm, f) 20 nm.

The thickness of the photosensitive polymer layer used in imaging could affect what near-field features are imprinted in the topography of the polymer surface. Simulation of the electric near-field at different heights above the surface of a bowtie with

a large gap, excited at 900 nm with longitudinal polarization, shows a decrease in both the electric field intensity and localization, shown in Figure 38. The hotspot located in the junction of the prisms weakens and delocalize as the distance from the surface of the nanoparticle increases. The near-field present at various heights above the surface of the nanoparticle may be simulated and studied for the possible identification of experimental features.

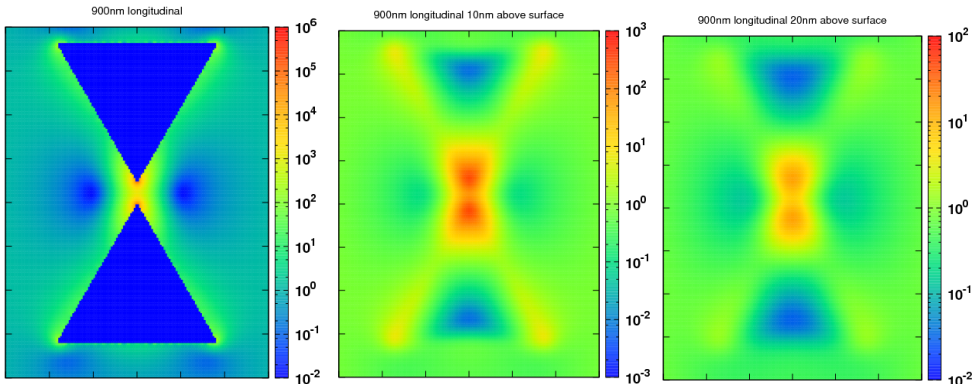

Figure 38: Electric field simulations Above Nanoparticle Surface

DDSCAT simulations of the electric field at different heights above a bowtie nanoantennae. The images from left to right represent simulation heights of 0, 10, and 20 nm above the nanoparticle surface.

5.3.2 Experimental Near field Imaging

Photochemical near-field imaging was used to experimentally map the near-field of bowtie nanoantennae with 568 nm excitation, as shown in Figure 39. Figure 39a and d show an AFM image before exposure for a bowtie with 6 nm and 10 nm gap between prisms, respectively. After exposure to an external electromagnetic field, the near-field features will have changed the surface of the polymer, as shown in Figure 39b and e, for a 6 nm and 10 nm gap respectively. In order to better visualize the changes in the polymer surface, differential images were made using image subtraction between the AFM images taken before and after exposure, as shown in Figure 39c and f for 6 nm and 10 nm gaps respectively. The features visualized in the photochemical near-field experiment showed good agreement with the features in the electric field contour plots; the hotspot was localized along the edges of the prisms for all gap sizes for both experiment and simulation.

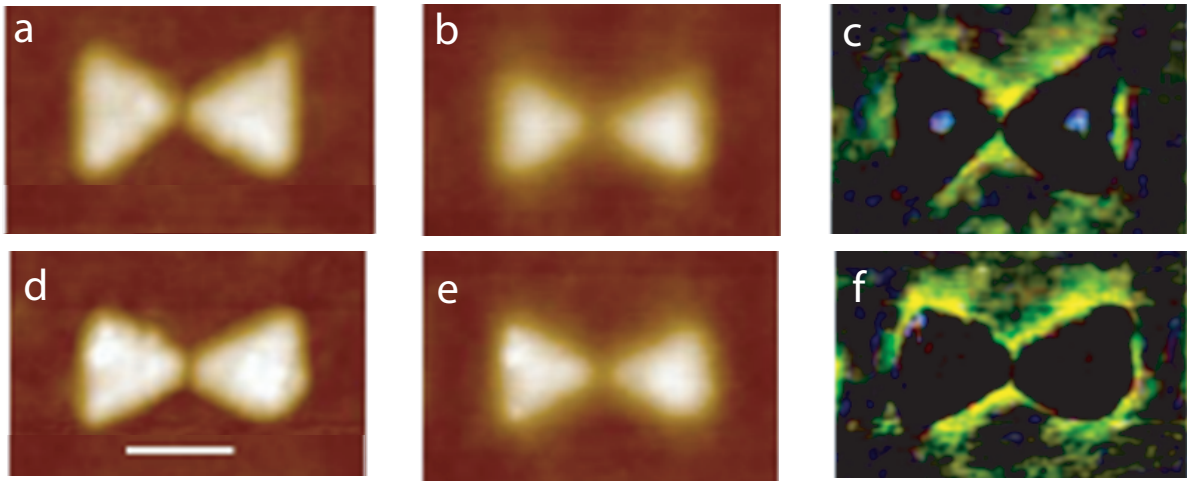

Figure 39: Photochemical Imaging

Experimental near-field imaged using photosensitive polymer film for a-c) 6 nm gap between prisms and d-f) 10 nm gap between prisms. a) and d) are AFM images taken before exposure. b) and e) are AFM images taken after exposure. c) and f) are differential images made using image subtraction to view the effect of the near-field. Polarization is longitudinal for all near-field simulated and experimental images.

5.3.3 Developing Two-Photon Induced Molecular Motion

To experimentally image the modes of nanostructures that fall outside of the absorption band of DR1, one could induce molecular motion through the two-photon absorption of DR1. The two-photon absorption of DR1 is statistical, and by using a high power, pulsed laser the chances of two-photon absorption occurring is increased. Table 2 shows power measurements of a laser of different wavelengths before and after passing through a thin film of DR1 polymer.

TABLE 2: TWO-PHOTON ABSORPTION POWER MEASUREMENTS OF DR1 POLYMER FILM

λ (nm)	I_0 (mW)	I (mW)	A
800	906	818	0.044374894
820	902	815	0.044048929
840	901	815	0.043567182
860	899	814	0.043135287

880	901	800	0.051634804
900	902	805	0.049410657
920	902	818	0.042453234
940	901	820	0.040910939
960	901	820	0.040910939
980	902	820	0.041392685

The absorption can be calculated based on the power difference observed before and after the DR1 film.

$$A = -log_{10}\frac{I}{I_0} \qquad (5\text{-}2)$$

where A is the absorption, I_0 is the power measured before the film, and I is the power measure after the film. The calculated absorption can be plotted over the wavelengths measured to achieve a rough, two-photon based absorption spectra, shown in Figure 40, which shows a peak around 880 nm.

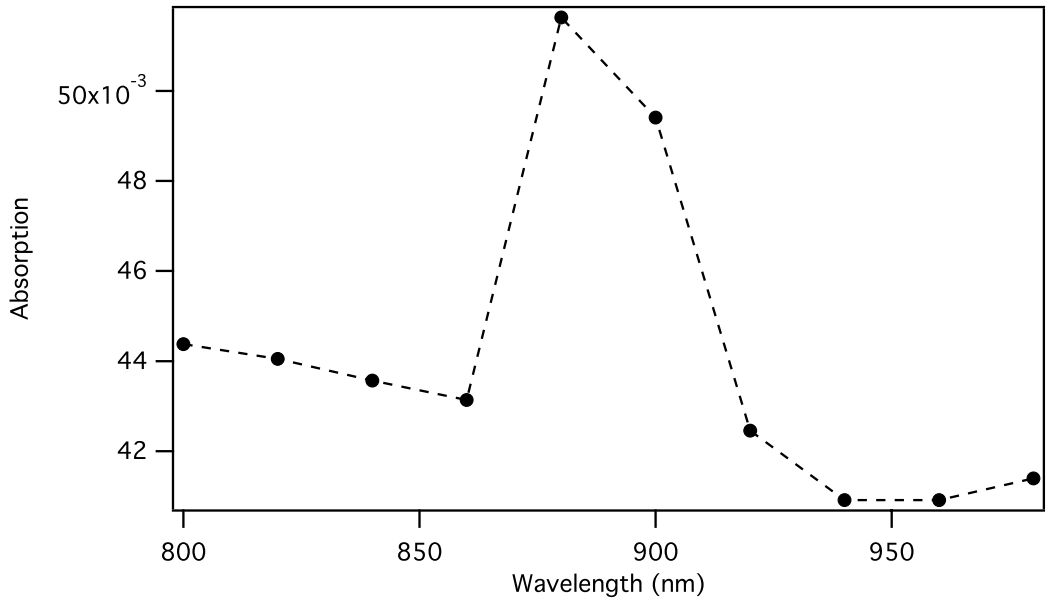

Figure 40: Two-Photon Absorption Spectra of DR1 polymer

The two-photon absorption spectra of DR1 polymer as calculated by the change in power before and

after the laser has passed through a thin film of DR1 polymer.

Using a focused laser spot to create an electric field gradient in an 80 nm film of DR1 polymer, molecular motion was induced using two-photon absorption, as shown in Figure 41. The gradient induced by the focalized laser spot is dependent on many variables. Objectives with higher numerical apertures induce a greater out of plane component, leading to quadrupole-like features. Varying the power and exposure time led to a range of areas and types of molecular motion. Very long exposure times and high power lead to exaggeration of the spot shape, sometimes showing that the induced motion was asymmetric. The concentric ring features of the Airy pattern were apparent in all exposures that resulted in molecular motion.

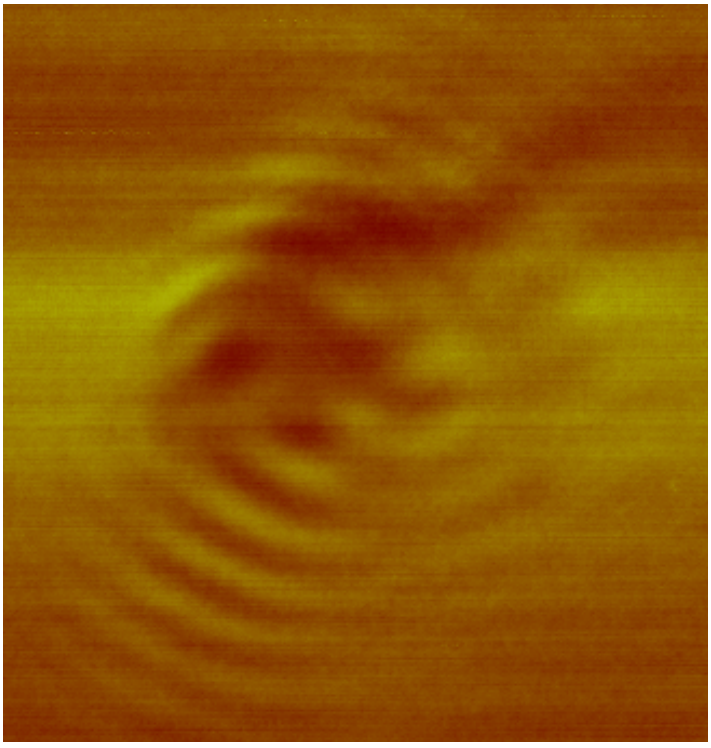

Figure 41: Molecular motion of DR1 Induced by Two-Photon Absorption

Molecular motion was induced using the two-photon absorption of a DR1MA film 80 nm thick. A focalized laser with 0.9 µm spot at 1000 nm with 900 mW was used to expose an 80 nm thick DR1MA film for 2 minutes. An area of molecular motion induced topographical changes 10 µm wide was imaged using AFM.

5.3.4 TWO-PHOTON ABSORPTION INDUCED NEAR FIELD IMAGING

By adjusting the technique developed for two-photon absorption induced molecular motion in focalized laser spots on plain polymer film, the near field features of modes in the red and infrared regime could be imaged. To image the excited modes of metallic nanoparticles it would be necessary to use a low power to not affect particle shape and long exposure time to allow the dynamics of the system to settle.

The on-resonance modes of a bowtie nanoantennae were excited at 890 nm and imaged using DR1MA, as shown in Figure 42. At this wavelength, depending on polarization, the longitudinal and transverse modes are resonant. Using the photochemical imaging technique developed, these modes were excited at one photon and induced two-photon absorption based molecular motion of DR1. The topographical changes were imaged using AFM, and we can clearly see the features predicted by simulation. The longitudinal mode has a strong central hotspot in the junction between the prisms and the transverse mode has hotspots on the four outer corners of the bowtie.

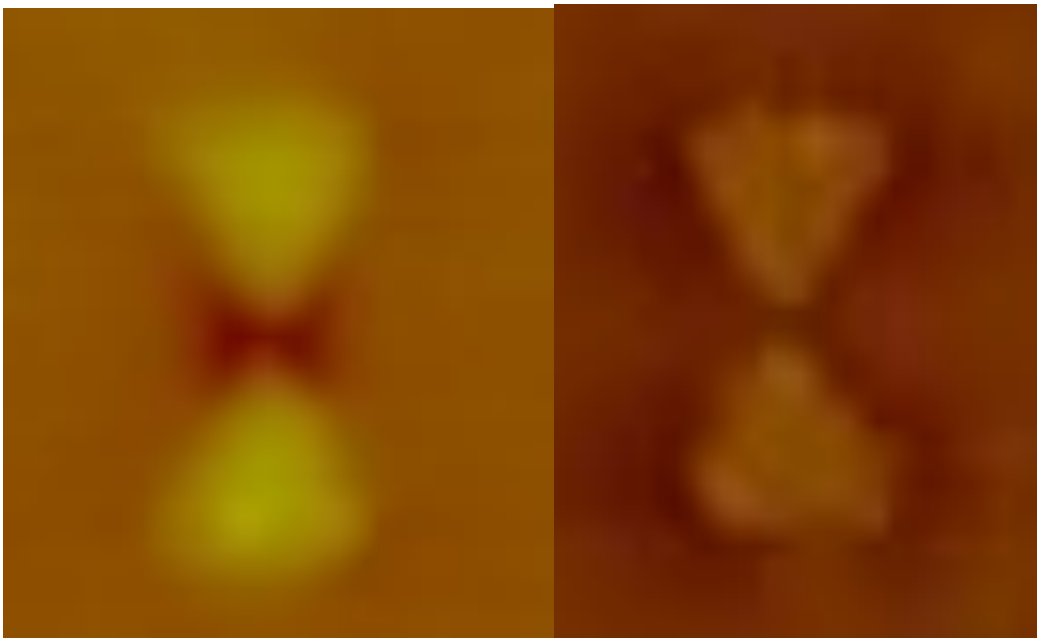

Figure 42: Photochemical Near-Field Imaging of Polarization Dependence

Photochemical near-field imaging of longitudinal (left) and transverse (right) modes of bowtie nanoantennae using the two-photon induced molecular motion of DR1MA. The excitation wavelength was 890 nm.

The effect of gap spacing on the electric near-field of bowtie nanoantennae is of interest to observe experimentally. According to simulations and previous studies, bowtie nanoantennae with small gaps between prisms exhibit very strong electric field localization in the junction between the prisms. Bowties with large gaps between prisms do not exhibit the central hotspot; instead, near-field excitation occurs along the edges of the prisms. Using the two-photon absorption of DR1, the near field features of various bowtie gap sizes were imaged, as shown in Figure 43. The bowties with small gaps, 4 to 8 nm, show a highly defined hotspot in the junction between prisms. The larger bowties, with 20 to 30 nm gaps, show a local field along the edges of the prism with no central hotspot. These experimental features show an excellent correlation with the trends observed in simulation, a dissipation of the central hotspot with increasing gap size. The thick layer of polymer used implies that the near-field far above the surface of the particle may be affecting the polymer and needs to be considered.

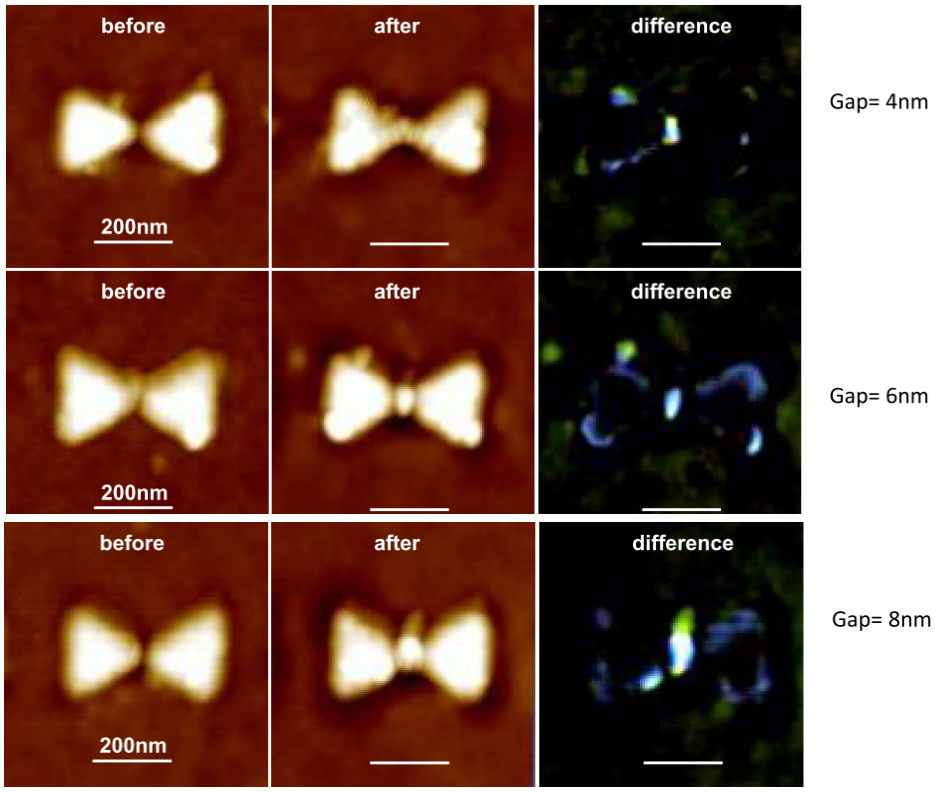

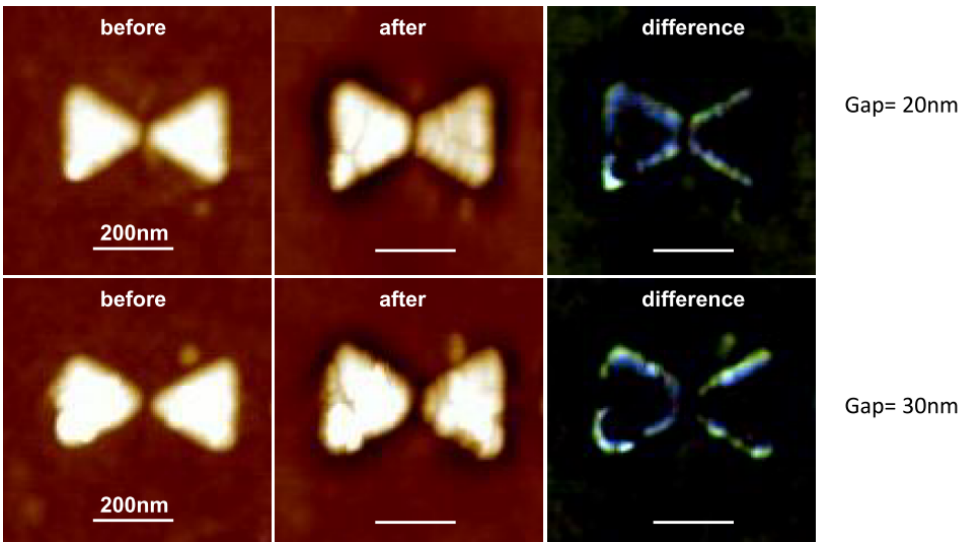

Figure 43: Photochemical Imaging of the Longitudinal Mode Excitation of Bowtie Nanoantennae

DR1MA/PMMA coated bowtie antennae, before (left) and after (center) irradiation, and differential image subtraction (right) for varying gaps between prisms.

5.4 CONCLUSIONS

In order to design and optimize plasmonic sensing substrates, it is necessary to verify the near-field features of nanostructures. In this chapter, a photosensitive polymer was used to image the electric field gradient of a focalized laser spot and the hotspots of plasmonic structures. The modes of bowtie nanoantennae at different wavelengths and polarizations were imaged. Normal, one-photon absorption of DR1MA/PMMA allowed the imaging of an off-resonance mode at 568 nm. This mode excited the near field around the edges of the prisms, but is considered less interesting than other stronger modes at longer wavelengths. In order to visualize modes in these longer wavelengths, a recipe was developed to accomplish near-field imaging using two-photon absorption based molecular motion of DR1. The electric field gradient of a focalized laser spot was imaged using a high power, pulsed laser at wavelengths well outside the absorption band of DR1. The experimental near-field features observed for off-resonance, longitudinal and transverse modes correlated to the electric field features simulated in DDSCAT. As predicted by simulation, the experimental near-field feature for the longitudinal mode of bowtie nanoantennae, the central hotspot, dissipates with increasing gap size.

5.5 PERSPECTIVES

The near-field technique developed can be used for imaging a wide variety of nanostructures. Using single and two-photon absorption of DR1MA the modes of plasmonic nanostructures within the range of 400 to 1000 nm can be imaged. There are many interesting nanostructures, such as metamaterials, which simulations have shown to have complex near field features. Using the molecular motion of photosensitive polymers, it would be possible to have experimental evidence of these complex features. Time resolved studies could illuminate the changes in the near electric field of nanostructures over time. Potentially, using very short exposure pulses, the stages of near field excitation could be imaged using AFM, since the polymer is stable when not in an electric field gradient.

6 CHAPTER 6: BOWTIE NANOANTENNAE

6.1 SURFACE ENHANCED RAMAN SCATTERING SENSING

Sensitivity is a key factor in the improvement of nanoparticle-based biosensors. Bowtie nanoantennae have shown high sensitivity for surface enhanced Raman scattering (SERS) based biosensing. In this work, optical bowtie nanoantennae with varying geometries were simulated, fabricated, and characterized. We successfully fabricated sub-5 nm gaps between prisms. The gap between prisms, prism size, and radius of curvature of the prism corners were characterized for their effects on the optical and electromagnetic properties. Bowties were described using simulations of particle scattering and electric field intensity as well as experimental characterization of localized surface plasmon resonance and surface enhanced Raman scattering. The results indicate that the bowtie gap and the radius of curvature of the prism corners have an important effect on the surface enhanced Raman scattering abilities of a nanoparticle array. The trends described herein can be utilized to intelligently design highly sensitive SERS biosensing substrates.

Metallic nanostructures including both chemically synthesized nanoparticles and nanostructures by top-down fabrication have been demonstrated as effective SERS substrates, which can be used towards highly sensitive and specific biosensing.[56] SERS biosensing involves the use of enhanced local electric fields of plasmonic devices to increase the Raman signal of biomolecules and biomarkers. These increased signals mean that lower concentrations of biomarkers still produce readable signatures and allow for detection with much lower sample volume or very low concentration samples.

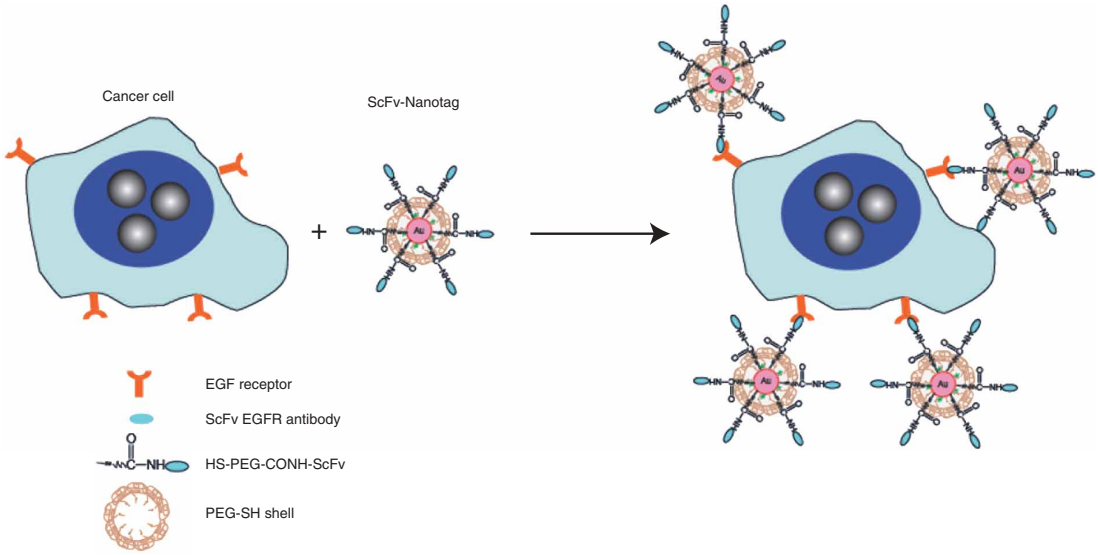

FIGURE 44: CANCER CELL TARGETING USING ANTIBODY-CONJUGATED SERS NANOPARTICLES.

Preparation of targeted SERS nanoparticles by using a mixture of SH-PEG and a hetero-functional PEG (SH-PEG-COOH). Covalent conjugation of an EGFR-antibody fragment occurs at the exposed terminal of the hetero-functional PEG. Adapted from Qian et al.[135]

The Raman enhancement factor is a quantitative measure of the increase in Raman signal due to the enhanced electric field in SERS substrates. The enhancement factor is given by:

$$EF = \left(\frac{N_{bulk}}{N_{SERS}}\right)\left(\frac{I_{SERS}}{I_{bulk}}\right) \qquad (6\text{-}1)$$

where N_{bulk} is the number of molecules in the bulk sample, N_{SERS} is the number of molecules on the SERS sample, I_{bulk} is the intensity of the Raman signal for the bulk sample, and I_{SERS} is the intensity of the Raman signal for the SERS sample. With high sensitivity SERS biosensors, the earlier diagnosis of diseases, such as cancer, leads to more effective, early treatment and higher survival rates.

SERS-based biosensors can be used for disease detection through the identification of biomarkers through their Raman fingerprint. Many types of biomarkers have been used for SERS-based disease and cancer detection, such as monoclonal antibodies, peptides, and epidermal growth factor receptor, shown in Figure 44 and Figure 45.[135-140]

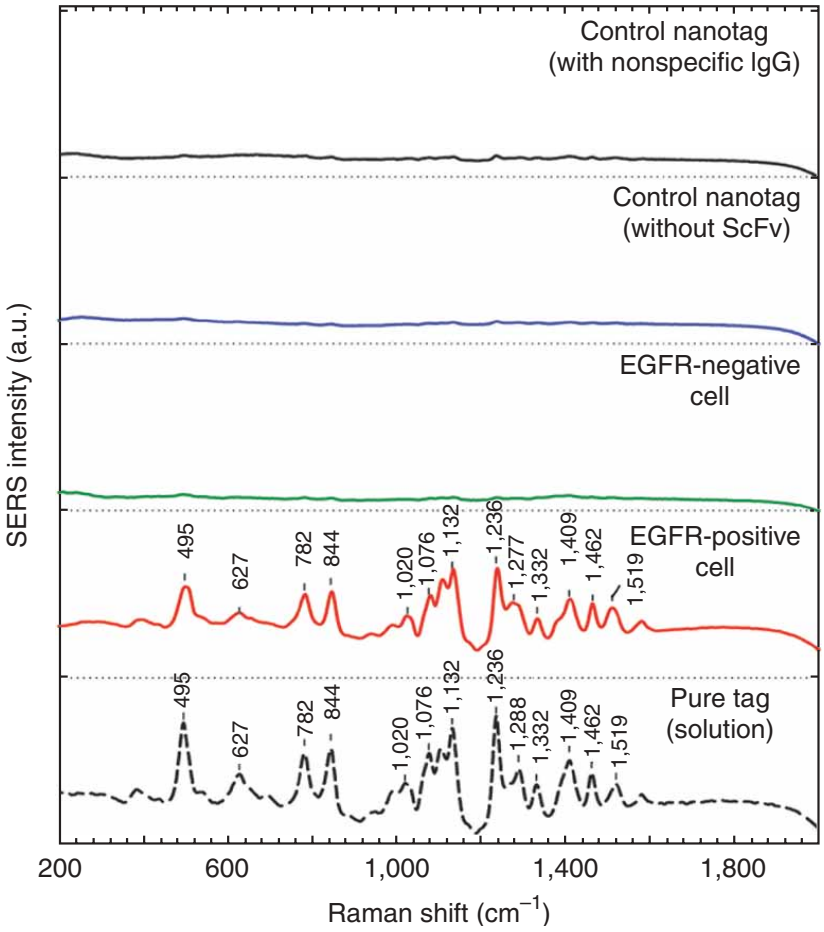

FIGURE 45: CANCER CELL DETECTION USING ANTIBODY CONJUGATED NANOPARTICLES

SERS spectra obtained from EGFR-positive cancer cells (Tu686) and from EGFR- negative cancer cells (human non-small cell lung carcinoma NCI-H520), together with control data and the standard tag spectrum. All spectra were taken in cell suspension with 785-nm laser excitation and were corrected by subtracting the spectra of nanotag-stained cells by the spectra of unprocessed cells. The Raman reporter molecule is diethylthiatri- carbocyanine (DTTC), and its distinct spectral signatures are indicated

by wave numbers (cm–1). Adapted from Qian et al.[135]

Various geometries of nanoparticles have been explored previously for SERS potential. Particle shape, size and material will affect the location and intensity of hotspots and the optical and electromagnetic properties of the particle.[13] The contours of roughened metal surfaces [18, 141-142] and solution grown aggregated particles [143-144] were shown to exhibit enhanced Raman signals. Experimental work exploring sub-5 nm gaps in other geometries such as spherical dimers has shown great potential for increased SERS enhancement factor in this regime.[145-146] Spherical, cylindrical and rectangular

prisms were found to be inferior to bowtie nanoantennae, prism dimers facing tip to tip, for electric field enhancement.[79]

A variety of different types of bowtie substrates have been explored for their potential as high sensitivity biosensors. Nanosphere lithography fabricated bowties offer good homogeneity and reproducibility, but have limited geometries.[147] Structures fabricated using electron beam lithography can be controlled in the nanometer regime for independent variation of geometrical parameters.[148-149]

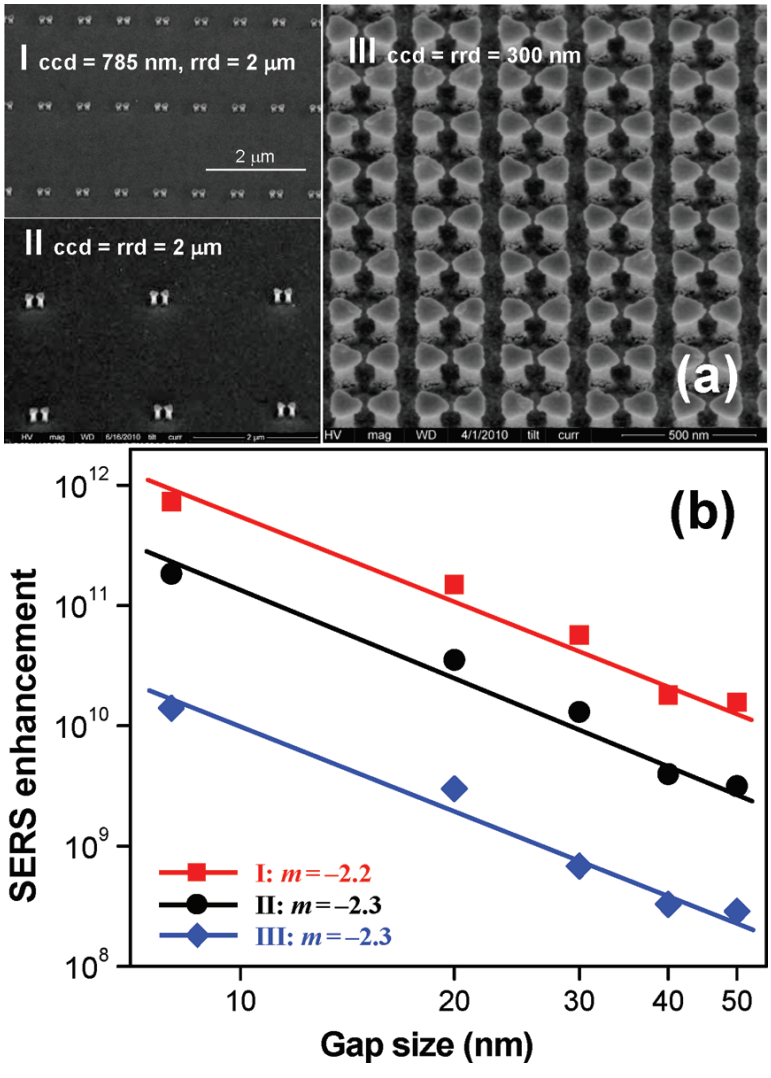

FIGURE 46: GOLD BOWTIE ARRAYS FOR SERS SENSING

Determination of the gap size dependence and the long-range collective plasmonic effects in SERS enhancement using elevated gold bowtie nanoantenna arrays. (a) SEM images of the elevated gold bowtie arrays with varying center-to-center distance in rows along the bowtie axis, and row-to-row distance. (b) A log-log plot of SERS enhancement factors as a function of bowtie nanogap size in arrays I, II, and III with different bowtie spacing. The slope is determined by fitting the power-law relationship of $EF \propto Ad_m$ *to*

the experimental data. Adapted from Hatab et al.[96]

The gap size between prisms in bowtie nanoantennae has been explored previously and decreasing gap size was found to redshift the resonance.[150-151] The Raman signal increased with decreasing gap size up to the limit of fabrication, which previously was an 8 nm gap for a bowtie nanoantenna.[96] Simulations have predicted that the electric field enhancement will continue to increase with decreasing gap size until the range at which quantum effects dominate and the enhancement starts to decrease.[79] Recently, bowtie nanoantennae with gaps in the sub-5 nm regime have been studied for electron energy loss by scanning tunneling electron microscopy.[152] These previous studies inspire great interest in studying bowties with sub-5 nm gaps for potential biosensing applications. Bow angle has been explored for bowtie nanoantennae, and the resonance was found to first blueshift then redshift with increasing bow angle.[153] To the best of our knowledge the effect of radius of curvature (ROC) of the prism corners has not been isolated experimentally and explored.

We show in this chapter the large scale, reproducible fabrication of bowtie nanoantennae systematically exploring how the scattering properties, and electric field enhancement change as a function of the geometry of nanoantennae. The bowtie gap size, prism size, thickness and radius of curvature of the prism corners were explored. Bowtie nanoantennae with varying geometric parameters have been fabricated reproducibly in the sub-5 nm regime and characterized. The SPR was characterized by discrete dipole approximation (DDA) scattering calculations and spectroscopy measurements. The electric field was characterized by DDA electric field mapping, Raman spectroscopy, and photochemical near-field imaging (see Chapter 5).

6.2 Design, fabrication and Testing of Bowtie Antenna Arrays

Simulation of the particle scattering was carried out using the DDA in the DDSCAT program.[69, 74] DDSCAT version 7.0 and a 1 nm grid were used for all simulations. The dielectric constants of Au are from Johnson and Christy.[78] The electric field intensity and thus the average and maximum intensity over the nanoparticle surface were calculated for isolate targets in an effective medium of refractive index 1.331. The information was used to make contour plots of the intensity on and around the nanoparticle to visualize the location of the hotspots. The extinction efficiency was

simulated for multiple wavelengths to produce spectra used to determine the resonance position of the particle.

Electron beam lithography (EBL) was used to fabricate the bowtie nanoantenna arrays. The same polymer layer was used for all chips, 950 poly (methyl methacrylate) (PMMA) A4. The PMMA was spin coated onto the chips using at 4000 rpm for 40 seconds (Specialty Coating Model P6700) and then baked at 180 °C for 15 minutes. EBL was performed using a JEOL JSM-7001F field emission scanning electron microscopy (FESEM) equipped with a Deben Beam Blanker and a nanometer pattern generation system (NPGS). After e-beam writing, the chips were developed for 75s in a solution of 1:3 methyl isobutyl ketone (MIBK):isopropyl alcohol (IPA) at room temperature. After development the chips were rinsed for 20s in IPA and blown dry using nitrogen or compressed air. Evaporation of 2 nm Cr and 30 nm Au was sequentially done in a thermal evaporator (Elite Engineering, Singapore). The chamber pressure of $2x10^{-7}$ Torr and evaporation rate of 0.6 Å/s was used for evaporation. Lift-off was done at room temperature in acetone for 2 hours followed by a sonication for 1 to 2 minutes at power level 2 (Crest Ultrasonics Powersonic P1100D). More information about the EBL recipe can be found in Chapter 2.

Bowtie geometry was confirmed by analysis in SEM. Statistical analysis was done for gap size and prism size at 30,000× magnification for 36 bowties per sample and was confirmed at 120,000× magnification for each sample. The nominally 5, 10, 15, 20, 25, 30 nm gaps had actual gaps of 5.5±1.5, 10.8±1.9, 12.1±3.2, 20.3±1.1, 26.1±1.3, 29.6±1.5 nm, respectively. The nominal prism side lengths of 180, 160, 140, and 120 nm had actual lengths of 179.8+4.0, 158.1+3.7, 139.9+3.8, and 108.8+3.3 nm, respectively. The sharp and round bowties had a tip radius of curvature of 16.6+2.8 and 28.8+2.0 nm, respectively. Round bowties had nominal gaps of 5, 10, 15, 20, 25 nm and actual gaps of 5.4±2.0, 9.9±1.6, 16.9±2.5, 19.6±1.1, 24.1±2.3 nm, respectively

Transmission spectroscopy on a microspectrophotometer (Craic, USA) with non-polarized light in air, with an angle of incidence of 90 degrees and an aperture size 15 μm was performed for three locations per sample. Each sampling measured around 225 bowties.

The molecule used for SERS experiments was 2-naphthalenethiol from Sigma-Aldrich. Substrates were incubated at room temperature in a solution of methanol with a concentration of 5 mM naphthalenethiol for 24 hours and then rinsed with methanol and

blown dry with nitrogen gas. Raman spectroscopy was conducted with a 785 nm excitation wavelength and a power of 2 mW. A 50× objective with a slit of 300 μm and a numerical aperture of 0.75 was used, with an integration time of 600 s per sample. Each sampling measured around 16 bowties. Three locations on each sample were tested for both polarizations, parallel and perpendicular to the antenna axis.

6.3 RESULTS

The LSPR of nanoparticles can be highly controllable and tunable. It was of interest to explore the LSPR of bowtie nanoantennae in order to better understand their optical properties. A highly controllable LSPR also has potential applications in designing sensitive binding event based biosensing platforms. The effect of the gap spacing between the prisms of a bowtie nanoantenna on optical properties was systematically explored by holding all other parameters constant and varying the gap between prisms.

A simulation using the DDA method has been carried out to identify the modes involved in the transmission spectra. As shown in Figure 47 for a bowtie nanoantenna with a size of 150 nm a gap size 20 nm, when the incoming irradiation polarization is parallel to the bowtie axis, the extinction efficiency has a peak around 800 nm. When the irradiation polarization is perpendicular to the gap, the peak is around 700 nm. It should also be noted that the extinction efficiency peaks for both polarizations of a single 150 nm prism are around 700 nm as well.

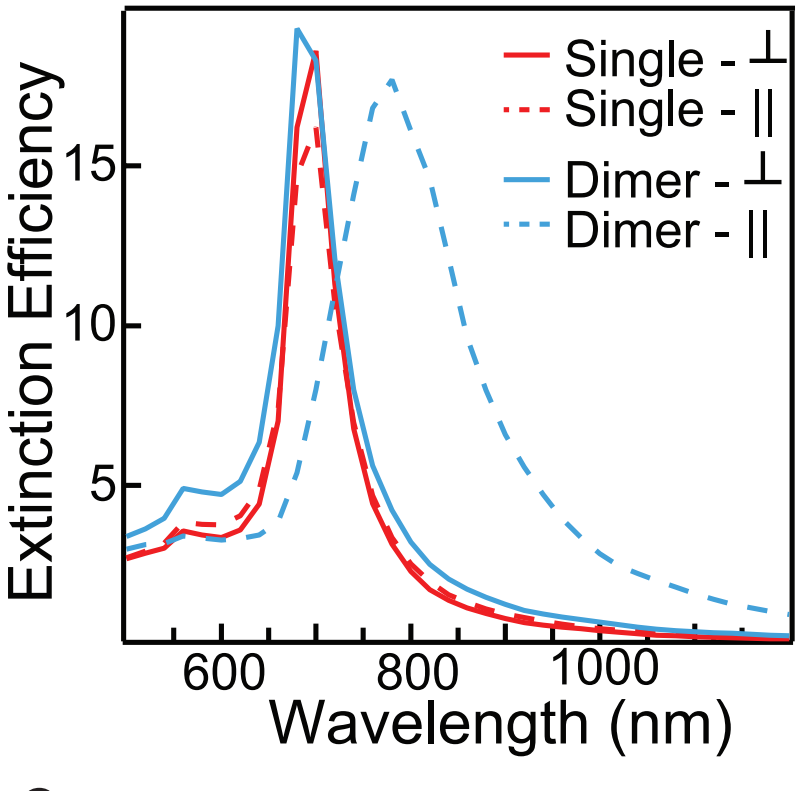

FIGURE 47: EFFECT OF DIMER COUPLING OF PRISMS ON EXTINCTION EFFICIENCY

Extinction efficiency of single prism and prism dimer for both polarizations. Calculations done in DDSCAT.

In Figure 49, we display the simulation results of extinction efficiency for a bowtie nanoantenna with gap spacing, δ, varied from 4 nm to 20 nm when the incoming irradiation is polarized along the gap, keeping the size (l = 150 nm) and thickness (t = 30 nm) constant. Unambiguously, the extinction shows a peak around 900 nm for a gap size of 4 nm. This peak red shifts significantly as the gap size is decreased from 20 nm to 4 nm, giving rise to an 800 nm peak for 20 nm gap. Simulations have also been conducted for the polarization perpendicular to the bowtie axis for different gap sized. The mode due to polarization perpendicular to the axis of the bowtie did not show noticeable resonance shift for different gap sizes and was similar to the resonances of single prisms. All of the gaps, 4 to 20 nm, for perpendicular polarization are shown overlaying each other in black color in Figure 49.

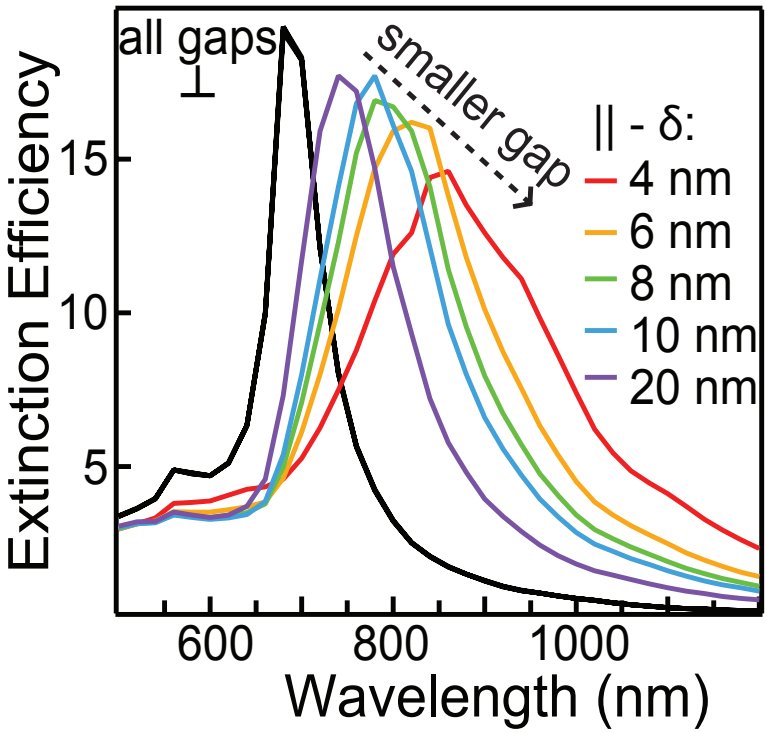

FIGURE 48: EFFECT OF GAP SIZE ON EXTINCTION EFFICIENCY

Extinction efficiency of prism dimers with varying gap spacing for both polarizations. Calculations done in DDSCAT.

The modes and effects of gap on resonance were studied by taking the transmission spectra of bowtie nanoantennae with gap spacings between 4 nm and 30 nm as shown in Figure 49. Two absorption bands were observed; one band around 700 nm does not vary with the gap spacing; while the other band redshifts as the gap spacing decreases. We observed that both resonance peaks are due to the two different polarization-based modes. In particular, the peak due to longitudinal polarization, parallel to the bowtie axis, shows systematic red shift with decreasing gap, as suggested by DDA simulation. The calculated extinction efficiency shows a different resonance for both the polarization parallel to and perpendicular to the bowtie axis. The peak corresponding to the perpendicular polarization does not vary with changing gap size while the peak corresponding to the parallel polarization redshifts with decreasing gap size. The transmission data shows two peaks, one of which remains constant with a gap change, and the other one redshifts with decreasing gap size. The correspondence of the transmission data to the calculated extinction efficiency implies that the two transmission modes must correspond to the two polarizations. The redshift with decreasing gap size implies a decrease in energy. This well-known behavior is explained by a weakening of

the restoring forces for the oscillating electrons due to the presence of the charge distribution of the second particle.[154]

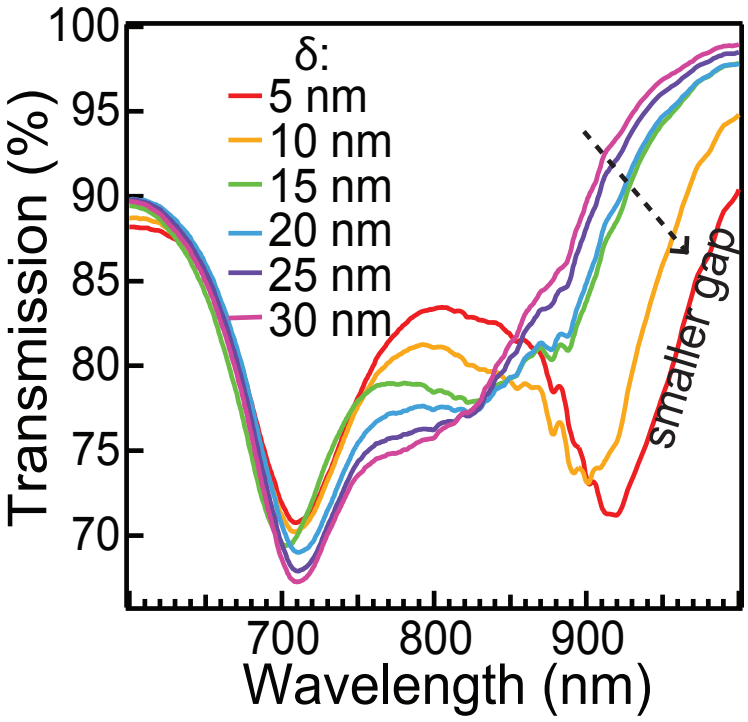

FIGURE 49: EFFECT OF GAP SIZE ON TRANSMISSION

Transmission spectra of prism dimers with varying gaps between prisms.

It was of interest to observe the effect of the side length of the prisms of a bowtie nanoantenna on its optical properties. First, the extinction of a variety of sizes of single prisms was calculated, shown in. Increasing prism size red shifts the resonance. By holding all other bowtie parameters constant and varying the side length of prisms, the LSPR has been explored systematically by both simulation and experiments. DDA extinction efficiency simulations were conducted for bowtie nanoantennae with varying prism size and gap spacing. Both polarizations, parallel and perpendicular to the bowtie axis, were simulated. Prism size was varied from 120 nm to 180 nm. Gap spacing was varied from 4 nm to 10 nm. The SPR for both modes, perpendicular and parallel to the axis, redshifted for increasing prism size. Optical transmission spectra were taken of bowtie nanoantennae with varying prism size and gap spacing, as shown in Figure 50 (left). Prism size was varied from 120 nm to 180 nm and gap size was varied from 4 nm to 30 nm. The two modes, for polarization perpendicular and parallel to the bowtie axis, redshifted for increasing prism size. The redshift with increasing prism size was more

dramatic for smaller gap sizes, as shown in Figure 50 (right). Both of the modes observed in extinction efficiency simulations redshifted with increasing prism size. The modes observed in transmission spectroscopy redshifted with increasing prism size, which agreed with simulation.

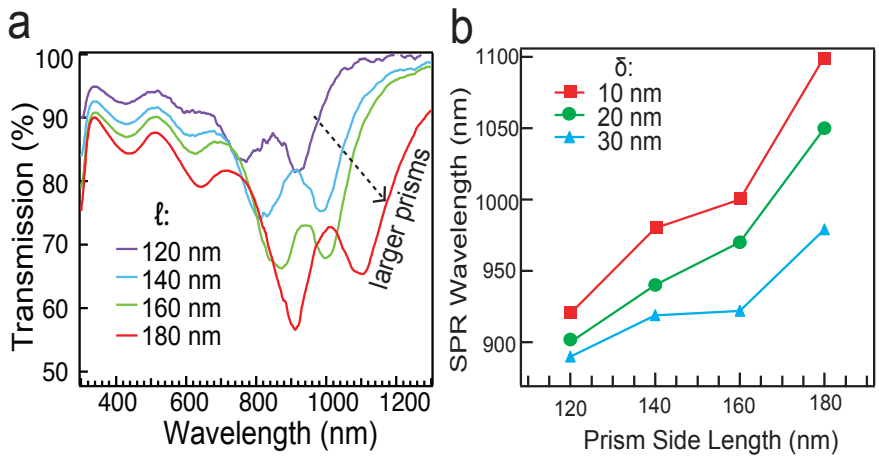

FIGURE 50: EFFECT OF PRISM SIZE ON TRANSMISSION

(a) Transmission spectra of prism dimers with varying prism side length. (b) Parallel mode SPR wavelength trends for several gap sizes of bowtie nanoantennae as prism side length is increased.

The engineering of hotspots and surface plasmon localization is of interest for its applications in SERS biosensing. The more localized an electric field hotspot is the more intense it is and thus will give more surface enhancement effects to Raman scattering signals. These enhanced signals allow for more sensitive detection of biomarkers. The effect of gap on electric field enhancement was studied through Raman spectroscopy, and DDA calculations on bowtie nanoantennae with gaps between prisms varying from 4 nm to 30 nm.

The Raman enhancement factor is a quantitative measure of the increase in Raman signal due to the enhanced electric field in SERS substrates. The enhancement factor is given by:

$$EF = \left(\frac{N_{bulk}}{N_{SERS}}\right)\left(\frac{I_{SERS}}{I_{bulk}}\right) \qquad (6\text{-}1)$$

where N_{bulk} is the number of molecules in the bulk sample, N_{SERS} is the number of molecules on the SERS sample, I_{bulk} is the intensity of the Raman signal for the bulk

sample, and I_{SERS} is the intensity of the Raman signal for the SERS sample. For this work, the number of molecules in the bulk sample was calculated by:

$$N_{bulk} = \pi R_{spot}^2 D_{bulk} \rho_{mol} \qquad (6\text{-}2)$$

where R_{spot} is the radius of the spot size of the excitation laser, D_{bulk} is the depth of the bulk sample, and ρ_{mol} is the molecular density of the bulk sample, given by

$$\rho_{mol} = \frac{\rho\, N_A}{w} \qquad (6\text{-}3)$$

where ρ is the density of the bulk sample (the number of grams per cubic centimeter), N_A is Avogadro's number (the number of molecules per mole), and w is the molecular weight (the number of grams per mole). The number of molecules in the SERS sample was calculated by:

$$N_{SERS} = \pi R_{spot}^2 \frac{S_{hotspot}}{S_{lattice}} \frac{1}{m} \qquad (6\text{-}4)$$

where $S_{hotspot}$ is the area of the hotspot excited, $S_{lattice}$ is the area of one lattice of the particle array, and m is the molecular footprint. In some works, the surface averaged enhancement factor is calculated. It should be noted that in this work the N_{SERS}has been normalized for the volume of the hotspot as determined from DDA electric near field contour plots and assuming a self-assembling monolayer of thiolated molecule on the surface of the gold. In this work we used naphthalenethiol which has a molecular footprint of 0.42 nm.[2,155] For the surface averaged calculation, instead of $S_{hotspot}$ the total surface area of the nanoparticle, $S_{average}$, is used.

$$S_{hotspot} = \pi {R_{hotspot}}^2$$

$$S_{average} = 2l^2 \sin 60$$

where $\boldsymbol{R_{hotspot}}$ is the radius of the excited hotspot, estimated from DDSCAT calculations of the electric field contour plots, and $\boldsymbol{l}$ is the side length of the prisms. For example, a particle with a hotspot enhancement factor of 10^{10} and a hotspot area that is 1% of the total area of the particle, the surface average enhancement factor would be 10^8. Examples of these calculations are shown in Tables 3, 4 and 5.

TABLE 3: VALUES OF CONSTANTS USED IN ENHANCEMENT FACTOR CALCULATIONS

$S_{lattice}$ (nm^2)	550*590=324500
$S_{average}$ (nm^2)	2*180*155=55800
$S_{hotspot}$ (nm^2)	π(2*2)=12
D_{spot} (nm)	4000
D_{bulk} (nm)	1000000
$\rho N_A/w$	4.42
m	0.42
ρ (g/cm^3)	1.176E-21
N_A	6.02E+23
w (g/mole)	160.24

TABLE 4: CALCULATIONS FOR HOTSPOT NORMALIZED ENHANCEMENT FACTOR

Gap (nm)	I_{SERS}	N_{SERS}	N_{bulk}	I_{bulk}	EF
5	9954	1106	5.55E+13	1600	3.122E+11
10	8179	1106	5.55E+13	1600	2.565E+11
15	5050	1106	5.55E+13	1600	1.584E+11
20	4248	1106	5.55E+13	1600	1.332E+11
25	3610	1106	5.55E+13	1600	1.132E+11

TABLE 5: CALCULATIONS FOR SURFACE AVERAGED ENHANCEMENT FACTOR

Gap (nm)	I_{SERS}	N_{SERS}	N_{bulk}	I_{bulk}	EF
5	9954	5144937	5.55E+13	1600	6.711E+07
10	8179	5144937	5.55E+13	1600	5.514E+07
15	5050	5144937	5.55E+13	1600	3.405E+07
20	4248	5144937	5.55E+13	1600	2.864E+07
25	3610	5144937	5.55E+13	1600	2.434E+07

Smaller gap sizes resulted in higher Raman enhancement for parallel polarization while perpendicular polarization did not show significant change, as shown in Figure 51a. Polarizations parallel to the bowtie axis had higher enhancement factors than perpendicular polarization, shown in Figure 51b.

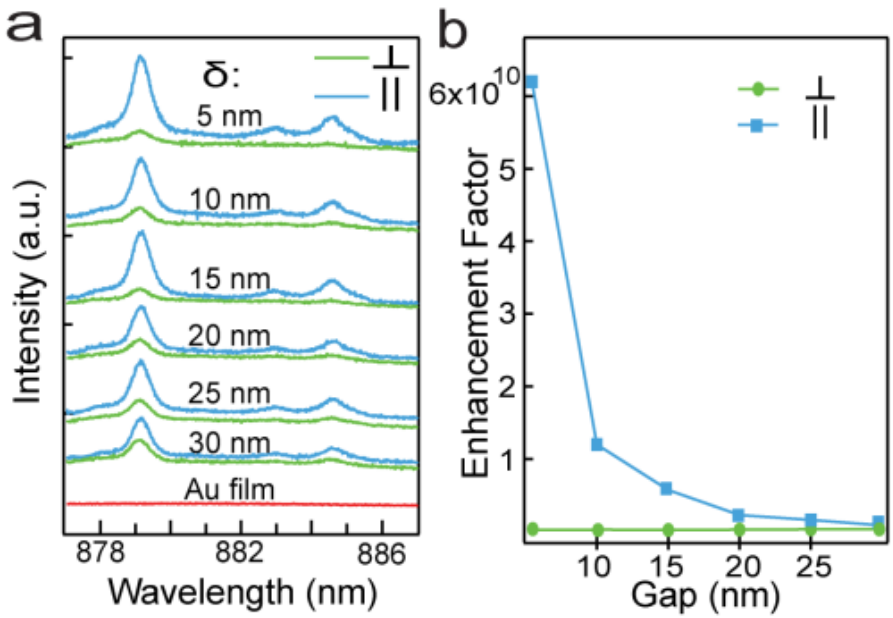

FIGURE 51: EFFECT OF GAP SIZE AND POLARIZATION ON SURFACE ENHANCED RAMAN SCATTERING AND ENHANCEMENT FACTOR

a) Raman spectra and b) enhancement factor of prism dimers with varying gaps between prisms for both polarizations.

The theoretical electric field enhancement was calculated with the use of electric field simulations in DDSCAT using 785 nm excitation, shown in Figure 52. The electric field contour plot simulations for 785 nm excitation show that the hotspot is located in between the prisms for polarization parallel to the bowtie axis and on the outer corners for polarization perpendicular to the bowtie axis, similar to the features of single prisms shown in Figure 53.

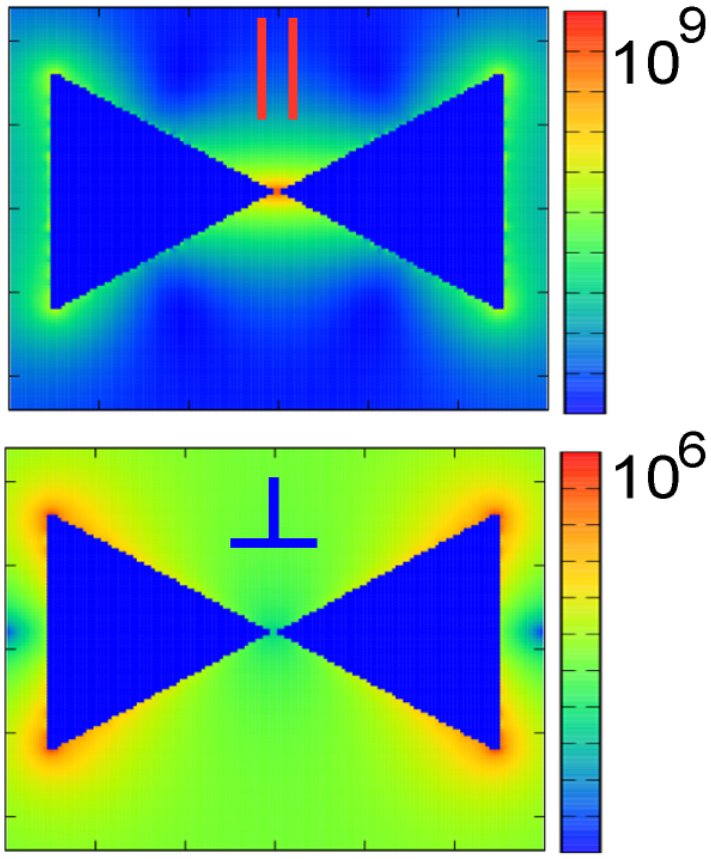

FIGURE 52: EFFECT OF POLARIZATION ON SIMULATED ELECTRIC FIELD CONTOUR PLOTS

Simulated electric field contour plot of longitudinal (top) and transverse (bottom) modes Calculations done using DDSCAT.

The calculated electric field enhancement increases with decreasing gap size for polarization parallel to the bowtie axis, until the limit of the fabrication abilities, which agrees with simulation results and previous studies.[79] The Raman signal was not significantly enhanced by the polarization perpendicular to the antenna axis and did not vary significantly with changing gap size.

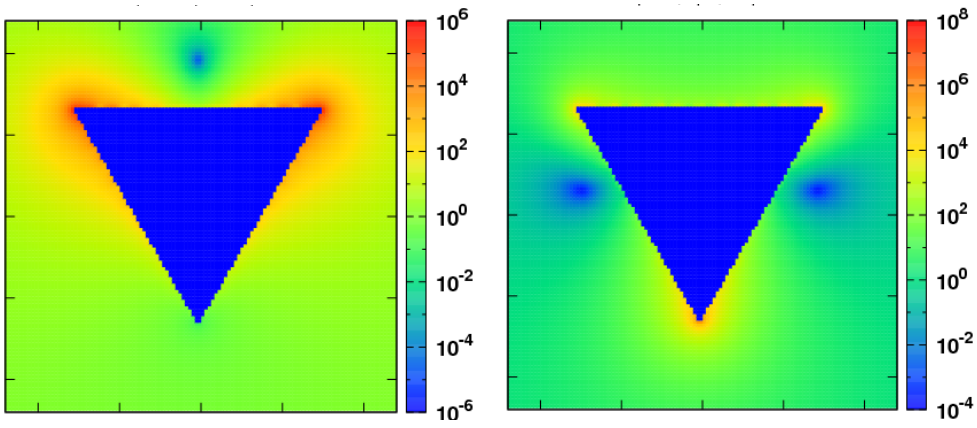

FIGURE 53: ELECTRIC FIELD SIMULATION CONTOUR PLOTS OF SINGLE PRISMS

Electric field contour plots of 150 nm side length prism, calculated using DDSCAT, for 785 nm excitation wavelength, with polarizations parallel (left) and perpendicular (right) to the top edge of prism.

The electric field was simulated and experimentally explored using SERS and DDA electric field calculations for bowtie nanoantennae with varying prism size. An excitation wavelength of 785 nm was used for all simulations and experimental measurements. The prism size was varied from 120 nm to 180 nm for gap spacing from 4 nm to 30 nm. The electric field intensity increased with decreasing gap for all prism sizes in both experiment and simulation, as shown in Figure 54. The calculated electric field peaked at for prisms with 140 nm side length and 4 nm gap. The Raman enhancement factor was highest for 160 nm prism size and 4 nm gap. The discrepancy between simulation and experiment for optimal prism size for 785 nm excitation may be due to the improved prism shape and corner sharpness that results from larger prism fabrication. If so, then improvements in fabrication technique may improve the experimental enhancement of the smaller prisms and the data might more closely follow the trend predicted in simulation. It is noteworthy that 785 nm excitation is off resonance, in varying degrees for different geometries. It would be of interest to explore on-resonance excitations in order to more carefully study the plasmon modes and fully exploit the potential of bowtie nanoantennae as a SERS biosensing substrate.

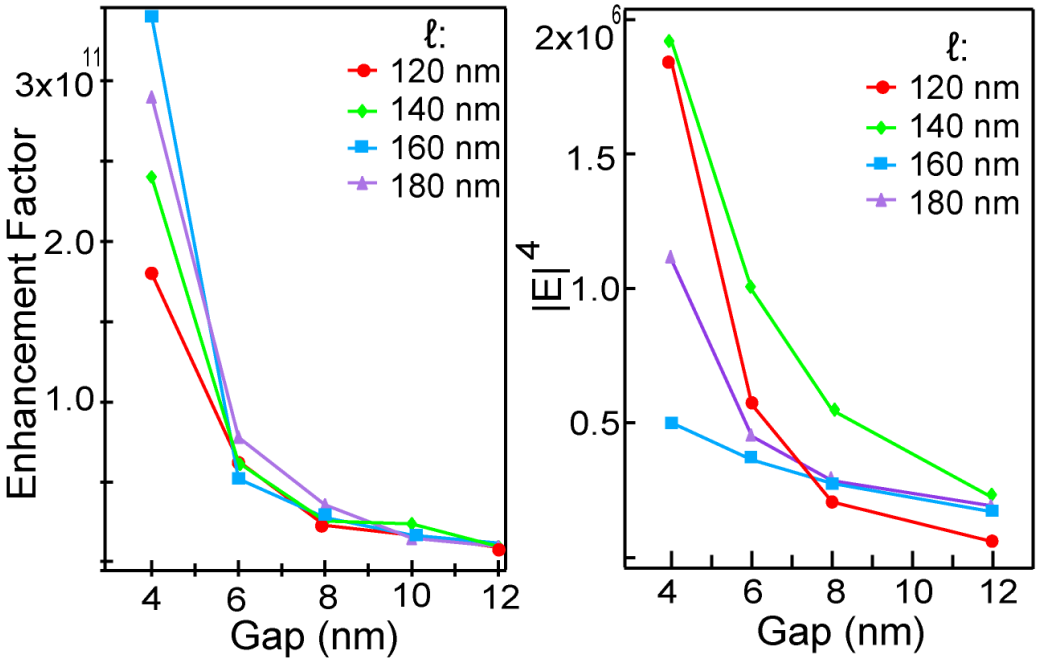

FIGURE 54: EFFECT OF PRISM SIZE ON ENHANCEMNT FACTOR AND CALCULATED ELECTRIC FIELD INTENSITY

(left) Enhancement factor and (right) averaged $|E|^4$ of prism dimers with varying gaps between prisms and varying prism side lengths. Calculations done using DDSCAT.

It was of interest to observe the effect of the radius of curvature (ROC) of the corners of the prisms of a bowtie nanoantenna on optical properties and electric field. By holding all other geometrical parameters constant and varying the fabrication recipe, specifically increasing the dosage of the electron beam, the ROC was controlled and its effects on the electrical and optical properties were observed. The optical transmission spectra were taken of bowtie nanoantennae with both sharp and rounded corners for varying gap spacing between prisms. Both modes, due to polarization perpendicular and parallel to the bowtie axis, redshifted for increasing sharpness of the prism corners. Raman spectra were taken for bowtie nanoantennae with varying ROC and gap size. The Raman enhancement factor increased with decreasing gap size for both round and sharp bowties, but the increase was more dramatic for the sharp bowties, as shown in Figure 55. This agrees with the school of thought that electrons are more fully confined in the smaller ROC corners and would induce more electric field enhancement. It would be of interest to observe more ROCs through controlled fabrication, ranging from circular dimers to prism dimers.

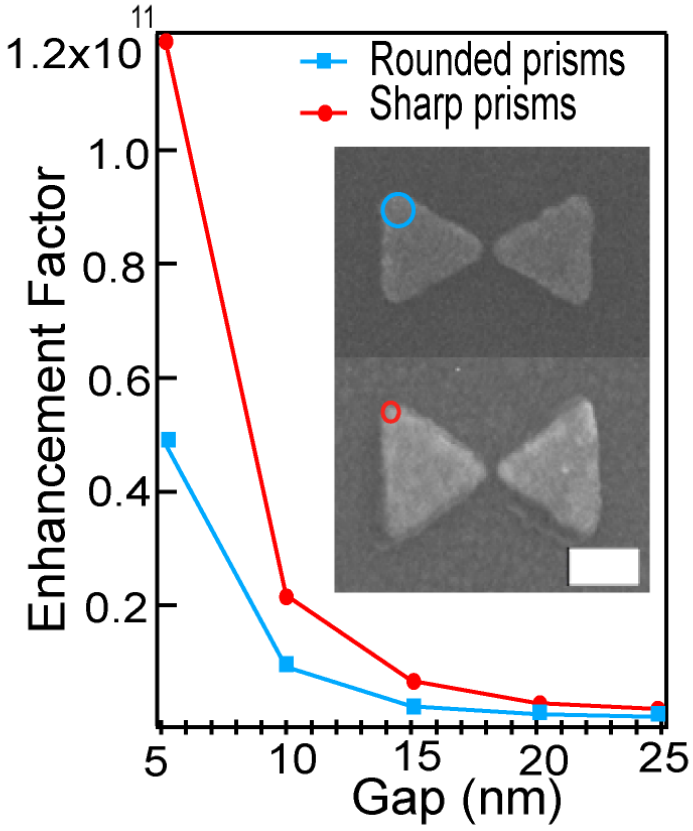

FIGURE 55: EFFECT OF RADIUS OF CURVATURE OOF PRISM CORNERS ON ENHANCEMENT FACTOR

Enhancement factor of prism dimers with varying gaps between prisms for two different ROCs. Inset shows SEM image of round and sharp prism dimers. Scale bar is 100 nm.

6.4 CONCLUSIONS

In order to optimize bowtie nanoantennae for potential SERS biosensing, it was necessary to characterize the effect of gap, prism size, and ROC. We have been able to fabricate very small gaps in bowtie nanoantennae, in the sub-5 nm range, and have confirmed the continuation of trends found in previous work. The results on the variation of bowtie prism size were found to agree with the studies on varying the size of individual prisms. We have found evidence that the radius of curvature has a significant impact on the LSPR and electric field enhancement. We found that simulated predictions of the effects of geometry can be experimentally confirmed for the effect of gap and prism size on the SPR and the EF enhancement. The SPR peak corresponding to the parallel polarization was found to red shift with decreasing gap size while the peak corresponding to the perpendicular polarization remained fixed. The Raman signal enhancement was

found to increase with decreasing gap for parallel polarization but did not change significantly for perpendicular polarization. The two modes, for polarization perpendicular and parallel to the bowtie axis, redshifted for increasing prism size. The trend of increasing enhancement with decreasing gap size was true for all prism sizes. As the ROC decreases and the prism corners become sharper both resonance peaks red shift and the Raman signal enhancement increases. This implies that the electric field enhancement is higher for sharper cornered bowties.

6.5 PERSPECTIVES

The increased enhancement resulting from decreasing gap sizes and ROC can be exploited for making highly sensitive SERS-based biosensors. With signal-to-noise ratios increased by factors around one million, the presence of a SERS biomarker will be considerably easier than Raman spectroscopy. It will be possible to detect lower amounts of biomarker, perform detection measurements in less time, and require less direct fluid sample from patients. The high enhancement factor of bowtie nanoantennae would make conformational studies of DNA possible. The Raman signature of DNA with varying secondary structure, such as duplex and quadruplex, should be detectable with a sensitive SERS substrate.

7 CHAPTER 7: GENERAL CONCLUSIONS AND PERSPECTIVES

During the course of this thesis work plasmonic nanostructures were rigorously tested through simulation and experiment to determine their potential for use as proteomic biosensors. Nanorod arrays with sharp photonic resonances were tuned and used for highly sensitive, localized surface plasmon resonance (LSPR)-based sensing. The use of a photosensitive polymer allowed the imaging of the electric near-field of bowtie nanoantennae, including modes in the near infrared. Bowtie nanoantennae were also tested for electric field enhancement for future use as proteomic surface enhanced Raman scattering (SERS)-based biosensors.

7.1 NANOROD ARRAYS FOR LSPR-BASED BIOSENSING

Rectangular arrays of gold nanorods were studied for their potential as LSPR-based biosensors. Nanorod arrays exhibited very sharp resonances, which demonstrated a high figure of merit (FOM) and sensitivity to changes in refractive index. A high FOM is an excellent indicator of potential analyte binding based biosensing capabilities. The molecular binding of biotinylated-DNA to streptavidin was detected through the LSPR shift at very low concentrations.

The resonances of nanorod arrays were found to be highly tunable through adjusting geometrical parameters, such as nanorod aspect ratio and array periodicity. Increasing the width or decreasing the length both showed a red shift of the resonance, reflecting the fact that the particles are becoming more sphere-like. The one-dimensional nanorod array simulations showed a red shift for decreasing transverse periodicity and a blue shift for decreasing longitudinal periodicity. Two-dimensional arrays showed a red shift for decreasing longitudinal periodicity and no shift for decreasing transverse periodicity.

Some arrays had very sharp resonances with narrow full width half maximum (FWHM). One such array, with 300×500 nm periodicity, had an experimental sensitivity to changes in the refractive index of dielectric media of 310 nm/riu. This high sensitivity and narrow FWHM resulted in an excellent figure of merit of 3.6.

In order to test the sensitivity of the resonance position to binding events, a streptavidin biotin binding assay was performed. Using this method, low concentrations of DNA molecules were detected, down to 0.1 aM (~3 molecules in 50 μL).

The nanorod arrays developed promise huge capabilities in molecular binding studies and single molecule detection, with enormous applications in disease diagnosis. By observing the LSPR shift of nanorod arrays, it was possible to detect the single nucleotide polymorphisms (SNP) of DNA. This was done by comparing the spectra of an array of nanorods coated in a monolayer of healthy DNA to that of SNP mutated DNA that has been cleaved through nuclease interaction.

Additionally, the binding of analytes holds great promise for LSPR-based biosensing. For very small amounts of analyte present, there should be a measurable LSPR shift for a sensitive substrate, like the nanorod arrays developed in this work.

7.2 Photochemical Near-Field Imaging

A photosensitive polymer was used to image the modes of bowtie nanoantennae for a range of excitation wavelengths. A photochemical near-field imaging recipe was developed for a range of excitation wavelengths, including wavelengths outside the absorption band of the azobenzene dye, dispersed red 1 (DR1). The existing technique for photochemical imaging was adapted to use two-photon absorption of DR1 to induce molecular motion for wavelengths outside the absorption band of DR1. Using one- and two-photon absorption of DR1, the experimental near-field features observed for off-resonance, longitudinal and transverse modes were correlated to the electric field features simulated by discrete dipole approximation (DDA).

Normal, one-photon absorption of DR1 polymer was used to image the off-resonance mode of bowtie nanoantennae at 568 nm excitation. The electric near field resulting from off-resonance excitation exhibits mild localization along the edges of the prisms, in both photochemical near field imaging and discrete dipole approximation electric field simulations.

A recipe was developed to accomplish near-field imaging using two-photon absorption based molecular motion of DR1. The electric field gradient of a focalized laser spot was imaged in photosensitive polymer films. The recipe was adapted to excite in-resonance modes in bowtie nanoantennae. The longitudinal mode exhibited the central hotspot just as in simulations of the electric field. The transverse mode also agrees well with simulation, showing the hotspots in the outer corners of the bowtie.

As predicted by simulation, the experimental near-field feature for the longitudinal mode of bowtie nanoantennae, the central hotspot, dissipates with increasing gap size.

The near-field technique developed can be used for imaging a wide variety of nanostructures. Using single and two-photon absorption of DR1 polymer the modes of plasmonic nanostructures within the range of 400 to 1000 nm can be imaged. There are many interesting nanostructures, such as metamaterials, which simulations have shown to have complex near field features. Using the molecular motion of photosensitive polymers, it would be possible to have experimental evidence of these complex features.

Furthermore, time resolved studies could illuminate the changes in the near electric field of nanostructures over time. Potentially, using a series of very short exposures, the stages of near field excitation could be imaged using atomic force microscopy, since the polymer is stable when not in an electric field gradient.

7.3 Bowtie Nanoantennae for SERS-Based Biosensing

Bowtie nanoantennae were studied for their potential as SERS-based biosensors. Simulated predictions of the effects of geometry were experimentally confirmed for the effect of gap, radius of curvature (ROC), and prism size on the LSPR and the electric field enhancement. Bowties with very small gaps and sharp corners exhibited SERS enhancement factors up to 10^{11}.

Bowtie nanoantennae with varying gap sizes, including in the sub-5 nm range, have been fabricated using electron beam lithography (EBL) and characterized for the effect of gap spacing on LSPR and electric field. The LSPR peak corresponding to the parallel polarization was found to red shift with decreasing gap size while the peak corresponding to the perpendicular polarization remained fixed. The Raman signal enhancement was found to increase with decreasing gap size for parallel polarization but did not change significantly for perpendicular polarization.

The results on the variation of bowtie prism size were found to agree with the studies on varying the size of individual prisms. The two modes, for polarization perpendicular to and parallel to the bowtie axis, red shifted for increasing prism size. The trend of increasing enhancement with decreasing gap size was true for all prism sizes.

The radius of curvature of bowtie corners has a significant impact on the LSPR and electric field enhancement. As the ROC decreases and the prism corners become sharper both resonance peaks red shift and the Raman signal enhancement increases. This implies that the electric field enhancement is higher for sharper cornered bowties.

The increased enhancement resulting from decreasing gap sizes and ROC can be exploited for making highly sensitive SERS-based biosensors. With signal-to-noise ratios increased by factors around one million, the presence of a SERS biomarker will be considerably easier than Raman spectroscopy. It will be possible to detect lower amounts of biomarkers, which means even in the early stages of disease the low quantity of biomarkers in patient samples will be enough. This also implies a requirement for less direct fluid sample from patients, for instance a drop rather than a pint of blood, which has a great impact on patient health and morale.

Furthermore, the high enhancement factor of bowtie nanoantennae makes conformational studies of DNA possible. The Raman signature of DNA with varying secondary structure, such as duplex and quadruplex, should be detectable with a sensitive SERS substrate.

The high FOM of nanorod arrays and high SERS enhancement factor of bowtie nanoantennae have great potential for highly sensitive biosensing. Using the sensing platforms discussed in this thesis work, proteomic biosensors will be able to detect lower concentrations of analyte in patient samples. The ability to detect low concentrations allows for early-stage disease diagnostics, which greatly increases the chances of successful treatment.

ABBREVIATIONS

AFM	Atomic Force Microscopy
DDA	Discrete Dipole Approximation
DDSCAT	Discrete Dipole Scattering
DNA	Deoxyribonucleic acid
DR1	Dispersed Red 1
DR1MA	Dispersed Red 1 methyl methacrylate
EBL	Electron Beam Lithography
EF	Enhancement Factor
IPA	Isopropyl Alcohol
IR	Infrared
ITO	Indium Tin Oxide
LSPR	Localized Surface Plasmon Resonance
MMA	Methyl methacrylate
NIR	Near Infrared
NSOM	Near Field Scanning Optical Microscopy
PMMA	Poly (methyl methacrylate)
PSA	Prostate Specific Antigen
RG6	Rhodamine G6
RI	Refractive Index
ROC	Radius Of Curvature
RT	Room Temperature
RTA	Rapid Thermal Annealing
SEM	Scanning Electron Microscope
SERS	Surface Enhance Raman Scattering

SNP	Single Nucleotide Polymorphism
SPR	Surface Plasmon Resonance

REFERENCES

1. Wulfkuhle, J. D.; Liotta, L. A.; Petricoin, E. F., Proteomic applications for the early detection of cancer. *Nature Reviews Cancer* **2003,** *3* (4), 267-275.
2. Anker, J. N.; Hall, W. P.; Lyandres, O.; Shah, N. C.; Zhao, J.; Van Duyne, R. P., Biosensing with plasmonic nanosensors. *Nat Mater* **2008,** *7* (6), 442-453.
3. Moskovits, M., Surface-Enhanced Spectroscopy. *Reviews of Modern Physics* **1985,** *57* (3), 783-826.
4. Parkin, D. M.; Bray, F.; Ferlay, J.; Pisani, P., Global cancer statistics, 2002. *Ca-a Cancer Journal for Clinicians* **2005,** *55* (2), 74-108.
5. Barnes, W. L.; Dereux, A.; Ebbesen, T. W., Surface plasmon subwavelength optics. *Nature* **2003,** *424* (6950), 824-830.
6. Savage, G., *Glass of the world*. Galahad Books: New York, 1975; p 128 p.
7. Thiessen, P. A., Connections of shape and characteristics of colloidal mixtures. *Kolloid-Zeitschrift* **1942,** *101* (3), 241-248.
8. Eustis, S.; El-Sayed, M. A., Why gold nanoparticles are more precious than pretty gold: Noble metal surface plasmon resonance and its enhancement of the radiative and nonradiative properties of nanocrystals of different shapes. *Chemical Society Reviews* **2006,** *35* (3), 209-217.
9. Chalabi, H.; Brongersma, M. L., Plasmonics Harvest Season for Hot Electrons. *Nature Nanotechnology* **2013,** *8* (4), 229-230.
10. Brockman, J. M.; Nelson, B. P.; Corn, R. M., Surface plasmon resonance imaging measurements of ultrathin organic films. *Annu Rev Phys Chem* **2000,** *51*, 41-63.
11. Knoll, W., Interfaces and thin films as seen by bound electromagnetic waves. *Annu Rev Phys Chem* **1998,** *49*, 569-638.
12. Haes, A. J.; Haynes, C. L.; McFarland, A. D.; Schatz, G. C.; Van Duyne, R. R.; Zou, S. L., Plasmonic materials for surface-enhanced sensing and spectroscopy. *Mrs Bulletin* **2005,** *30* (5), 368-375.
13. Kelly, K. L.; Coronado, E.; Zhao, L. L.; Schatz, G. C., The optical properties of metal nanoparticles: The influence of size, shape, and dielectric environment. *Journal of Physical Chemistry B* **2003,** *107* (3), 668-677.
14. Jensen, T. R.; Duval, M. L.; Kelly, K. L.; Lazarides, A. A.; Schatz, G. C.; Van Duyne, R. P., Nanosphere lithography: Effect of the external dielectric medium on the surface plasmon resonance spectrum of a periodic array of sliver nanoparticles. *Journal of Physical Chemistry B* **1999,** *103* (45), 9846-9853.
15. Willets, K. A.; Van Duyne, R. P., Localized surface plasmon resonance spectroscopy and sensing. *Annu Rev Phys Chem* **2007,** *58*, 267-97.
16. Mulvaney, P., Surface plasmon spectroscopy of nanosized metal particles. *Langmuir* **1996,** *12* (3), 788-800.
17. Brongersma, M. L.; Shalaev, V. M., Applied Physics the Case for Plasmonics. *Science* **2010,** *328* (5977), 440-441.
18. Fleischm.M; Hendra, P. J.; Mcquilla.Aj, Raman-Spectra of Pyridine Adsorbed at a Silver Electrode. *Chemical Physics Letters* **1974,** *26* (2), 163-166.
19. Jeanmaire, D. L.; Vanduyne, R. P., Surface Raman Spectroelectrochemistry .1. Heterocyclic, Aromatic, and Aliphatic-Amines Adsorbed on Anodized Silver Electrode. *Journal of Electroanalytical Chemistry* **1977,** *84* (1), 1-20.
20. Moskovits, M., Surface-Roughness and Enhanced Intensity of Raman-Scattering by Molecules Adsorbed on Metals. *Journal of Chemical Physics* **1978,** *69* (9), 4159-4161.
21. Takahara, J.; Yamagishi, S.; Taki, H.; Morimoto, A.; Kobayashi, T., Guiding of a one-dimensional optical beam with nanometer diameter. *Optics Letters* **1997,** *22* (7), 475-477.
22. Ebbesen, T. W.; Lezec, H. J.; Ghaemi, H. F.; Thio, T.; Wolff, P. A., Extraordinary optical transmission through sub-wavelength hole arrays. *Nature* **1998,** *391* (6668), 667-669.
23. Pendry, J. B., Negative refraction makes a perfect lens. *Physical Review Letters* **2000,** *85* (18), 3966-3969.
24. Shalaev, V. M., Transforming light. *Science* **2008,** *322* (5900), 384-386.

25. Stockman, M. I., The spaser as a nanoscale quantum generator and ultrafast amplifier. *Journal of Optics* **2010,** *12* (2).
26. Eustis, S.; El-Sayed, M. A., Determination of the aspect ratio statistical distribution of gold nanorods in solution from a theoretical fit of the observed inhomogeneously broadened longitudinal plasmon resonance absorption spectrum. *Journal of Applied Physics* **2006,** *100* (4).
27. Jensen, T. R.; Malinsky, M. D.; Haynes, C. L.; Van Duyne, R. P., Nanosphere lithography: Tunable localized surface plasmon resonance spectra of silver nanoparticles. *Journal of Physical Chemistry B* **2000,** *104* (45), 10549-10556.
28. Hicks, E. M.; Zou, S. L.; Schatz, G. C.; Spears, K. G.; Van Duyne, R. P.; Gunnarsson, L.; Rindzevicius, T.; Kasemo, B.; Kall, M., Controlling plasmon line shapes through diffractive coupling in linear arrays of cylindrical nanoparticles fabricated by electron beam lithography. *Nano Lett* **2005,** *5* (6), 1065-1070.
29. McFarland, A. D.; Young, M. A.; Dieringer, J. A.; Van Duyne, R. P., Wavelength-scanned surface-enhanced Raman excitation spectroscopy. *J Phys Chem B* **2005,** *109* (22), 11279-85.
30. Halas, N. J.; Lal, S.; Chang, W. S.; Link, S.; Nordlander, P., Plasmons in Strongly Coupled Metallic Nanostructures. *Chemical Reviews* **2011,** *111* (6), 3913-3961.
31. Sherry, L. J.; Chang, S. H.; Schatz, G. C.; Van Duyne, R. P.; Wiley, B. J.; Xia, Y. N., Localized surface plasmon resonance spectroscopy of single silver nanocubes. *Nano Lett* **2005,** *5* (10), 2034-2038.
32. Yeom, S. H.; Han, M. E.; Kang, B. H.; Kim, K. J.; Yuan, H.; Eum, N. S.; Kang, S. W., Enhancement of the sensitivity of LSPR-based CRP immunosensors by Au nanoparticle antibody conjugation. *Sensors and Actuators B-Chemical* **2013,** *177*, 376-383.
33. Jeong, H. H.; Erdene, N.; Park, J. H.; Jeong, D. H.; Lee, H. Y.; Lee, S. K., Real-time label-free immunoassay of interferon-gamma and prostate-specific antigen using a Fiber-Optic Localized Surface Plasmon Resonance sensor. *Biosens Bioelectron* **2013,** *39* (1), 346-351.
34. Willets, K. A.; Van Duyne, R. P., Localized surface plasmon resonance spectroscopy and sensing. *Annual Review of Physical Chemistry* **2007,** *58*, 267-297.
35. Yonzon, C. R.; Stuart, D. A.; Zhang, X. Y.; McFarland, A. D.; Haynes, C. L.; Van Duyne, R. P., Towards advanced chemical and biological nanosensors - An overview. *Talanta* **2005,** *67* (3), 438-448.
36. Haes, A. J.; Chang, L.; Klein, W. L.; Van Duyne, R. P., Detection of a biomarker for Alzheimer's disease from synthetic and clinical samples using a nanoscale optical biosensor. *Journal of the American Chemical Society* **2005,** *127* (7), 2264-2271.
37. Dahlin, A. B.; Tegenfeldt, J. O.; Hook, F., Improving the instrumental resolution of sensors based on localized surface plasmon resonance. *Analytical Chemistry* **2006,** *78* (13), 4416-4423.
38. Chen, S.; Svedendahl, M.; Van Duyne, R. P.; Kall, M., Plasmon-Enhanced Colorimetric ELISA with Single Molecule Sensitivity. *Nano Lett* **2011,** *11* (4), 1826-1830.
39. Mayer, K. M.; Hafner, J. H., Localized Surface Plasmon Resonance Sensors. *Chemical Reviews* **2011,** *111* (6), 3828-3857.
40. Stewart, M. E.; Anderton, C. R.; Thompson, L. B.; Maria, J.; Gray, S. K.; Rogers, J. A.; Nuzzo, R. G., Nanostructured plasmonic sensors. *Chemical Reviews* **2008,** *108* (2), 494-521.
41. Homola, J., Surface plasmon resonance sensors for detection of chemical and biological species. *Chemical Reviews* **2008,** *108* (2), 462-493.
42. Fong, K. E.; Yung, L. Y. L., Localized surface plasmon resonance: a unique property of plasmonic nanoparticles for nucleic acid detection. *Nanoscale* **2013,** *5* (24), 12043-12071.
43. Guo, L. H.; Kim, D. H., LSPR biomolecular assay with high sensitivity induced by aptamer-antigen-antibody sandwich complex. *Biosens Bioelectron* **2012,** *31* (1), 567-570.
44. Tang, L.; Casas, J.; Venkataramasubramani, M., Magnetic Nanoparticle Mediated Enhancement of Localized Surface Plasmon Resonance for Ultrasensitive Bioanalytical Assay in Human Blood Plasma. *Analytical Chemistry* **2013,** *85* (3), 1431-1439.
45. Jackson, J. D., *Classical electrodynamics*. Wiley: New York,, 1962; p 641 p.
46. Girard, C.; Joachim, C.; Gauthier, S., The physics of the near-field. *Reports on Progress in Physics* **2000,** *63* (6), 893-938.
47. Hsu, J. W. P., Near-field scanning optical microscopy studies of electronic and photonic materials and devices. *Materials Science & Engineering R-Reports* **2001,** *33* (1), 1-50.

48. Betzig, E.; Lewis, A.; Harootunian, A.; Isaacson, M.; Kratschmer, E., Near-Field Scanning Optical Microscopy (Nsom) - Development and Biophysical Applications. *Biophysical Journal* **1986,** *49* (1), 269-279.
49. Hecht, B.; Sick, B.; Wild, U. P.; Deckert, V.; Zenobi, R.; Martin, O. J. F.; Pohl, D. W., Scanning near-field optical microscopy with aperture probes: Fundamentals and applications. *Journal of Chemical Physics* **2000,** *112* (18), 7761-7774.
50. Plain, J.; Juan, M. L.; Bachelot, R.; Royer, P.; Gray, S. K.; Wiederrecht, G. P., Self-Consistent Model of Light-Induced Molecular Motion Around Metallic Nanostructures. *Journal of Physical Chemistry Letters* **2010,** *1* (15), 2228-2232.
51. Plain, J.; Juan, M. L.; Bachelot, R.; Vial, A.; Royer, P.; Gray, S. K.; Montgomery, J. M.; Wiederrecht, G. P., Plasmonic Electromagnetic Hot Spots Temporally Addressed by Photoinduced Molecular Displacement. *Journal of Physical Chemistry A* **2009,** *113* (16), 4647-4651.
52. Haggui, M.; Dridi, M.; Plain, J.; Marguet, S.; Perez, H.; Schatz, G. C.; Wiederrecht, G. P.; Gray, S. K.; Bachelot, R., Near-field optical properties of Au-Nanocubes: confinement of hot and cold spots. *Nanophotonics Iv* **2012,** *8424*.
53. Bachelot, R.; Juan, M. L.; Plain, J.; Royer, P.; Gray, S. K.; Wiederrecht, G. P., Stochastic model for photoinduced surface relief grating formation through molecular transport in polymer films. *Applied Physics Letters* **2008,** *93* (15).
54. Juan, M. L.; Plain, J.; Bachelot, R.; Royer, P.; Gray, S. K.; Wiederrecht, G. P., Multiscale Model for Photoinduced Molecular Motion in Azo Polymers. *ACS Nano* **2009,** *3* (6), 1573-1579.
55. Juan, M. L.; Plain, J.; Bachelot, R.; Vial, A.; Royer, P.; Gray, S. K.; Montgomery, J. M.; Wiederrecht, G. P., Plasmonic Electromagnetic Hot Spots Temporally Addressed by Photoinduced Molecular Displacement. *Journal of Physical Chemistry A* **2009,** *113* (16), 4647-4651.
56. Halas, N. J.; Lal, S.; Link, S.; Chang, W. S.; Natelson, D.; Hafner, J. H.; Nordlander, P., A Plethora of Plasmonics from the Laboratory for Nanophotonics at Rice University. *Advanced Materials* **2012,** *24* (36), 4842-4877.
57. McCreery, R. L., *Raman spectroscopy for chemical analysis*. John Wiley & Sons: New York, 2000; p xxiv, 420 p.
58. Kneipp, K.; Kneipp, H.; I, I.; Dasari, R. R.; Feld, M. S., Ultrasensitive chemical analysis by Raman spectroscopy. *Chemical Reviews* **1999,** *99* (10), 2957-+.
59. Albrecht, M. G.; Creighton, J. A., Anomalously Intense Raman-Spectra of Pyridine at a Silver Electrode. *Journal of the American Chemical Society* **1977,** *99* (15), 5215-5217.
60. Otto, A., Surface-Enhanced Raman-Scattering - Classical and Chemical Origins. *Topics in Applied Physics* **1984,** *54*, 289-418.
61. Purcell, E. M.; Pennypac.Cr, SCATTERING AND ABSORPTION OF LIGHT BY NONSPHERICAL DIELECTRIC GRAINS. *Astrophysical Journal* **1973,** *186* (2), 705-714.
62. Devoe, H., OPTICAL PROPERTIES OF MOLECULAR AGGREGATES .I. CLASSICAL MODEL OF ELECTRONIC ABSORPTION + REFRACTION. *Journal of Chemical Physics* **1964,** *41* (2), 393-&.
63. Draine, B. T., The Discrete-Dipole Approximation and Its Application to Interstellar Graphite Grains. *Astrophysical Journal* **1988,** *333* (2), 848-872.
64. Clausius, R. J. E., *Die mechanische Behandlung der Electricität*. F. Vieweg: Braunschweig,, 1879; p xii, 352 p.
65. Clausius, R. J. E., *Théorie mécanique de la chaleur*. E. Lacroix: Paris,, 1868.
66. Clausius, R. J. E., *Die Potentialfunction und das Potential; ein Beitrag zur mathematischen Physik*. 2. verm. ed.; J. A. Barth: Leipzig,, 1867; p vi, 119 p.
67. Benedetti, S. d.; Ferrucci, M.; Mossotti, O. F., *Ottaviano Fabrizio Mossotti*. Tipografia Nistri: Pisa,, 1867; p 51 p.
68. Pillori, P.; Gazzeri, G.; Mossotti, O. F., *Osservazioni dell'abate Pietro Pillori al cav. professore Giuseppe Gazzeri in materia dei lavori Galileiani sui satelliti di Giove*. Emidio dall'Olmo: Bologna, 1844; p 48 p.
69. Draine, B. T.; Flatau, P. J., Discrete-Dipole Approximation for Scattering Calculations. *Journal of the Optical Society of America a-Optics Image Science and Vision* **1994,** *11* (4), 1491-1499.

70. Flatau, P. J.; Stephens, G. L.; Draine, B. T., Light-Scattering by Rectangular Solids in the Discrete-Dipole Approximation - a New Algorithm Exploiting the Block-Toeplitz Structure. *Journal of the Optical Society of America a-Optics Image Science and Vision* **1990,** *7* (4), 593-600.
71. Goodman, J. J.; Draine, B. T.; Flatau, P. J., Application of Fast-Fourier-Transform Techniques to the Discrete-Dipole Approximation. *Optics Letters* **1991,** *16* (15), 1198-1200.
72. Draine, B. T.; Goodman, J., Beyond Clausius-Mossotti - Wave-Propagation on a Polarizable Point Lattice and the Discrete Dipole Approximation. *Astrophysical Journal* **1993,** *405* (2), 685-697.
73. Collinge, M. J.; Draine, B. T., Discrete-dipole approximation with polarizabilities that account for both finite wavelength and target geometry. *Journal of the Optical Society of America a-Optics Image Science and Vision* **2004,** *21* (10), 2023-2028.
74. Draine, B. T.; Flatau, P. J., Discrete-dipole approximation for periodic targets: theory and tests. *Journal of the Optical Society of America a-Optics Image Science and Vision* **2008,** *25* (11), 2693-2703.
75. Choy, T. C., *Effective medium theory : principles and applications*. Clarendon Press ;Oxford University Press: Oxford EnglandNew York, 1999; p xi, 182 p.

76. Granqvist, C. G.; Hunderi, O., CONDUCTIVITY OF INHOMOGENEOUS MATERIALS - EFFECTIVE-MEDIUM THEORY WITH DIPOLE-DIPOLE INTERACTION. *Physical Review B* **1978,** *18* (4), 1554-1561.
77. Bartella, J.; Schroeder, J.; Witting, K., Characterization of ITO- and TiOxNy films by spectroscopic ellipsometry, spectraphotometry and XPS. *Applied Surface Science* **2001,** *179* (1-4), 181-190.
78. Johnson, P. B.; Christy, R. W., OPTICAL CONSTANTS OF NOBLE METALS. *Physical Review B* **1972,** *6* (12), 4370-4379.
79. Hao, E.; Schatz, G. C., Electromagnetic fields around silver nanoparticles and dimers. *Journal of Chemical Physics* **2004,** *120* (1), 357-366.
80. Wang, Y.; Chen, G.; Yang, M.; Silber, G.; Xing, S.; Tan, L. H.; Wang, F.; Feng, Y.; Liu, X.; Li, S.; Chen, H., A systems approach towards the stoichiometry-controlled hetero-assembly of nanoparticles. *Nat Commun* **2010,** *1*, 87.
81. Murphy, C. J.; Sau, T. K.; Gole, A. M.; Orendorff, C. J.; Gao, J.; Gou, L.; Hunyadi, S. E.; Li, T., Anisotropic Metal Nanoparticles: Synthesis, Assembly, and Optical Applications. *The Journal of Physical Chemistry B* **2005,** *109* (29), 13857-13870.
82. Grabar, K. C.; Freeman, R. G.; Hommer, M. B.; Natan, M. J., Preparation and Characterization of Au Colloid Monolayers. *Analytical Chemistry* **1995,** *67* (4), 735-743.
83. Peng, B.; Li, G.; Li, D.; Dodson, S.; Zhang, Q.; Zhang, J.; Lee, Y. H.; Demir, H. V.; Yi Ling, X.; Xiong, Q., Vertically Aligned Gold Nanorod Monolayer on Arbitrary Substrates: Self-Assembly and Femtomolar Detection of Food Contaminants. *ACS Nano* **2013,** *7* (7), 5993-6000.
84. Haynes, C. L.; Van Duyne, R. P., Nanosphere Lithography: A Versatile Nanofabrication Tool for Studies of Size-Dependent Nanoparticle Optics. *The Journal of Physical Chemistry B* **2001,** *105* (24), 5599-5611.
85. Haes, A. J.; Van Duyne, R. P., A Nanoscale Optical Biosensor: Sensitivity and Selectivity of an Approach Based on the Localized Surface Plasmon Resonance Spectroscopy of Triangular Silver Nanoparticles. *Journal of the American Chemical Society* **2002,** *124* (35), 10596-10604.
86. Geissler, M.; Xia, Y. N., Patterning: Principles and some new developments. *Advanced Materials* **2004,** *16* (15), 1249-1269.
87. Rycenga, M.; Cobley, C. M.; Zeng, J.; Li, W. Y.; Moran, C. H.; Zhang, Q.; Qin, D.; Xia, Y. N., Controlling the Synthesis and Assembly of Silver Nanostructures for Plasmonic Applications. *Chemical Reviews* **2011,** *111* (6), 3669-3712.
88. Murray, C. B.; Kagan, C. R.; Bawendi, M. G., Synthesis and characterization of monodisperse nanocrystals and close-packed nanocrystal assemblies. *Annual Review of Materials Science* **2000,** *30*, 545-610.
89. Deckman, H. W.; Dunsmuir, J. H., NATURAL LITHOGRAPHY. *Applied Physics Letters* **1982,** *41* (4), 377-379.

90. Kosiorek, A.; Kandulski, W.; Chudzinski, P.; Kempa, K.; Giersig, M., Shadow nanosphere lithography: Simulation and experiment. *Nano Lett* **2004,** *4* (7), 1359-1363.
91. Hulteen, J. C.; Treichel, D. A.; Smith, M. T.; Duval, M. L.; Jensen, T. R.; Van Duyne, R. P., Nanosphere lithography: Size-tunable silver nanoparticle and surface cluster arrays. *Journal of Physical Chemistry B* **1999,** *103* (19), 3854-3863.
92. Haynes, C. L.; Van Duyne, R. P., Nanosphere lithography: A versatile nanofabrication tool for studies of size-dependent nanoparticle optics. *Journal of Physical Chemistry B* **2001,** *105* (24), 5599-5611.
93. Wallraff, G. M.; Hinsberg, W. D., Lithographic imaging techniques for the formation of nanoscopic features. *Chemical Reviews* **1999,** *99* (7), 1801-1821.
94. Ito, T.; Okazaki, S., Pushing the limits of lithography. *Nature* **2000,** *406* (6799), 1027-1031.
95. Bloomstein, T. M.; Horn, M. W.; Rothschild, M.; Kunz, R. R.; Palmacci, S. T.; Goodman, R. B., Lithography with 157 nm lasers. *Journal of Vacuum Science & Technology B* **1997,** *15* (6), 2112-2116.
96. Hatab, N. A.; Hsueh, C. H.; Gaddis, A. L.; Retterer, S. T.; Li, J. H.; Eres, G.; Zhang, Z. Y.; Gu, B. H., Free-Standing Optical Gold Bowtie Nanoantenna with Variable Gap Size for Enhanced Raman Spectroscopy. *Nano Lett* **2010,** *10* (12), 4952-4955.
97. Cord, B.; Yang, J.; Duan, H. G.; Joy, D. C.; Klingfus, J.; Berggren, K. K., Limiting factors in sub-10 nm scanning-electron-beam lithography. *Journal of Vacuum Science & Technology B* **2009,** *27* (6), 2616-2621.
98. Stewart, M. E.; Anderton, C. R.; Thompson, L. B.; Maria, J.; Gray, S. K.; Rogers, J. A.; Nuzzo, R. G., Nanostructured plasmonic sensors. *Chemical Reviews* **2008,** *108* (2), 494-521.
99. Mayer, K. M.; Lee, S.; Liao, H.; Rostro, B. C.; Fuentes, A.; Scully, P. T.; Nehl, C. L.; Hafner, J. H., A label-free immunoassay based upon localized surface plasmon resonance of gold nanorods. *ACS Nano* **2008,** *2* (4), 687-92.
100. Lassiter, J. B.; Sobhani, H.; Fan, J. A.; Kundu, J.; Capasso, F.; Nordlander, P.; Halas, N. J., Fano resonances in plasmonic nanoclusters: geometrical and chemical tunability. *Nano Lett* **2010,** *10* (8), 3184-9.
101. Zou, S. L.; Schatz, G. C., Coupled plasmonic plasmon/photonic resonance effects in SERS. *Surface-Enhanced Raman Scattering: Physics and Applications* **2006,** *103*, 67-85.
102. Liu, N.; Hentschel, M.; Weiss, T.; Alivisatos, A. P.; Giessen, H., Three-Dimensional Plasmon Rulers. *Science* **2011,** *332* (6036), 1407-1410.
103. Zou, S. L.; Janel, N.; Schatz, G. C., Silver nanoparticle array structures that produce remarkably narrow plasmon lineshapes. *Journal of Chemical Physics* **2004,** *120* (23), 10871-10875.
104. Zou, S. L.; Schatz, G. C., Narrow plasmonic/photonic extinction and scattering line shapes for one and two dimensional silver nanoparticle arrays. *Journal of Chemical Physics* **2004,** *121* (24), 12606-12612.
105. Malynych, S.; Chumanov, G., Light-induced coherent interactions between silver nanoparticles in two-dimensional arrays. *Journal of the American Chemical Society* **2003,** *125* (10), 2896-2898.
106. Ausman, L. K.; Li, S. Z.; Schatz, G. C., Structural Effects in the Electromagnetic Enhancement Mechanism of Surface-Enhanced Raman Scattering: Dipole Reradiation and Rectangular Symmetry Effects for Nanoparticle Arrays. *Journal of Physical Chemistry C* **2012,** *116* (33), 17318-17327.
107. Lombardi, J. R.; Birke, R. L., A Unified View of Surface-Enhanced Raman Scattering. *Accounts of Chemical Research* **2009,** *42* (6), 734-742.
108. Morton, S. M.; Silverstein, D. W.; Jensen, L., Theoretical Studies of Plasmonics using Electronic Structure Methods. *Chemical Reviews* **2011,** *111* (6), 3962-3994.
109. Chen, H. N.; McMahon, J. M.; Ratner, M. A.; Schatz, G. C., Classical Electrodynamics Coupled to Quantum Mechanics for Calculation of Molecular Optical Properties: a RT-TDDFT/FDTD Approach. *Journal of Physical Chemistry C* **2010,** *114* (34), 14384-14392.
110. Zhang, J.; Sun, Y.; Xu, B.; Zhang, H.; Gao, Y.; Zhang, H.; Song, D., A novel surface plasmon resonance biosensor based on graphene oxide decorated with gold nanorod-antibody conjugates for determination of transferrin. *Biosens Bioelectron* **2013,** *45*, 230-6.

111. Morokoshi, S.; Ohhori, K.; Mizukami, K.; Kitano, H., Sensing capabilities of colloidal gold modified with a self-assembled monolayer of a glucose-carrying polymer chain on a glass substrate. *Langmuir* **2004,** *20* (20), 8897-902.
112. Yonzon, C. R.; Jeoung, E.; Zou, S.; Schatz, G. C.; Mrksich, M.; Van Duyne, R. P., A comparative analysis of localized and propagating surface plasmon resonance sensors: the binding of concanavalin a to a monosaccharide functionalized self-assembled monolayer. *Journal of the American Chemical Society* **2004,** *126* (39), 12669-76.
113. Lin, T. J.; Huang, K. T.; Liu, C. Y., Determination of organophosphorous pesticides by a novel biosensor based on localized surface plasmon resonance. *Biosens Bioelectron* **2006,** *22* (4), 513-8.
114. Zijlstra, P.; Paulo, P. M.; Orrit, M., Optical detection of single non-absorbing molecules using the surface plasmon resonance of a gold nanorod. *Nature Nanotechnology* **2012,** *7* (6), 379-82.
115. Hadley, D. W.; Jenkins, J. F.; Dimond, E.; de Carvalho, M.; Kirsch, I.; Palmer, C. G., Colon cancer screening practices after genetic counseling and testing for hereditary nonpolyposis colorectal cancer. *J Clin Oncol* **2004,** *22* (1), 39-44.
116. Jemal, A.; Siegel, R.; Ward, E.; Murray, T.; Xu, J.; Thun, M. J., Cancer statistics, 2007. *CA Cancer J Clin* **2007,** *57* (1), 43-66.
117. Sohn, K. J.; Croxford, R.; Yates, Z.; Lucock, M.; Kim, Y. I., Effect of the methylenetetrahydrofolate reductase C677T polymorphism on chemosensitivity of colon and breast cancer cells to 5-fluorouracil and methotrexate. *Journal of the National Cancer Institute* **2004,** *96* (2), 134-144.
118. Ogino, S.; Kawasaki, T.; Brahmandam, M.; Yan, L. Y.; Cantor, M.; Namgyal, C.; Mino-Kenudson, M.; Lauwers, G. Y.; Loda, M.; Fuchs, C. S., Sensitive Sequencing method for KRAS mutation detection by pyrosequencing. *Journal of Molecular Diagnostics* **2005,** *7* (3), 413-421.
119. Karapetis, C. S.; Khambata-Ford, S.; Jonker, D. J.; O'Callaghan, C. J.; Tu, D.; Tebbutt, N. C.; Simes, R. J.; Chalchal, H.; Shapiro, J. D.; Robitaille, S.; Price, T. J.; Shepherd, L.; Au, H. J.; Langer, C.; Moore, M. J.; Zalcberg, J. R., K-ras mutations and benefit from cetuximab in advanced colorectal cancer. *New England Journal of Medicine* **2008,** *359* (17), 1757-1765.
120. Amado, R. G.; Wolf, M.; Peeters, M.; Van Cutsem, E.; Siena, S.; Freeman, D. J.; Juan, T.; Sikorski, R.; Suggs, S.; Radinsky, R.; Patterson, S. D.; Chang, D. D., Wild-type KRAS is required for panitumumab efficacy in patients with metastatic colorectal cancer. *Journal of Clinical Oncology* **2008,** *26* (10), 1626-1634.
121. Almoguera, C.; Shibata, D.; Forrester, K.; Martin, J.; Arnheim, N.; Perucho, M., MOST HUMAN CARCINOMAS OF THE EXOCRINE PANCREAS CONTAIN MUTANT C-K-RAS GENES. *Cell* **1988,** *53* (4), 549-554.
122. Forrester, K.; Almoguera, C.; Han, K. Y.; Grizzle, W. E.; Perucho, M., DETECTION OF HIGH-INCIDENCE OF K-RAS ONCOGENES DURING HUMAN-COLON TUMORIGENESIS. *Nature* **1987,** *327* (6120), 298-303.
123. Linn, S.; Arber, W., Host specificity of DNA produced by Escherichia coli, X. In vitro restriction of phage fd replicative form. *Proc Natl Acad Sci U S A* **1968,** *59* (4), 1300-6.
124. Arber, W.; Linn, S., DNA modification and restriction. *Annu Rev Biochem* **1969,** *38*, 467-500.
125. Pilato, B.; De Summa, S.; Danza, K.; Papadimitriou, S.; Zaccagna, P.; Paradiso, A.; Tommasi, S., DHPLC/SURVEYOR nuclease: a sensitive, rapid and affordable method to analyze BRCA1 and BRCA2 mutations in breast cancer families. *Mol Biotechnol* **2012,** *52* (1), 8-15.
126. Bannwarth, S.; Procaccio, V.; Paquis-Flucklinger, V., Rapid identification of unknown heteroplasmic mutations across the entire human mitochondrial genome with mismatch-specific Surveyor Nuclease. *Nat Protoc* **2006,** *1* (4), 2037-47.
127. Hoyt, L. F., New table of the refractive index of pure glycerol at 20 degrees C. *Industrial and Engineering Chemistry* **1934,** *26*, 329-332.
128. Guiton, B. S.; Iberi, V.; Li, S. Z.; Leonard, D. N.; Parish, C. M.; Kotula, P. G.; Varela, M.; Schatz, G. C.; Pennycook, S. J.; Camden, J. P., Correlated Optical Measurements and Plasmon Mapping of Silver Nanorods. *Nano Letters* **2011,** *11* (8), 3482-3488.
129. Gilbert, Y.; Bachelot, R.; Vial, A.; Lerondel, G.; Royer, P.; Bouhelier, A.; Wiederrecht, G. P., Photoresponsive polymers for topographic simulation of the optical near-field of a

nanometer sized gold tip in a highly focused laser beam. *Optics Express* **2005,** *13* (10), 3619-3624.
130. Hubert, C.; Rumyantseva, A.; Lerondel, G.; Grand, J.; Kostcheev, S.; Billot, L.; Vial, A.; Bachelot, R.; Royer, P.; Chang, S. H.; Gray, S. K.; Wiederrecht, G. P.; Schatz, G. C., Near-field photochemical imaging of noble metal nanostructures. *Nano Lett* **2005,** *5* (4), 615-619.
131. Wiederrecht, G. P.; Wurtz, G. A.; Hranisavljevic, J., Near-field scanning optical microscopy of metal nanoparticles and nanoscale heterostructures. *Abstracts of Papers of the American Chemical Society* **2005,** *229*, U865-U865.
132. Hubert, C.; Bachelot, R.; Plain, J.; Kostcheev, S.; Lerondel, G.; Juan, M.; Royer, P.; Zou, S. L.; Schatz, G. C.; Wiederrecht, G. P.; Gray, S. K., Near-field polarization effects in molecular-motion-induced photochemical imaging. *Journal of Physical Chemistry C* **2008,** *112* (11), 4111-4116.
133. Plain, J.; Juan, M. L.; Bachelot, R.; Royer, P.; Gray, S. K.; Wiederrecht, G. P., Multiscale Model for Photoinduced Molecular Motion in Azo Polymers. *ACS Nano* **2009,** *3* (6), 1573-1579.
134. Haggui, M.; Dridi, M.; Plain, J.; Marguet, S.; Perez, H.; Schatz, G. C.; Wiederrecht, G. P.; Gray, S. K.; Bachelot, R., Spatial Confinement of Electromagnetic Hot and Cold Spots in Gold Nanocubes. *ACS Nano* **2012,** *6* (2), 1299-1307.
135. Qian, X. M.; Peng, X. H.; Ansari, D. O.; Yin-Goen, Q.; Chen, G. Z.; Shin, D. M.; Yang, L.; Young, A. N.; Wang, M. D.; Nie, S. M., In vivo tumor targeting and spectroscopic detection with surface-enhanced Raman nanoparticle tags. *Nature Biotechnology* **2008,** *26* (1), 83-90.
136. Boisselier, E.; Astruc, D., Gold nanoparticles in nanomedicine: preparations, imaging, diagnostics, therapies and toxicity. *Chemical Society Reviews* **2009,** *38* (6), 1759-1782.
137. Liu, Z.; Cai, W. B.; He, L. N.; Nakayama, N.; Chen, K.; Sun, X. M.; Chen, X. Y.; Dai, H. J., In vivo biodistribution and highly efficient tumour targeting of carbon nanotubes in mice. *Nature Nanotechnology* **2007,** *2* (1), 47-52.
138. Grubisha, D. S.; Lipert, R. J.; Park, H. Y.; Driskell, J.; Porter, M. D., Femtomolar detection of prostate-specific antigen: An immunoassay based on surface-enhanced Raman scattering and immunogold labels. *Analytical Chemistry* **2003,** *75* (21), 5936-5943.
139. Huang, X. H.; Jain, P. K.; El-Sayed, I. H.; El-Sayed, M. A., Gold nanoparticles: interesting optical properties and recent applications in cancer diagnostic and therapy. *Nanomedicine* **2007,** *2* (5), 681-693.
140. Qian, X. M.; Nie, S. M., Single-molecule and single-nanoparticle SERS: from fundamental mechanisms to biomedical applications. *Chemical Society Reviews* **2008,** *37* (5), 912-920.
141. Miller, S. K.; Baiker, A.; Meier, M.; Wokaun, A., Surface-Enhanced Raman-Scattering and the Preparation of Copper Substrates for Catalytic Studies. *Journal of the Chemical Society-Faraday Transactions I* **1984,** *80*, 1305-&.
142. Davies, J. P.; Pachuta, S. J.; Cooks, R. G.; Weaver, M. J., Surface-Enhanced Raman-Scattering from Sputter-Deposited Silver Surfaces. *Analytical Chemistry* **1986,** *58* (7), 1290-1294.
143. Kneipp, K.; Wang, Y.; Kneipp, H.; Perelman, L. T.; Itzkan, I.; Dasari, R.; Feld, M. S., Single molecule detection using surface-enhanced Raman scattering (SERS). *Physical Review Letters* **1997,** *78* (9), 1667-1670.
144. Xu, H. X.; Bjerneld, E. J.; Kall, M.; Borjesson, L., Spectroscopy of single hemoglobin molecules by surface enhanced Raman scattering. *Physical Review Letters* **1999,** *83* (21), 4357-4360.
145. Chu, Y. Z.; Banaee, M. G.; Crozier, K. B., Double-Resonance Plasmon Substrates for Surface-Enhanced Raman Scattering with Enhancement at Excitation and Stokes Frequencies. *Acs Nano* **2010,** *4* (5), 2804-2810.
146. Zhu, W. Q.; Banaee, M. G.; Wang, D. X.; Chu, Y. Z.; Crozier, K. B., Lithographically Fabricated Optical Antennas with Gaps Well Below 10 nm. *Small* **2011,** *7* (13), 1761-1766.
147. Jensen, T. R.; Schatz, G. C.; Van Duyne, R. P., Nanosphere lithography: Surface plasmon resonance spectrum of a periodic array of silver nanoparticles by ultraviolet-visible extinction spectroscopy and electrodynamic modeling. *Journal of Physical Chemistry B* **1999,** *103* (13), 2394-2401.
148. Kahl, M.; Voges, E.; Kostrewa, S.; Viets, C.; Hill, W., Periodically structured metallic substrates for SERS. *Sensors and Actuators B-Chemical* **1998,** *51* (1-3), 285-291.

149. Koh, A. L.; Fernandez-Dominguez, A. I.; McComb, D. W.; Maier, S. A.; Yang, J. K. W., High-Resolution Mapping of Electron-Beam-Excited Plasmon Modes in Lithographically Defined Gold Nanostructures. *Nano Lett* **2011,** *11* (3), 1323-1330.
150. Fromm, D. P.; Sundaramurthy, A.; Schuck, P. J.; Kino, G.; Moerner, W. E., Gap-dependent optical coupling of single "Bowtie" nanoantennas resonant in the visible. *Nano Lett* **2004,** *4* (5), 957-961.
151. Tabor, C.; Murali, R.; Mahmoud, M.; El-Sayed, M. A., On the Use of Plasmonic Nanoparticle Pairs As a Plasmon Ruler: The Dependence of the Near-Field Dipole Plasmon Coupling on Nanoparticle Size and Shape. *Journal of Physical Chemistry A* **2009,** *113* (10), 1946-1953.
152. Duan, H. G.; Fernandez-Dominguez, A. I.; Bosman, M.; Maier, S. A.; Yang, J. K. W., Nanoplasmonics: Classical down to the Nanometer Scale. *Nano Letters* **2012,** *12* (3), 1683-1689.
153. Ding, W.; Bachelot, R.; Kostcheev, S.; Royer, P.; de Lamaestre, R. E., Surface plasmon resonances in silver Bowtie nanoantennas with varied bow angles. *Journal of Applied Physics* **2010,** *108* (12).
154. Rechberger, W.; Hohenau, A.; Leitner, A.; Krenn, J. R.; Lamprecht, B.; Aussenegg, F. R., Optical properties of two interacting gold nanoparticles. *Optics Communications* **2003,** *220* (1-3), 137-141.
155. Kolega, R. R.; Schlenoff, J. B., Self-assembled monolayers of an aryl thiol: Formation, stability, and exchange of adsorbed 2-naphthalenethiol and bis(2-naphthyl) disulfide on Au. *Langmuir* **1998,** *14* (19), 5469-5478.

APPENDICES

THE JOURNAL OF PHYSICAL CHEMISTRY Letters

Letter

pubs.acs.org/JPCL

Optimizing Electromagnetic Hotspots in Plasmonic Bowtie Nanoantennae

Stephanie Dodson,[†] Mohamed Haggui,[‡] Renaud Bachelot,[‡] Jérôme Plain,*[,‡] Shuzhou Li,*[,¶] and Qihua Xiong*[,†,§]

[†]Division of Physics and Applied Physics, School of Physical and Mathematical Sciences, Nanyang Technological University, Singapore 637371

[‡]Laboratoire de Nanotechnologie et d'Instrumentation Optique, ICD, Université de Technologie de Troyes, France

[¶]School of Materials Science and Engineering and [§]Division of Microelectronics, School of Electrical and Electronic Engineering, Nanyang Technological University, Singapore 639798

ABSTRACT: Sensitivity is a key factor in the improvement of nanoparticle-based biosensors. Bowtie nanoantennae have shown high sensitivity for both surface-enhanced Raman scattering (SERS)- and localized surface plasmon resonance (LSPR)-based biosensing. In this work, optical bowtie nanoantennae with varying geometries were simulated, fabricated, and characterized. We successfully fabricated sub-5 nm gaps between prisms. The gap between prisms, the prism size, and the radius of curvature of the prism corners were characterized for their effects on the optical and electromagnetic properties. Bowties were characterized using LSPR, SERS, and photochemical near-field imaging. The results indicate that the radius of curvature of the prism corners has an important effect on the SERS abilities of a nanoparticle array. The trends described herein can be utilized to intelligently design highly sensitive SERS and LSPR biosensing substrates.

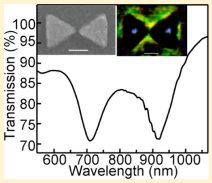

SECTION: Plasmonics, Optical Materials, and Hard Matter

Metallic nanostructures including both chemically synthesized nanoparticles and nanostructures by top-down fabrication have been demonstrated as effective surface-enhanced Raman scattering (SERS) substrates, which can be used toward highly sensitive and specific biosensing.[1] With such high sensitivity SERS biosensors, the earlier diagnosis of diseases, such as cancer, leads to more effective early treatment and higher survival rates. The challenge lies in the fact that the concentration of disease biomarkers at early diagnosis stages is usually very low.[2] This is normally the limiting factor in how early the disease can be detected using proteomic biosensors. Higher detection sensitivity in proteomic biosensors allows for the accurate recognition of lower concentrations of biomarkers, implying the possibility of earlier diagnosis.[2] New, nanotechnology-based biosensors make use of the unique optical and electric properties of nanoscale particles. With this in mind, it is of great interest to exploit the novel properties exhibited by noble metals in the nanoscale for making sensitive, plasmonics-based biosensing technologies. Biosensors based on SERS and localized surface plasmon resonance (LSPR) have great potential as very rapid and sensitive tools.[3,4] SERS biosensing involves the use of enhanced local electric fields of plasmonic devices to increase the Raman signal of biomolecules and biomarkers. These increased signals mean that lower concentrations of biomarkers still produce readable signatures and allow for detection with much lower sample volume or very low concentration samples. LSPR biosensing makes use of the sensitivity of plasmonic devices to their dielectric environment to detect binding events between biomolecules.[5]

A variety of different types of bowtie substrates have been explored for their potential as high sensitivity biosensors. The contours of roughened metal surfaces[6−8] and solution-grown aggregated particles[9,10] were shown to exhibit enhanced Raman signals. Nanosphere lithography fabricated bowties offer good homogeneity and reproducibility but have limited geometries.[11] Structures fabricated using electron beam lithography can be controlled in the nanometer regime for independent variation of geometrical parameters.[12,13] Various geometries of nanoparticles have been explored previously for SERS potential. Particle shape, size, and material will affect the location and intensity of hotspots and the optical and electromagnetic properties of the particle.[14] Experimental work exploring sub-5 nm gaps in other geometries such as spherical dimers has shown great potential for an increased SERS enhancement factor in this regime.[15,16] Spherical, cylindrical, and rectangular prisms were found to be inferior to bowtie nanoantennae prism dimers facing tip to tip for electric field enhancement.[17] Near-field studies making use of photosensitive polymers have been conducted previously on bowtie nanoantennae and hotspots supported by nanorods, and the electric near-field features were well correlated with simulations.[18,19] The gap size between prisms has also been explored previously, and decreasing gap size was found to red shift the resonance.[20,21] The Raman signal increased with decreasing gap size up to the limit of fabrication,

Received: December 5, 2012
Accepted: January 21, 2013

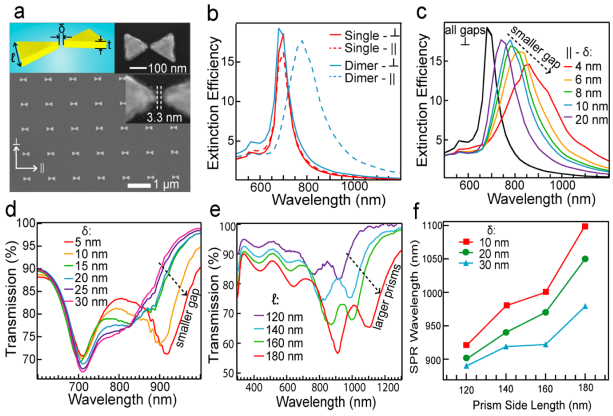

Figure 1. LSPR. (a) SEM image of the bowtie nanoantenna array. The left inset shows a diagram illustrating the variable usage used throughout the document. The right insets show high-magnification SEM images of a 3.3 nm gap bowtie nanoantenna. (b) Extinction efficiency of a single prism and prism dimer for both polarizations. (c) Extinction efficiency of prism dimers with varying gap spacing for both polarizations. (d) Transmission spectra of prism dimers with varying gaps between prisms. (e) Transmission spectra of prism dimers with varying prism side lengths. (f) Parallel mode SPR wavelength trends for several gap sizes of bowtie nanoantenna as the prism side length is increased. Calculations were done in DDSCAT.

which previously was an 8 nm gap for a bowtie nanoantenna.[22] Simulations have predicted that the electric field enhancement will continue to increase with decreasing gap size until the range at which quantum effects dominate and the enhancement starts to decrease.[17] Recently, bowtie antenna with gaps in the sub-5 nm regime have been studied for electron energy loss by scanning tunneling electron microscopy.[23] These previous studies inspire great interest in studying bowties with sub-5 nm gaps for potential biosensing applications. The bow angle has been explored for bowtie nanoantennae, and the resonance was found to first blue shift and then red shift with increasing bow angle.[24] To the best of our knowledge, the effect of the radius of curvature (ROC) of the prism corners has not been isolated experimentally and explored.

We show in this work the large-scale, reproducible fabrication of bowtie nanoantennae, systematically exploring how the scattering properties, electric near-field features, and electric field enhancement change as a function of the geometry of the nanoantennae. The bowtie gap size, prism size, thickness, and ROC of the prism corners were explored. Bowtie nanoantennae, shown in Figure 1a, with varying geometric parameters have been fabricated reproducibly in the sub-5 nm regime and characterized. The SPR was characterized by discrete dipole approximation (DDA) scattering calculations and spectroscopy measurements. The electric field was characterized by DDA electric field mapping, Raman spectroscopy, and photochemical near-field imaging.

The LSPR of nanoparticles can be highly controllable and tunable. It was of interest to explore the LSPR of bowtie nanoantennae in order to better understand their optical properties. A highly controllable LSPR also has potential applications in designing sensitive binding event based biosensing platforms. The effect of the gap spacing between the prisms of a bowtie nanoantenna on optical properties was systematically explored by holding all other parameters constant and varying the gap between prisms. A simulation using the DDA method has been carried out to identify the modes involved in the transmission spectra. As shown in Figure 1b for a bowtie nanoantenna with a size of 150 nm and a gap size 20 nm, when the incoming irradiation polarization is parallel to the bowtie axis, the extinction efficiency has a peak at around 800 nm. When the irradiation polarization is perpendicular to the gap, the peak is at around 700 nm. It should also be noted that the extinction efficiency peaks for both polarizations of a single 150 nm prism are at around 700 nm as well. In Figure 1c, we display the simulation results of the extinction efficiency for a bowtie nanoantenna with the gap spacing, δ, varied from 4 to 20 nm when the incoming irradiation is polarized along the gap, keeping the size (l = 150 nm) and thickness (t = 30 nm) constant. Unambiguously, the extinction shows a peak at around 900 nm for a gap size of 4 nm. This peak red shifts significantly as the gap size is decreased from 20 to 4 nm, giving rise to an 800 nm peak for a 20 nm gap. Simulations have also been conducted for the polarization perpendicular to the bowtie axis for different gap sizes. The mode due to polarization perpendicular to the axis of the bowtie did not show a noticeable resonance shift for different gap sizes and was similar to the resonances of single prisms. All of the gaps, 4−20 nm, for perpendicular polarization are shown overlaying each other in black color in Figure 1c.

The modes and effects of the gap on the resonance were studied by taking the transmission spectra of bowtie nanoantennae with gap spacings between 4 and 30 nm, as shown in Figure 1d. Two absorption bands were observed; one band around 700 nm does not vary with the gap spacing, while the other band red shifts as the gap spacing decreases. We observed that both resonance peaks are due to the two different polarization-based modes. In particular, the peak due to longitudinal polarization, parallel to the bowtie axis, shows a systematic red shift with decreasing gap, as suggested by the DDA simulation. The calculated extinction efficiency shows a different resonance for both the polarization parallel to and

dx.doi.org/10.1021/jz302018x | J. Phys. Chem. Lett. 2013, 4, 496−501

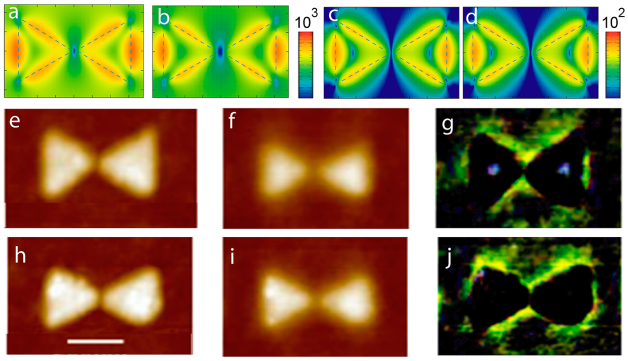

Figure 2. Electric near-field. (a–d) Simulated electric near-field of a bowtie nanoantenna with (a,c) a 6 nm gap and (b,d) a 10 nm gap between prisms. (a,b) Simulated total electric near-field, $|E|^4$, contour plot. (c,d) Simulated out-of-plane component of electric field, $|E_z|^2$, contour plots. (e–j) Experimental near-field imaged using a photosensitive polymer film for (e–g) a 6 nm gap between prisms and (h–j) a 10 nm gap between prisms. (e,h) Atomic force microscopy (AFM) images taken before exposure. (f,i) AFM images taken after exposure. (g,j) Differential images made using image subtraction to view the effect of the near-field. Polarization is longitudinal for all near-field simulated and experimental images.

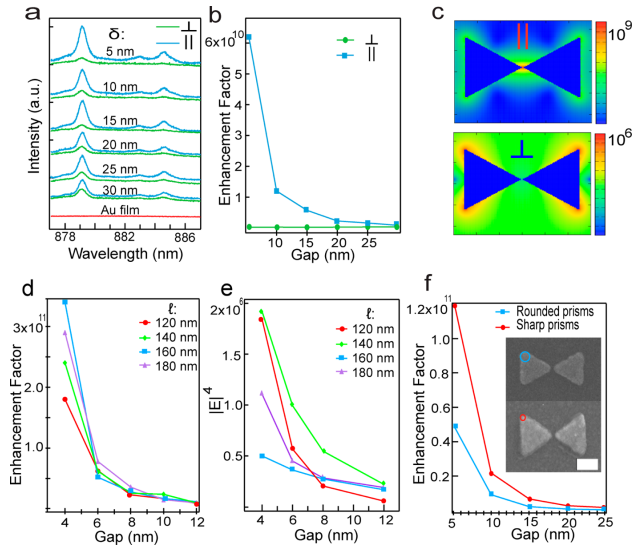

Figure 3. SERS. (a) Raman spectra and (b) the enhancement factor of prism dimers with varying gaps between prisms for both polarizations. (c) Simulated electric field contour plot of both modes. (d) Enhancement factor and (e) averaged $|E|^4$ of prism dimers with varying gaps between prisms and varying prism side lengths. (f) The enhancement factor of prism dimers with varying gaps between prisms for two different ROCs. The inset shows the SEM image of round and sharp prism dimers. The scale bar is 100 nm. Calculations were done using DDSCAT.

perpendicular to the bowtie axis. The peak corresponding to the perpendicular polarization does not vary with changing gap size, while the peak corresponding to the parallel polarization red shifts with decreasing gap size. The transmission data show two peaks, one of which remains constant with a gap change and the other that red shifts with decreasing gap size. The correspondence of the transmission data to the calculated extinction efficiency implies that the two transmission modes must correspond to the two polarizations. The red shift with decreasing gap size implies a decrease in energy. This well-known behavior is explained by a weakening of the restoring forces for the oscillating electrons due to the presence of the charge distribution of the second particle.[25]

It was of interest to observe the effect of the side length of the prisms of a bowtie nanoantenna on the optical properties. By holding all other parameters constant and varying the side length of prisms, the LSPR has been explored systematically by both simulation and experiments. DDA extinction efficiency simulations were conducted for bowtie nanoantennae with varying prism sizes and gap spacings. Both polarizations, parallel and perpendicular to the bowtie axis, were simulated. The prism size was varied from 120 to 180 nm. The gap spacing was varied from 4 to 10 nm. The SPR for both modes, perpendicular and parallel to the axis, red shifted for increasing prism size. Optical transmission spectra were taken of bowtie nanoantennae with varying prism sizes and gap spacings, as shown in Figure 1e. The prism size was varied from 120 to 180 nm, and the gap size was varied from 4 to 30 nm. The two modes, for polarization perpendicular and parallel to the bowtie axis, red shifted for increasing prism size. The red shift with increasing prism size was more dramatic for smaller gap sizes, as shown in Figure 1f. Both of the modes observed in extinction efficiency simulations red -shifted with increasing prism size. The modes observed in transmission spectroscopy red shifted with increasing prism size, which agreed with simulation.

The visualization of the local near-field is of interest to identify the modes of excitation and to aid in the intelligent design of SERS substrates.[26] Using a photosensitive polymer layer over the bowtie allows the near-field excited in the particle to induce molecular motion and imprint the near-field features into the surface of the polymer. Simulated electric field contour plots were calculated using DDA for 568 nm excitation, as shown in Figure 2a–d. Figure 2a and b shows the simulated total electric near-field, $|E|^4$, contour plots for a 6 and 10 nm gap, respectively, with noticeable hotspot features along the edges of the prisms. Figure 2c and d shows the out-of-plane component of electric field, $|E_z|^2$, contour plots for a 6 and 10 nm gap, respectively.

Photochemical near-field imaging was used to directly map the near-field of bowtie nanoantennae with 568 nm excitation, as shown in Figure 2e–j. Figure 2e and h shows an AFM image before exposure for a bowtie with 6 and 10 nm gaps between prisms, respectively. After exposure to an external electromagnetic field, the near-field features will have changed the surface of the polymer, as shown in Figure 2f and i for a 6 and 10 nm gap, respectively. In order to better visualize the changes in the polymer surface, differential images were made using image subtraction between the AFM images taken before and after exposure, as shown in Figure 2g and j for 6 and 10 nm gaps, respectively. The features visualized in the photochemical near-field experiment showed very good agreement with the features in the electric field contour plots; the hotspot was localized along the edges of the prisms for all gap sizes for both experiment and simulation. The excitation mode visualized in this experiment is one of limited interest; the absorption band of the photosensitive polymer ends at around 600 nm. Currently, work is ongoing to explore options, such as two-photon absorption of the photopolymer, for visualizing the near-field features of modes excited by different wavelengths, especially those shown in Figure 3c.

The engineering of hotspots and surface plasmon localization are of interest for applications in SERS biosensing. The more localized an electric field hotspot is, the more intense it is, and thus, it will give more surface enhancement effects to Raman scattering signals. These enhanced signals allow for more sensitive detection of biomarkers. The effect of gap on electric field enhancement was studied through Raman spectroscopy and DDA calculations on bowtie nanoantennae with gaps between prisms varying from 4 to 30 nm. Smaller gap sizes resulted in higher Raman enhancement for parallel polarization, while perpendicular polarization did not show significant change, as shown in Figure 3a. Polarizations parallel to the bowtie axis had higher enhancement factors than perpendicular polarization, shown in Figure 3b. The theoretical electric field enhancement was calculated with the use of electric field simulations in DDSCAT using 785 nm excitation, shown in Figure 3c. The electric field contour plot simulations for 785 nm excitation show that the hotspot is located in between the prisms for polarization parallel to the bowtie axis and on the outer corners for polarization perpendicular to the bowtie axis. The calculated electric field enhancement increases with decreasing gap size for polarization parallel to the bowtie axis, until the limit of the fabrication abilities, which agrees with simulation results and previous studies.[17] The Raman signal was not significantly enhanced by the polarization perpendicular to the antenna axis and did not vary significantly with changing gap size.

The electric field was simulated and experimentally explored using SERS and DDA electric field calculations for bowtie nanoantennae with varying prism sizes. An excitation wavelength of 785 nm was used for all simulations and experimental measurements. The prism size was varied from 120 to 180 nm for gap spacings from 4 to 30 nm. The electric field intensity increased with decreasing gap for all prism sizes in both experiment and simulation, as shown in Figure 3d and e, respectively. The calculated electric field peaked for prisms with a 140 nm side length and a 4 nm gap. The Raman enhancement factor was highest for the 160 nm prism size and 4 nm gap. The discrepancy between simulation and experiment for optimal prism size for 785 nm excitation may be due to the improved prism shape and corner sharpness that result from larger prism fabrication. If so, then improvements in fabrication technique may improve the experimental enhancement of the smaller prisms, and the data might more closely follow the trend predicted in simulation. It is noteworthy that 785 nm excitation is off-resonance, in varying degrees for different geometries. It would be of interest to explore on-resonance excitations in order to more carefully study the plasmon modes and fully exploit the potential of bowtie antennae as a SERS biosensing substrate.

It was of interest to observe the effect of the ROC of the corners of the prisms of a bowtie nanoantenna on optical properties and the electric field. By holding all other geometrical parameters constant and varying the fabrication recipe, specifically increasing the dosage of the electron beam, the ROC was controlled, and its effects on the electrical and optical properties were observed. The optical transmission spectra were taken of bowtie nanoantennae with both sharp and rounded corners for varying gap spacing between prisms. Both modes, due to polarization perpendicular and parallel to the bowtie axis, red shifted for increasing sharpness of the prism corners. Raman spectra were taken for bowtie nanoantennae with varying ROCs and gap sizes. The Raman enhancement factor increased with decreasing gap size for both round and sharp bowties, but the increase was more dramatic for the sharp bowties, as shown in Figure 3f. This agrees with the school of thought that electrons are more fully confined in the smaller ROC corners and would induce more electric field enhancement. It would be of interest to observe more ROCs through

controlled fabrication, ranging from circular dimers to prism dimers.

In this work, we have fabricated and characterized bowtie nanoantennae with varying gaps, prism sizes, and ROCs. We have been able to fabricate very small gaps in bowtie nanoantennae, in the sub-5 nm range, and have confirmed the continuation of trends found in previous work. The results on the variation of the bowtie prism size were found to agree with the studies on varying the size of individual prisms. We have found evidence that the ROC has a significant impact on the LSPR and electric field enhancement. We found that simulated predictions of the effects of geometry can be experimentally confirmed for the effect of gap and prism size on the SPR and the EF enhancement. The SPR peak corresponding to the parallel polarization was found to red shift with decreasing gap size while the peak corresponding to the perpendicular polarization remained fixed. The Raman signal enhancement was found to increase with decreasing gap for parallel polarization but did not change significantly for perpendicular polarization. The two modes, for polarization perpendicular and parallel to the bowtie axis, red shifted for increasing prism size. The trend of increasing enhancement with decreasing gap size was true for all prism sizes. As the ROC decreases and the prism corners become sharper, both resonance peaks red shift, and the Raman signal enhancement increases. This implies that the electric field enhancement is higher for sharper cornered bowties. The increased enhancement resulting from the decreasing gap sizes and ROC can be exploited for making highly sensitive biosensors

Simulation of the particle scattering was carried out using the DDA in the DDSCAT program.[27,28] DDSCAT version 7.0 and a 1 nm grid were used for all simulations. The dielectric constants of Au are from Johnson and Christy.[29] The electric field intensity and thus the average and maximum intensity over the nanoparticle surface were calculated for isolated targets in an effective medium of refractive index 1.331. The information was used to make contour plots of the intensity on and around the nanoparticle to visualize the location of the hotspots. The extinction efficiency was simulated for multiple wavelengths to produce spectra used to determine the resonance position of the particle.

Electron beam lithography (EBL) was used to fabricate the bowtie nanoantenna arrays. The same polymer layer was used for all chips, 950 poly(methylmethacrylate) (PMMA) A4. The PMMA was spin coated onto the chips at 4000 rpm for 40 s (Specialty Coating Model P6700) and then baked at 180 °C for 15 min. EBL was performed using a JEOL JSM-7001F field emission scanning electron microscopy (FESEM) equipped with a Deben Beam Blanker and a nanometer pattern generation system (NPGS). After e-beam writing, the chips were developed for 75 s in a solution of 1:3-methyl isobutyl ketone (MIBK)/isopropyl alcohol (IPA) at room temperature. After development, the chips were rinsed for 20 s in IPA and blown dry using nitrogen or compressed air. Evaporation of 2 nm Cr and 30 nm Au was sequentially done in a thermal evaporator (Elite Engineering, Singapore). The chamber pressure of 2×10^{-7} Torr and evaporation rate of 0.6 Å/s were used for evaporation. Liftoff was done at room temperature in acetone for 2 h followed by a sonication for 1−2 min at a power level of 2 (Crest Ultrasonics Powersonic P1100D).

Bowtie geometry was confirmed by analysis in SEM; an example is shown in Figure 1a. Also shown in Figure 1a is a illustration demonstrating the geometrical parameters defined as the prism side length, l, thickness, t, and gap between prisms, δ. Statistical analysis was done for the gap size and prism size at 30 000× magnification for 36 bowties per sample and was confirmed at 120 000× magnification for each sample. The nominally 5, 10, 15, 20, 25, and 30 nm gaps had actual gaps of 5.5 ± 1.5, 10.8 ± 1.9, 12.1 ± 3.2, 20.3 ± 1.1, 26.1 ± 1.3, and 29.6 ± 1.5 nm, respectively. The nominal prism side lengths of 180, 160, 140, and 120 nm had actual lengths of 179.8 + 4.0, 158.1 + 3.7, 139.9 + 3.8, and 108.8 + 3.3 nm, respectively. The sharp and round bowties had tip ROCs of 16.6 + 2.8 and 28.8 + 2.0 nm, respectively. Round bowties had nominal gaps of 5, 10, 15, 20, and 25 nm and actual gaps of 5.4 ± 2.0, 9.9 ± 1.6, 16.9 ± 2.5, 19.6 ± 1.1, and 24.1 ± 2.3 nm, respectively

Transmission spectroscopy on a microspectrophotometer (Craic, U.S.A.) with nonpolarized light in air, with an angle of incidence of 90° and an aperture size 15 μm, was performed for three locations per sample. Each sampling measured around 225 bowties.

The molecule used for SERS experiments was 2-naphthalenethiol from Sigma-Aldrich. Substrates were incubated at room temperature in a solution of methanol with a concentration of 5 mM naphthalenethiol for 24 h and then rinsed with methanol and blown dry with nitrogen gas. Raman spectroscopy was conducted with a 785 nm excitation wavelength and a power of 2 mW. A 50× objective with a slit of 300 μm and a numerical aperture of 0.75 was used, with an integration time of 600 s per sample; each sampling measured around 16 bowties. Three locations on each sample were tested for both polarizations, parallel and perpendicular to the antenna axis. The Raman enhancement factor is a quantitative measure of the increase in Raman signal due to the enhanced electric field in SERS substrates and is given by

$$\mathrm{EF} = \left(\frac{N_{\mathrm{bulk}}}{N_{\mathrm{SERS}}7}\right)\left(\frac{I_{\mathrm{SERS}}}{I_{\mathrm{bulk}}}\right)$$

where N_{bulk} is the total number of molecules in the bulk sample, N_{SERS} in this work is the number of molecules contributing to the SERS signal, I_{bulk} is the intensity of the Raman signal for the bulk sample, and I_{SERS} is the intensity of the Raman signal for the SERS sample. It should be noted that in this work, the N_{SERS} has been normalized for the volume of the hotspot as determined from DDA electric near-field contour plots and assuming a self-assembling monolayer of thiolated molecule on the surface of the gold. In this Letter, we used naphthalenethiol, which has a molecular footprint of 0.42 nm^2.[30]

Photochemical near-field imaging was done using an approach similar to that reported by Haggui and co-workers.[31] A thin film of DR1/PMMA was spin-coated onto the substrate. AFM images were taken of polymer-coated nanoparticles. The sample was exposed at 568 nm using an Ar−Kr laser source, with a power of 200mW/cm^2, for 40 min. The polarization was along the major axis of the bowtie. AFM images were taken after exposure of the same nanoparticles. Differential images were obtained through postprocessing image subtraction.

AUTHOR INFORMATION

Corresponding Author

*E-mail: jerome.plain@utt.fr (J.P.); lisz@ntu.edu.sg (S.L.); qihua@ntu.edu.sg (Q.X.).

Notes

The authors declare no competing financial interest.

■ ACKNOWLEDGMENTS

The author Q.X. would like to acknowledge the strong support from the Singapore National Research Foundation through a Fellowship Grant (NRF-RF2009-06) and start-up grant support from Nanyang Technological University (M58110061). Q.X. and S.L. gratefully acknowledge the strong support from the Singapore Ministry of Education via two Tier 2 Grants (MOE2011-T2-2-051 and MOE2011-T2-2-085), respectively. The author J.P. would like to acknowledge the financial support of Nano'Mat (www.nanomat.eu) by the Ministère de l'enseignement supérieur et de la recherche, the Conseil régional Champagne-Ardenne, the FEDER funds, and the Conseil général de l'Aube. Q.X., S.L.D., and J.P. would like to acknowledge the France−Singapore Merlion Project.

■ REFERENCES

(1) Halas, N. J.; Lal, S.; Link, S.; Chang, W. S.; Natelson, D.; Hafner, J. H.; Nordlander, P. A Plethora of Plasmonics from the Laboratory for Nanophotonics at Rice University. *Adv. Mater.* **2012**, *24*, 4842−4877.
(2) Wulfkuhle, J. D.; Liotta, L. A.; Petricoin, E. F. Proteomic Applications for the Early Detection of Cancer. *Nat. Rev. Cancer* **2003**, *3*, 267−275.
(3) Anker, J. N.; Hall, W. P.; Lyandres, O.; Shah, N. C.; Zhao, J.; Van Duyne, R. P. Biosensing with Plasmonic Nanosensors. *Nat. Mater.* **2008**, *7*, 442−453.
(4) Moskovits, M. Surface-Enhanced Spectroscopy. *Rev. Mod. Phys.* **1985**, *57*, 783−826.
(5) Halas, N. J.; Lal, S.; Chang, W. S.; Link, S.; Nordlander, P. Plasmons in Strongly Coupled Metallic Nanostructures. *Chem. Rev.* **2011**, *111*, 3913−3961.
(6) Fleischm., M.; Hendra, P. J. Mcquilla.Aj, Raman-Spectra of Pyridine Adsorbed at a Silver Electrode. *Chem. Phys. Lett.* **1974**, *26*, 163−166.
(7) Miller, S. K.; Baiker, A.; Meier, M.; Wokaun, A. Surface-Enhanced Raman-Scattering and the Preparation of Copper Substrates for Catalytic Studies. *J. Chem. Soc., Faraday Trans. 1* **1984**, *80*, 1305−1312.
(8) Davies, J. P.; Pachuta, S. J.; Cooks, R. G.; Weaver, M. J. Surface-Enhanced Raman-Scattering from Sputter-Deposited Silver Surfaces. *Anal. Chem.* **1986**, *58*, 1290−1294.
(9) Kneipp, K.; Wang, Y.; Kneipp, H.; Perelman, L. T.; Itzkan, I.; Dasari, R.; Feld, M. S. Single Molecule Detection Using Surface-Enhanced Raman Scattering (SERS). *Phys. Rev. Lett.* **1997**, *78*, 1667−1670.
(10) Xu, H. X.; Bjerneld, E. J.; Kall, M.; Borjesson, L. Spectroscopy of Single Hemoglobin Molecules by Surface Enhanced Raman Scattering. *Phys. Rev. Lett.* **1999**, *83*, 4357−4360.
(11) Jensen, T. R.; Schatz, G. C.; Van Duyne, R. P. Nanosphere Lithography: Surface Plasmon Resonance Spectrum of a Periodic Array of Silver Nanoparticles by Ultraviolet-Visible Extinction Spectroscopy and Electrodynamic Modeling. *J. Phys. Chem. B* **1999**, *103*, 2394−2401.
(12) Kahl, M.; Voges, E.; Kostrewa, S.; Viets, C.; Hill, W. Periodically Structured Metallic Substrates for SERS. *Sens. Actuators, B* **1998**, *51*, 285−291.
(13) Koh, A. L.; Fernandez-Dominguez, A. I.; McComb, D. W.; Maier, S. A.; Yang, J. K. W. High-Resolution Mapping of Electron-Beam-Excited Plasmon Modes in Lithographically Defined Gold Nanostructures. *Nano Lett.* **2011**, *11*, 1323−1330.
(14) Kelly, K. L.; Coronado, E.; Zhao, L. L.; Schatz, G. C. The Optical Properties of Metal Nanoparticles: The Influence of Size, Shape, And Dielectric Environment. *J. Phys. Chem. B* **2003**, *107*, 668−677.
(15) Chu, Y. Z.; Banaee, M. G.; Crozier, K. B. Double-Resonance Plasmon Substrates for Surface-Enhanced Raman Scattering with Enhancement at Excitation and Stokes Frequencies. *ACS Nano* **2010**, *4*, 2804−2810.
(16) Zhu, W. Q.; Banaee, M. G.; Wang, D. X.; Chu, Y. Z.; Crozier, K. B. Lithographically Fabricated Optical Antennas with Gaps Well Below 10 nm. *Small* **2011**, *7*, 1761−1766.
(17) Hao, E.; Schatz, G. C. Electromagnetic Fields around Silver Nanoparticles and Dimers. *J. Chem. Phys.* **2004**, *120*, 357−366.
(18) Hubert, C.; Bachelot, R.; Plain, J.; Kostcheev, S.; Lerondel, G.; Juan, M.; Royer, P.; Zou, S. L.; Schatz, G. C.; Wiederrecht, G. P.; Gray, S. K. Near-Field Polarization Effects in Molecular-Motion-Induced Photochemical Imaging. *J. Phys. Chem. C* **2008**, *112*, 4111−4116.
(19) Juan, M. L.; Plain, J.; Bachelot, R.; Vial, A.; Royer, P.; Gray, S. K.; Montgomery, J. M.; Wiederrecht, G. P. Plasmonic Electromagnetic Hot Spots Temporally Addressed by Photoinduced Molecular Displacement. *J. Phys. Chem. A* **2009**, *113*, 4647−4651.
(20) Fromm, D. P.; Sundaramurthy, A.; Schuck, P. J.; Kino, G.; Moerner, W. E. Gap-Dependent Optical Coupling of Single "Bowtie: Nanoantennas Resonant in the Visible. *Nano Lett.* **2004**, *4*, 957−961.
(21) Tabor, C.; Murali, R.; Mahmoud, M.; El-Sayed, M. A. On the Use of Plasmonic Nanoparticle Pairs As a Plasmon Ruler: The Dependence of the Near-Field Dipole Plasmon Coupling on Nanoparticle Size and Shape. *J. Phys. Chem. A* **2009**, *113*, 1946−1953.
(22) Hatab, N. A.; Hsueh, C. H.; Gaddis, A. L.; Retterer, S. T.; Li, J. H.; Eres, G.; Zhang, Z. Y.; Gu, B. H. Free-Standing Optical Gold Bowtie Nanoantenna with Variable Gap Size for Enhanced Raman Spectroscopy. *Nano Lett.* **2010**, *10*, 4952−4955.
(23) Duan, H. G.; Fernandez-Dominguez, A. I.; Bosman, M.; Maier, S. A.; Yang, J. K. W. Nanoplasmonics: Classical down to the Nanometer Scale. *Nano Lett.* **2012**, *12*, 1683−1689.
(24) Ding, W.; Bachelot, R.; Kostcheev, S.; Royer, P.; de Lamaestre, R. E. Surface Plasmon Resonances in Silver Bowtie Nanoantennas with Varied Bow Angles. *J. Appl. Phys.* **2010**, *108*, 124314−124320.
(25) Rechberger, W.; Hohenau, A.; Leitner, A.; Krenn, J. R.; Lamprecht, B.; Aussenegg, F. R. Optical Properties of Two Interacting Gold Nanoparticles. *Opt. Commun.* **2003**, *220*, 137−141.
(26) Guiton, B. S.; Iberi, V.; Li, S. Z.; Leonard, D. N.; Parish, C. M.; Kotula, P. G.; Varela, M.; Schatz, G. C.; Pennycook, S. J.; Camden, J. P. Correlated Optical Measurements and Plasmon Mapping of Silver Nanorods. *Nano Lett.* **2011**, *11*, 3482−3488.
(27) Draine, B. T.; Flatau, P. J. Discrete-Dipole Approximation for Scattering Calculations. *J. Opt. Soc. Am. A* **1994**, *11*, 1491−1499.
(28) Draine, B. T.; Flatau, P. J. Discrete-Dipole Approximation for Periodic Targets: Theory and Tests. *J. Opt. Soc. Am. A* **2008**, *25*, 2693−2703.
(29) Johnson, P. B.; Christy, R. W. Optical Constants of Noble Metals. *Phys. Rev. B* **1972**, *6*, 4370−4379.
(30) Kolega, R. R.; Schlenoff, J. B. Self-Assembled Monolayers of an Aryl Thiol: Formation, Stability, And Exchange of Adsorbed 2-Naphthalenethiol and Bis(2-naphthyl) Disulfide on Au. *Langmuir* **1998**, *14*, 5469−5478.
(31) Haggui, M.; Dridi, M.; Plain, J.; Marguet, S.; Perez, H.; Schatz, G. C.; Wiederrecht, G. P.; Gray, S. K.; Bachelot, R. Spatial Confinement of Electromagnetic Hot and Cold Spots in Gold Nanocubes. *ACS Nano* **2012**, *6*, 1299−1307.

Nanoscale RSCPublishing

ARTICLE

Engineering Plasmonic Nanorod Arrays for Colon Cancer Marker Detection

Cite this: DOI: 10.1039/x0xx00000x

Received ooth January 2012,
Accepted ooth January 2012

DOI: 10.1039/x0xx00000x

www.rsc.org/

Stephanie L. Dodson,[a] Cuong Cao,[b] Hamed Zaribafzadeh,[a] Shuzhou Li,[c] and Qihua Xiong [a,d]

Engineering plasmonic nanomaterials or nanostructures towards ultrasensitive biosensing for disease markers or pathogens is of high importance. Here we demonstrate a systematic approach to tailor effective plasmonic nanorod arrays by combining both comprehensive numerical discrete dipole approximations (DDA) simulation and transmission spectroscopy experiments. The results indicate that 200 × 50 nm nanorod arrays with 300 × 500 nm period provide the highest FOM of 3.6 and a sensitivity of 310 nm/RIU. Furthermore, we demonstrate the use of nanorod arrays for the detection of single nucleotide polymorphism in codon 12 of the K-*ras* gene that are frequently occurring in early stages of colon cancer, with a sensitivity down to 10 nM in the presence of 100-fold higher concentration of the homozygous genotypes. Our work shows significant potential of nanorod arrays towards point-of-care applications in diagnosis and clinical studies.

Introduction

Recently, we have witnessed considerable efforts for the development of plasmonics and photonics-based nanosensors for biochemical and genetic analysis, especially for screening and rapid detection of cancer markers.[1-15] These systems provide a range of benefits such as shorter analysis time, lower consumption of sample, chemical reagent and energy, lower cost, and portability. Towards this end, the usage of the dielectric sensitivity of localized surface plasmon resonances (LSPR) of nanoparticles has been shown to be particularly robust and very sensitive to changes in the dielectric environment of surrounding.[16-19] The effects of periodicity, geometry, polarization, and dielectric environment have been explored for tuning the LSPR responses of nanosphere, trianglular nanoprism, nanorods, *etc*. Highly sensitive LSPR biosensing has been done using the various plasmonic substrates.[16, 20-23] Among them, the nanorods possess outstanding plasmonic and photonic properties, exhibiting intrinsic transverse and longitudinal modes. Unlike other nanoparticle shapes, the longitudinal mode has been shown to be more sensitive to changes in refractive index and exhibit a better figure of merit (FOM) value. More importantly, bandwidth and the LSPR sensitivity of the AuNRs can be optimized by tuning their aspect ratios. One- and two-dimensional arrays of nanoparticles have been previously studied for their plasmonic resonances and longer wavelength photonic resonances.[24-30] Arrays of gold nanorods showed very sharp resonances that shifted significantly with variations in array parameters. Classical mechanics has been found to be sufficient to describe a system of nanoscale particles in arrays on the order of a wavelength of visible light, for instance, one of the versatile framework is the discrete dipole approximations (DDA) that has been used to study the classical electrodynamics of such a system.[31-33] Previously, DDA simulations of rectangular nanorod arrays showed the appearance of sharp photonic resonances in the near infrared,[30] which have not been experimentally identified.

In this work, nanorod arrays were studied for their plasmonic and photonic resonances and their potential as LSPR biosensing substrates. The plasmonic and photonic modes of gold nanorod arrays were studied through rigorous experiments and DDA simulation to observe their extinction efficiency spectra and

electric near field. Rigorous periodicity studies were carried out to fully understand the behavior of photonic resonances resulting from the array structure. Upon the engineering and optimization of nanorod array, we have successfully used the AuNR array device as a plasmonic nanosensor for the detection of single nucleotide polymorphisms (SNPs) in codon 12 of the K-*ras* gene that are frequently occurring in early stages of colon cancer - the third most common type of human cancer today and the second most common cause of cancer related deaths.[34, 35]

In order to understand the effects of changes in nanorod size and aspect ratio, the DDA was used to simulate the extinction spectra of varying nanorod geometries. This is an important factor to consider, as small variations in the fabrication procedure can drastically affect the experimental particle shape, which determines the LSPR properties. Figure 1a shows the variation in resonance of a single nanorod with constant length and varying width. Spectra for both polarizations are shown, longitudinal (parallel to the nanorod axis) and transverse (perpendicular to the nanorod axis). Figure 1b shows the extinction spectra of a single nanorod with a constant width but varying length. There is very little variation in transverse resonance position for either variation in aspect ratio, though there is a slight red shift for an increase in nanorod thickness. The variation of aspect ratio, the length over the width of the particle, has a dramatic effect on the longitudinal resonance mode. Tuning the aspect ratio from 2.7 to 8 varies the resonance from 900 to 1400 nm. As the aspect ratio of the rod decreases, it becomes more sphere-like, in geometry and resonance.

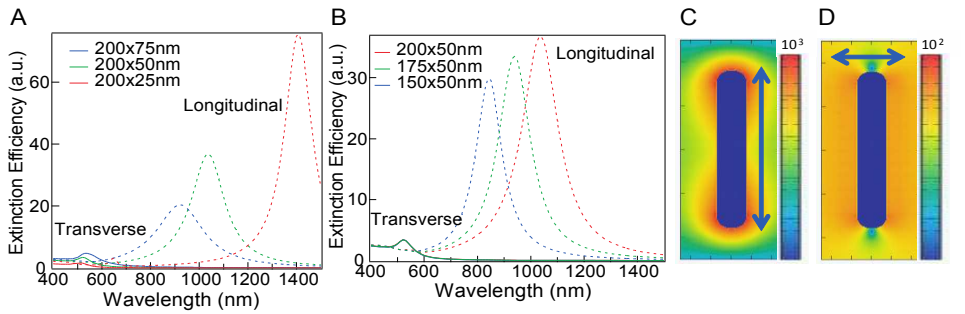

Figure 1. Simulated extinction and electric field of nanorods. Simulated extinction efficiency of single nanorods with varying a) widths and b) lengths. Simulated electric near-field for single 200×50 nm nanorods with c) longitudinal and d) transverse polarization, demonstrated by the blue arrows.

To better understand the two modes, the electric near-field was computed. Figure 1c and d show the electric near-field contour plots of a single nanorod with longitudinal and transverse polarizations, respectively. The longitudinal mode has hotspots located at the ends of the nanorod. The transverse mode has a more uniform electric near-field with cold spots at both ends of the nanorod. The weak electric field excited in the transverse mode will have weak interactions when particles are arranged in arrays. Changes in transverse periodicity may not make much impact on LSPR. The strong, localized electric field excited in the longitudinal mode, however, will interact strongly and changes in longitudinal periodicity will greatly affect the LSPR. It is noteworthy to comment that the local electric field contour can be directly visualized by near-field technique or indirectly mapped atomic force microscopy approaches, in which specific photosensitive polymers can be used to produce topographic variations due to conformational changes upon light irradiation.[36-42]

In order to understand how periodicity affects the LSPR, it is necessary to first understand the effects of the two basic types of one-dimensional arrays. Figure 2 shows the simulated extinction efficiency spectra for a single 200×50 nm nanorod and one-dimensional arrays, for transverse and longitudinal polarizations. Very large period arrays have similar LSPR to a single nanorod, since the particles are far enough apart that coupling is negligible. However, as the period is decreased, and the near field of the particles can interact, the resonance shifts and new features appear. The near field excited in the transverse mode of nanorods does not interact in longitudinal arrays, therefore variation of periodicity in longitudinal arrays did not affect the transverse mode LSPR, as shown in Figure 2a. The hotspots excited in longitudinal mode of nanorods interact strongly in longitudinal arrays and the longitudinal LSPR was greatly affected by changes in longitudinal periodicity, as shown in Figure 2b. The appearance of a new peak around 1200 nm in the arrays with 500 and 1000 nm periodicities with longitudinal polarization warranted further studies, and Figure 2c shows the extinction efficiency of a thorough study of the effect of periodicity in one-dimensional longitudinal arrays with longitudinal polarization. The appearance and subsequent red shift of two peaks is observed. These peaks appear very narrow and red shift and broaden until at their maximum extinction at approximately 830 and 415 nm periods. These values correspond roughly to the LSPR wavelength divided by the refractive index of the surrounding medium, 1.331 (divided by two for the 415 nm period). Figure 2d and e show the extinction efficiency spectra of a single nanorod and various one-dimensional transverse arrays with

transverse and longitudinal polarizations, respectively. There is comparatively little shift in the either resonance position for variations in the transverse periodicity, except when the particles are brought very close together. The longitudinal mode blue shifts as the periodicity decreased and the transverse mode red shifts with decreasing periodicity.

The red shift of the longitudinal mode in Figure 2b and c implies that the electric near field of the longitudinal mode would be affected by changes in longitudinal periodicity. Also, the blue shift in Figure 2e implies that the electric field intensity of the longitudinal mode will increase with decreasing transverse periodicity. Figure 2f shows the simulated maximum electric field intensity for a single nanorod and a variety of one-dimensional arrays with longitudinal polarization. Large period arrays of both types more closely resemble the single nanorod, as expected from similar results with the resonances. As the transverse period is decreased, the electric field increases. As the longitudinal periodicity is decreased the electric field intensity decreases. This result agrees with the patterns observed in the resonance shifts of both types of arrays.

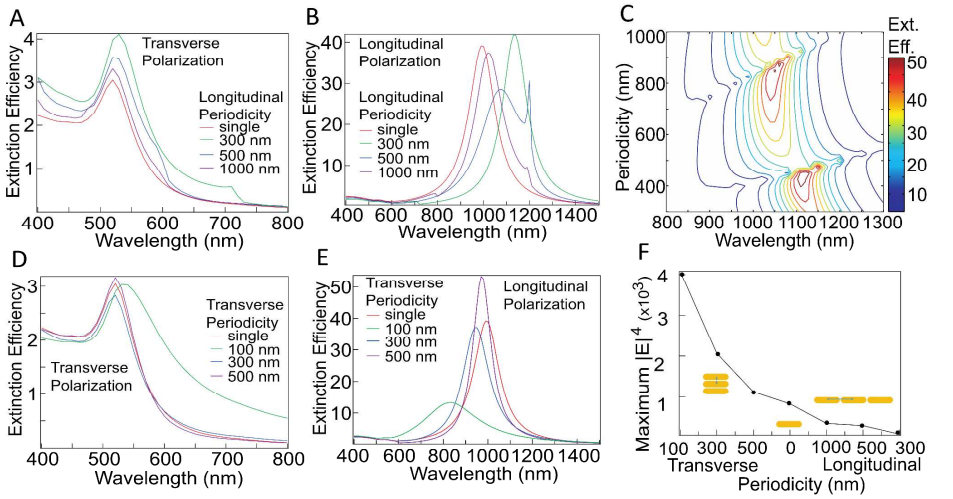

Figure 2. Simulated extinction and electric field of one-dimensional nanorod arrays. a-e) Simulated extinction efficiency spectra for one dimensional arrays of nanorods with: a) longitudinal array with a transverse polarization; b) longitudinal array with a longitudinal polarization; c) further calculations of the longitudinal array with longitudinal polarization to follow the development of the peak formation; d) transverse array with a transverse polarization; e) transverse array with a longitudinal polarization. f) Maximum electric field intensity for varying transverse and longitudinal one dimensional arrays as compared to a single nanorod, all with longitudinal polarization and 785 nm excitation.

After understanding the trends developed when nanorods are introduced into one-dimensional arrays, it is necessary to expand the system to two-dimensional arrays. Simulated spectra of two-dimensional arrays are of interest to compare with, and to better understand, potential experimental conditions. Figure SI1 shows the simulated extinction efficiency spectra of a variety of two-dimensional arrays. The longitudinal plasmonic mode, around 1000 nm, remains stationary with increasing transverse periodicity. There is a second longitudinal peak, around 1250 nm, which also remains stationary but undergoes sharpening with increased transverse periodicity. An increase in longitudinal array periodicity causes a blue shift in the plasmonic mode. The appearance and sharpening of the photonic resonance is more dramatic in the variation of the longitudinal periodicity.

The sharp photonic resonances seen in simulation have great potential for biosensing, due to the narrow FWHM and high FOM, and so it was of great interest to demonstrate such resonances experimentally. This requires very high quality fabrication, in order to minimize the surface roughness effects and maintain consistent nanorod shape. In order to have a LSPR in the NIR with a high FOM, nanorods with 200 nm length and 50 nm width were chosen based upon simulation and fabricated by EBL, as shown in Figure 3a. The uniform rod surface and defect-free structure integrity manifest the high quality of nanofabrication. Rectangular arrays were fabricated with periodicities varying from 100 nm to 1 μm in order to observe experimental effects of array parameters. Figure 3b and c show the experimental transmission spectra of two-dimensional arrays with varying transverse and longitudinal periodicity. Simulation predicted that increasing the transverse periodicity would not shift the longitudinal resonance of a two-dimensional array. In the experimental transmission spectra the longitudinal mode of the 1000×100 nm array is red shifted from the resonance position of the other two arrays, and the transverse mode is blue shifted. According to the study on

nanorod geometry, shown in Figure 1, this implies that the nanorods in the 1000×100 nm array are wider than the nanorods in the other two arrays. Increasing the longitudinal periodicity blue shifts the longitudinal mode of the transmission spectra, in good agreement with simulation. Increasing the transverse periodicity also blue shifts the longitudinal mode of the transmission spectra, as predicted from the simulations. The appearance of the sharp photonic resonance in the near-infrared region of the spectrum did not occur as expected from simulated results. This is assumed to be due to the dielectric mismatch of the experimental system. The simulated environment is a constant dielectric medium with refractive index of 1.331, whereas the experimental system consists of an indium-tin oxide (ITO) coated glass substrate and air. A dielectric medium with refractive index of 1.331 was determined to be the closest approximation to the experimental system, as the resonances match at these conditions.

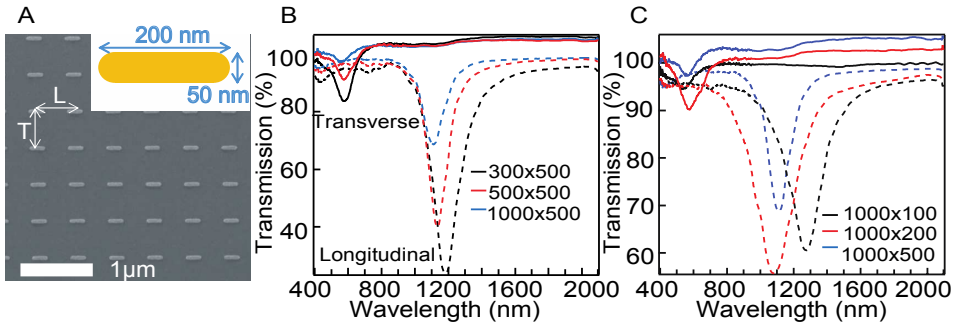

Figure 3. a) Scanning electron microscopy image of nanorod array. "L" denotes the longitudinal array parameter. "T" denotes the transverse array parameter. Inset shows the nanorod geometry. Nanorods are 200 nm long and 50 nm wide. Experimental transmission spectra for two-dimensional nanorod arrays with varying b) transverse and c) longitudinal periodicity. Solid lines represent longitudinal polarization and dashed lines represent transverse polarization.

The existence of such a sharp resonance as appears in the 300 × 500 nm and 500 × 500 nm arrays is instantly recognizable as a potential LSPR biosensor as its narrow FWHM, approximately 100 nm, would result in a high FOM, meaning that very small shifts in the resonance easily distinguishable. To determine the sensitivity and FOM of this nanorod array, media of different refractive indices were applied and the resonance red shifts were measured. Figure 4a shows, in black, the experimental sensitivity, 309.6 nm/RIU, of the longitudinal mode of a 300 × 500 nm array in a variety of concentrations of glycerol. The FOM was calculated to be 3.60. Figure 4a also shows, in blue, the simulated sensitivity, 679.3 nm/RIU, of a single nanorod to changes in homogenous dielectric environment. Both calculations of the response of the system to changes in refractive index show a very good linear fit with a coefficient of determination very close to one. The discrepancy in sensitivity is due to the difference in nanoparticle surface area exposed to changes in dielectric material resulting from simulating a homogenous dielectric environment while the experimental conditions of a nanoparticle on an ITO/glass substrate coated with dielectric material. When considering that, using the effective medium theory, an ITO/glass substrate can be approximated in DDSCAT by a refractive index of 1.331, one could recalculate the simulated sensitivity, with adjusted refractive index to take the substrate into account. The simulated environment of a nanoparticle in a homogenous dielectric medium of refractive index 1.331 is equivalent to a particle on an ITO substrate in air. The simulated environment of a nanoparticle in a homogenous dielectric medium of refractive index 1.5 is equivalent to a particle on an ITO substrate in a medium of RI 1.34. Using these equivalencies, a 126.6 nm shift for a change of medium with a refractive index of 0.34 RIU, the simulated sensitivity is 372.4 nm/RIU. This value is consistent with the experimental value.

In order to evaluate the sensitivity of the nanorod arrays as a potential biosensing platform, the shift caused by molecular binding events must be evaluated. We first chose to evaluate the response of the rod array device upon nucleic acid molecule binding. The nanorod array with the highest FOM was chosen, 300×500 nm period. Nanorod arrays were incubated sequentially with thiolated biotin, streptavidin, and biotinylated DNA and the LSPR shift was measured for each binding event. Figure 4b and c show the spectra and λ_{max} shifts, respectively, for different concentrations of biotinylated DNA, down to 0.1 aM. This concentration of DNA corresponds to approximately 3 molecules in 50 μL of buffer solution. This is a very low limit of detection through streptavidin-biotin binding, and proves the potential of this plasmonic substrate as a biosensing platform towards ultrasensitive detection of nucleic acids.

Nanoscale RSCPublishing

ARTICLE

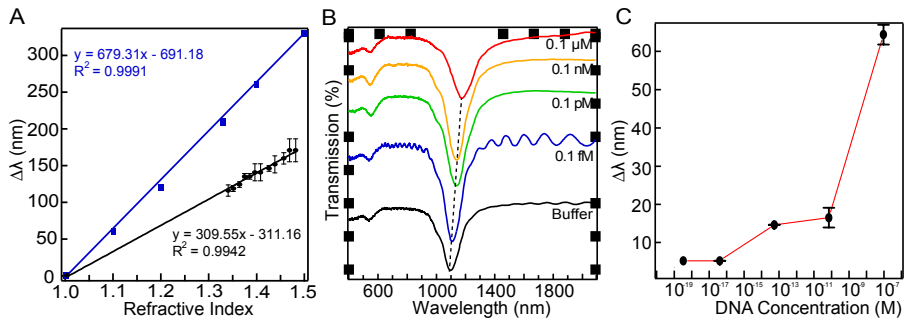

Figure 4. LSPR-based chemical and biological sensing. a) Dielectric sensitivity. Black data and equation denote the experimental study of a nanorod array on ITO/glass substrate with 300 nm longitudinal periodicity and 500 nm transverse periodicity coated with dielectric medium. Blue data and equation denotes the DDA simulation of a single nanorod in homogenous dielectric. b) Spectra and c) LSPR λ_{max} shift of the same nanorod array with varying concentrations of DNA in log scale.

With an optimized performance in the near-infrared regime, nanorods array can be further devised as a high performance device towards the discrimination of single nucleotide polymorphism (SNP). As shown in Figure 5a, the principle of the SNP detection is based on cleavage activity of SURVEYOR nuclease which has been shown to recognize and cleave all types of SNP in heteroduplex DNA with high specificity.[43] Following the immobilization of thiolated DNA probe molecules on the AuNRs surface, WT DNA or MT DNA containing SNP is introduced to bind with the DNA probe *via* DNA hybridization. SURVEYOR nuclease is subsequently applied to the AuNR arrays, leading to a specific cleavage of all imperfectly hybridized DNA duplexes (MT) while maintaining the perfectly hybridized products with the WT DNA. The cleavage leads to shorter DNA molecules attached to the nanorods array, therefore the absorption bands blue shift. Figure 5b and c represents consistent phase shifts caused by the molecular binding events. In both cases, wavelength red shifts after the DNA probe immobilization and after the DNA hybridization were respectively obtained about 20 nm and 51 nm as compared to the initial longitudinal plasmon band of the investigated AuNRs. Hybridization results with various WT DNA concentrations is shown in more detailed in Figure SI2 which indicates that the AuNR arrays could be used to detect the DNA oligonucleotide at concentration as low as 0.1 nM. In addition, the enzymatic cleavage caused a tremendous blue-shift of 46 nm in the case of 1 μM MT DNA, and this blue-shift value is only less than 6 nm in that of 1 μM WT which possibly corresponds to non-specific interaction between the WT DNA and the immobilized probes. To further investigate the discriminating power and selectivity of the assay, various ratio mixtures of MT/WT have been analyzed. As shown in the inset of Figure 5c, the phase shift value is proportional to the increase of MT/WT ratios after the enzyme cleavage. Because non-specific hybridization of WT DNA to the immobilized probe caused a shift of 6 nm, therefore the AuNRs sensor combined with the enzyme cleavage strategy could clearly discriminate the SNP down to 10 nM in the presence of 100-fold higher concentration of the WT DNA (MT/WT = 10/1000 nanomolar ratio).

Nanoscale RSCPublishing

ARTICLE

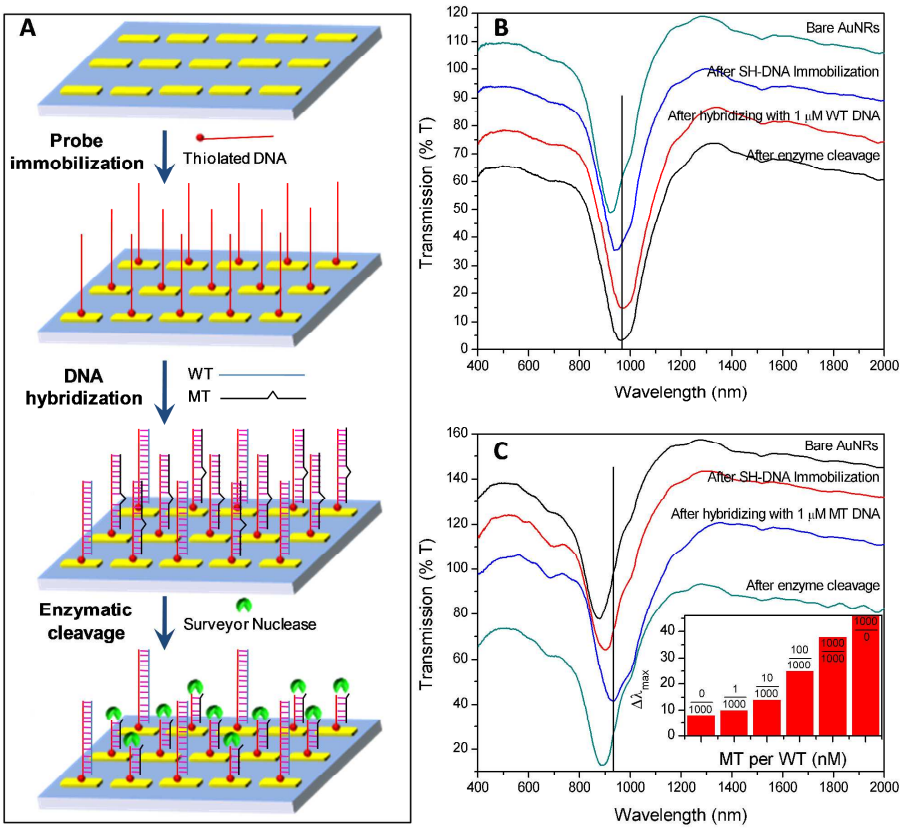

Figure 5. Detection of single nucleotide polymorphism (SNP) by a means of AuNRs. A). Overall scheme describing step-by-step procedure of the detection. B). The enzymatic cleavage causes a very small blue-shift as hybridized with the WT DNA. C) indicating that a large blue-shift was obtained as hybridized with the MT DNA. Inset in Figure C shows that the AuNRs sensor could clearly discriminate the SNP down to 10/1000 molar ratio of MT/WT.

Methods

Discrete Dipole Approximation Simulation.

Simulation of the extinction efficiency and electric field was carried out using the DDA method in the DDSCAT program, version 7.0.[44, 45] A grid spacing of 1 nm was used for all simulations. The dielectric constants of Au are from Johnson and Christy.[46] The electric field intensity over the nanoparticle surface was calculated for isolated targets in an effective medium of refractive index of 1.331. The electric field information was used to make contour plots of the intensity on and around the nanoparticle to visualize the features of different modes of excitation. The extinction efficiency was simulated for multiple wavelengths to produce spectra used to determine the resonance position of the particles or arrays.

Nanorod Array Fabrication.

Electron beam lithography (EBL) was used to fabricate the nanorod arrays. The same polymer layer was used for all chips, 950 poly (methyl methacrylate) (PMMA) A4. The PMMA was spin-coated onto the chips using at 4000 rpm for 40 s (Specialty Coating Model P6700) and then baked at 180 °C for 15 min. EBL was performed using a JEOL JSM-7001F field emission scanning electron microscope (SEM) equipped with a Deben Beam Blanker and a nanometer pattern generation system (NPGS). After e-beam writing, the chips were developed for 75 s in a solution of 1:3 methyl isobutyl ketone (MIBK):isopropyl alcohol (IPA) at room temperature. After development the chips were rinsed for 20 s in IPA and blown dry using nitrogen gas. Evaporation of 2 nm Cr and 30 nm Au was sequentially done in a thermal evaporator (Elite Engineering, Singapore). A chamber pressure of 2×10^{-7} Torr and evaporation rate of approximately 0.6 Å/s were used for evaporation. Liftoff was done at room temperature in acetone for 2 hr followed by a 2 min sonication (Crest Ultrasonics Powersonic P1100D) at low power (level 2). Nanorod geometry was observed and measured by SEM.

Transmission Spectroscopy Measurement.

Transmission spectroscopy was performed on a 20/20 PV™ UV-Visible-NIR microspectrophotometer (CRAIC Technologies™, USA) with non-polarized light in air, unless otherwise noted, with an angle of incidence of 90 degrees and an aperture size 15 μm. Spectra were taken for at least three locations per sample.

Figure of Merit Determination.

For the dielectric sensitivity testing Au nanorods chip was first cleaned by sonication in IPA for one minute, washed in deionized water and dried by nitrogen gas. Then, glycerol solutions (Alfa Aesar, UK) of 1%, 10%, 20%, 28%, 36%, 44%, 52%, 64%, 72%, 84%, 92%, and 100% in deionized water, corresponding to different refractive indices (RI) of 1.3342, 1.3448, 1.3572, 1.3676, 1.33897, 1.4011, 1.4189, 1.4310, 1.4492, 1.4613, and 1.4735 respectively, were deposited and covered by a cover slip.[47] After each measurement, the chip and cover slip were rinsed by deionized water and blown dry using nitrogen gas. LSPR λ_{max} shifts were plotted against their respective refractive index unit, and sensitivity of Au nanorods was calculated by linear regression.

DNA and Single Point Mutation Detection

For DNA sensing experiments, the chip was washed by IPA, rinsed by deionized water, and then cleaned by ultraviolet-ozone process (UV-1, SAMCO, Japan) for 15 min. Immediately after cleaning, the chip was incubated in 1 mM solution of 1:9 (v/v) mixture of biotin-PEG3-thiol (spacer arm length 27-28 Å, nanoScience Instruments, USA) and methyl-PEG4-thiol (spacer arm length 15.8 Å, Pierce, USA) in DMSO for 2 hr. The chip was washed in deionized water for 5 min and blown dry using nitrogen gas. The chip was incubated in a streptavidin (Pierce, USA) solution of 250 nM for 1 hr, washed in phosphate buffered saline (PBS, pH 7.4) for 5 min, rinsed in deionized water, and dried using nitrogen gas. To apply as minimum as possible amount of DNA solution, the nanorod array was bound by a hydrophobic tape. The nanorod array was then incubated in 100 μL of biotinylated DNA (MW 9440 Da, 1st BASE, Singapore) of 10^{11}, 10^{8}, 10^{5}, 10^{2}, and 10^{-1} aM concentrations in PBS for 1 hr. Then the chip was washed in PBS for 5 min, rinsed with deionized water, and dried by nitrogen gas.

For the SNP experiments, DNA oligonucleotides were purchased from Integrated DNA Technologies, Singapore. 100 μM thiolated DNA capture probe corresponding for Arg12 mutations (5'-Dithiol-TTT TTT TTT TAG CTC GTG GCG TAG GC-3') was first mixed with 150 mM dithiothreitol (Sigma-Aldrich, Singapore) at room temperature for 2 hr to deprotect the terminal thiol group.[48] After the deprotection, the thiolated DNA probe was desalted and purified using a NAP-5 column (GE Healthcare, Singapore). An open chamber was made by punching a hole (d ~ 8 mm) on an adhesive tape using a paper puncher and sticking it onto the ITO glass substrate where the AuNRs are aligned in the center of the hole. Then, 20 μL of 20 μM deprotected DNA probe diluted in PBS buffer (100 mM, pH 7) was dropped into the open chamber and incubated at room temperature overnight. A glass coverslip (thickness no. 1) was placed on the top of the chamber to avoid evaporation. After the incubation, wash the chip with PBS buffer and air-dry.

Wild type (WT, 5'-GCC TAC GCC ACG AGC TAA AAA AAA AA-3') and mutant type (MT, 5'-GCC TAC GCC ACC AGC TAA AAA AAA AA-3') DNA samples at various concentrations and ratios were hybridized with the DNA probes immobilized on the AuNRs' surface. Briefly, 10 μL of each DNA sample was mixed with 10 μL PerfectHyb™ Plus hybridization buffer (Sigma-Aldrich, Singapore). After that, the mixture was added onto the DNA-functionalized AuNRs. Then, the reaction was first incubated at 90 ºC for 5 min, and then at 42 ºC for 2 hr. During the incubation, a high humidity condition should be kept to avoid evaporation. After the incubation, the AuNRs was washed by DNA-free H_2O. After hybridizing with the immobilized DNA probe, the samples were treated with Surveyor Nuclease (Transgenomic Inc., UK) according to the manufacturer's protocol. Subsequently the chip was washed by DNA-free H_2O and measured using transmission microspectrophotometer.

Conclusions

In summary, we have systematically investigated the effects of nanorod geometry and array parameters in order to design an effective LSPR-based biosensing substrate. Increasing the aspect ratio of nanorods leads to sharpening of resonances and better FOM. Simulations of two-dimensional arrays, confirmed experimentally, have shown that increasing the longitudinal or transverse period blue shifts the longitudinal plasmonic

resonance. No experimental evidence was found for the appearance of the photonic resonance shown in simulations. Lithographically fabricated nanorod arrays with very sharp resonances have proven to be highly sensitive to the surrounding refractive index, generating an effective LSPR substrate with a figure of merit of 3.6 and a sensitivity of 310 nm/RIU. DNA molecules were detected down to 0.1 aM (~3 molecules in 50 μL). Colon cancer SNPs were detected down to 10/1000 molar ratio of MT/WT. The unambiguous discrimination of SNPs and the high sensitivity to local RI suggest that the nanorod arrays could be used for not only point mutation detections but also for a variety of applications such as cancer diagnostics and other point-of-care testing.

Acknowledgements

The author Q.X. would like to acknowledge the strong support from Singapore National Research Foundation through a Fellowship grant (NRF-RF2009-06) and a start-up grant support from Nanyang Technological University (M58110061). Q.X. and S.L. gratefully acknowledges the strong support from Singapore Ministry of Education via two Tier 2 grants (MOE2011-T2-2-051 and MOE2011-T2-2-085), respectively.

Notes and references

[a] Division of Physics and Applied Physics, School of Physical and Mathematical Sciences, Nanyang Technological University, Singapore 637371

[b] Institute for Global Food Security, School of Biological Sciences, Queen's University Belfast, Belfast BT9 5AG, United Kingdom

[c] School of Materials Science and Engineering, Nanyang Technological University, Singapore 637371

[d] NOVITAS, Nanoelectronics Centre of Excellence, School of Electrical and Electronic Engineering, Nanyang Technological University, Singapore 639798

References:

1. N. Verellen, Y. Sonnefraud, H. Sobhani, F. Hao, V. V. Moshchalkov, P. Van Dorpe, P. Nordlander and S. A. Maier, *Nano letters*, 2009, 9, 1663-1667.
2. F. Hao, Y. Sonnefraud, P. Van Dorpe, S. A. Maier, N. J. Halas and P. Nordlander, *Nano letters*, 2008, 8, 3983-3988.
3. C. Y. Chao and L. J. Guo, *Applied Physics Letters*, 2003, 83, 1527-1529.
4. A. E. Miroshnichenko, S. Flach and Y. S. Kivshar, *Reviews of Modern Physics*, 2010, 82, 2257-2298.
5. J. A. Fan, C. H. Wu, K. Bao, J. M. Bao, R. Bardhan, N. J. Halas, V. N. Manoharan, P. Nordlander, G. Shvets and F. Capasso, *Science*, 2010, 328, 1135-1138.
6. B. Luk'yanchuk, N. I. Zheludev, S. A. Maier, N. J. Halas, P. Nordlander, H. Giessen and C. T. Chong, *Nature materials*, 2010, 9, 707-715.
7. Q. Zhang, X. Wen, G. Li, Q. Ruan, J. Wang and Q. Xiong, *ACS nano*, 2013, DOI: 10.1021/nn4047716.
8. J. N. Anker, W. P. Hall, O. Lyandres, N. C. Shah, J. Zhao and R. P. Van Duyne, *Nature materials*, 2008, 7, 442-453.
9. R. de la Rica and M. M. Stevens, *Nat Nanotechnol*, 2012, 7, 821-824.
10. L. Rodriguez-Lorenzo, R. de la Rica, R. A. Alvarez-Puebla, L. M. Liz-Marzan and M. M. Stevens, *Nature materials*, 2012, 11, 604-607.
11. P. L. Truong, C. Cao, S. Park, M. Kim and S. J. Sim, *Lab on a chip*, 2011, 11, 2591-2597.
12. B. Peng, G. Li, D. Li, S. Dodson, Q. Zhang, J. Zhang, Y. H. Lee, H. V. Demir, X. Y. Ling and Q. Xiong, *ACS nano*, 2013, 7, 5993-6000.
13. X. L. Xu, B. Peng, D. H. Li, J. Zhang, L. M. Wong, Q. Zhang, S. J. Wang and Q. H. Xiong, *Nano letters*, 2011, 11, 3232-3238.
14. X. Wen, G. Li, J. Zhang, Q. Zhang, B. Peng, L. M. Wong, S. Wang and Q. Xiong, *Nanoscale*, 2013, DOI: 10.1039/C3NR04012G.
15. C. Cao, J. Zhang, X. Wen, S. L. Dodson, N. T. Dao, L. M. Wong, S. Wang, S. Li, A. T. Phan and Q. Xiong, *ACS nano*, 2013, 7, 7583–7591.
16. K. A. Willets and R. P. Van Duyne, *Annu Rev Phys Chem*, 2007, 58, 267-297.
17. C. R. Yonzon, D. A. Stuart, X. Y. Zhang, A. D. McFarland, C. L. Haynes and R. P. Van Duyne, *Talanta*, 2005, 67, 438-448.
18. A. J. Haes, L. Chang, W. L. Klein and R. P. Van Duyne, *J Am Chem Soc*, 2005, 127, 2264-2271.
19. A. B. Dahlin, J. O. Tegenfeldt and F. Hook, *Analytical Chemistry*, 2006, 78, 4416-4423.
20. S. Chen, M. Svedendahl, R. P. Van Duyne and M. Kall, *Nano letters*, 2011, 11, 1826-1830.
21. K. M. Mayer and J. H. Hafner, *Chem Rev*, 2011, 111, 3828-3857.
22. M. E. Stewart, C. R. Anderton, L. B. Thompson, J. Maria, S. K. Gray, J. A. Rogers and R. G. Nuzzo, *Chem Rev*, 2008, 108, 494-521.
23. J. Homola, *Chem Rev*, 2008, 108, 462-493.
24. S. L. Zou and G. C. Schatz, *Surface-Enhanced Raman Scattering: Physics and Applications*, 2006, 103, 67-85.
25. N. Liu, M. Hentschel, T. Weiss, A. P. Alivisatos and H. Giessen, *Science*, 2011, 332, 1407-1410.
26. N. J. Halas, S. Lal, W. S. Chang, S. Link and P. Nordlander, *Chem Rev*, 2011, 111, 3913-3961.
27. S. L. Zou, N. Janel and G. C. Schatz, *J Chem Phys*, 2004, 120, 10871-10875.
28. S. L. Zou and G. C. Schatz, *J Chem Phys*, 2004, 121, 12606-12612.
29. S. Malynych and G. Chumanov, *J Am Chem Soc*, 2003, 125, 2896-2898.
30. L. K. Ausman, S. Z. Li and G. C. Schatz, *Journal of Physical Chemistry C*, 2012, 116, 17318-17327.
31. J. R. Lombardi and R. L. Birke, *Accounts of Chemical Research*, 2009, 42, 734-742.
32. S. M. Morton, D. W. Silverstein and L. Jensen, *Chem Rev*, 2011, 111, 3962-3994.
33. H. N. Chen, J. M. McMahon, M. A. Ratner and G. C. Schatz, *Journal of Physical Chemistry C*, 2010, 114, 14384-14392.
34. A. Jemal, R. Siegel, E. Ward, T. Murray, J. Xu and M. J. Thun, *CA: a cancer journal for clinicians*, 2007, 57, 43-66.
35. D. W. Hadley, J. F. Jenkins, E. Dimond, M. de Carvalho, I. Kirsch and C. G. Palmer, *Journal of clinical oncology : official journal of the American Society of Clinical Oncology*, 2004, 22, 39-44.

36. S. Dodson, M. Haggui, R. Bachelot, J. Plain, S. Z. Li and Q. H. Xiong, *Journal of Physical Chemistry Letters*, 2013, 4, 496-501.
37. C. Girard, C. Joachim and S. Gauthier, *Rep Prog Phys*, 2000, 63, 893-938.
38. J. W. P. Hsu, *Mat Sci Eng R*, 2001, 33, 1-50.
39. M. Haggui, M. Dridi, J. Plain, S. Marguet, H. Perez, G. C. Schatz, G. P. Wiederrecht, S. K. Gray and R. Bachelot, *ACS nano*, 2012, 6, 1299-1307.
40. G. P. Wiederrecht, G. A. Wurtz and J. Hranisavljevic, *Abstracts of Papers of the American Chemical Society*, 2005, 229, U865-U865.
41. C. Hubert, R. Bachelot, J. Plain, S. Kostcheev, G. Lerondel, M. Juan, P. Royer, S. L. Zou, G. C. Schatz, G. P. Wiederrecht and S. K. Gray, *Journal of Physical Chemistry C*, 2008, 112, 4111-4116.
42. G. A. Wurtz, J. Hranisavljevic and G. P. Wiederrecht, *Nano letters*, 2003, 3, 1511-1516.
43. P. Qiu, H. Shandilya, J. M. D'Alessio, K. O'Connor, J. Durocher and G. F. Gerard, *BioTechniques*, 2004, 36, 702-707.
44. B. T. Draine and P. J. Flatau, *Journal of the Optical Society of America a-Optics Image Science and Vision*, 1994, 11, 1491-1499.
45. B. T. Draine and P. J. Flatau, *Journal of the Optical Society of America a-Optics Image Science and Vision*, 2008, 25, 2693-2703.
46. P. B. Johnson and R. W. Christy, *Physical Review B*, 1972, 6, 4370-4379.
47. L. F. Hoyt, *Ind Eng Chem*, 1934, 26, 329-332.
48. L. Prix, P. Uciechowski, B. Bockmann, M. Giesing and A. J. Schuetz, *Clinical chemistry*, 2002, 48, 428-435.